A low cost eddy current displacement sensor for active magnetic bearings

---

A dissertation presented to

The School of Electrical, Electronic and Computer Engineering

North-West University

In partial fulfilment of the requirements of the degree

Master Ingeneriae

in Electrical and Electronic Engineering

by

Andries J. Grobler

Supervisor: Prof. G van Schoor
Co-supervisor: Dr. EO Ranft

May 2008

Potchefstroom Campus

DECLARATION

I hereby declare that all the material incorporated in this thesis is my own original unaided work, except where specific reference is made by name or in the form of a numbered reference. The work herein has not been submitted for a degree at another university.

Signed: _____

Andries J. Grobler

SUMMARY

The McTronX research group of the North-West University is involved in active magnetic bearing (AMB) research. An AMB is a mechatronic system that levitates a rotating axis with electromagnetic forces. The group has successfully implemented radial and axial AMBs as well as a complete flywheel energy storage system operating at 22 000 rpm. Research is also done on using the actuator voltage and current to derive rotor position, also known as self-sensing, but these methods have not been perfected.

Position measurement is very important in AMBs, since it is the main control variable. The literature indicates that the eddy current phenomenon is well suited for displacement measurement, since it is relatively noise immune and insensitive to process medium when a non-magnetic and non-conductive substance is used. Printed circuit board (PCB) sensors must be considered when low cost is a requirement.

The goal of this project is to design, simulate, manufacture and test a PCB based, low cost eddy current displacement sensor for AMBs. This project will focus on the sensor (probe) that converts the physical rotor movement to an electric signal. An evaluation platform, used to test the PCB sensor, is also designed and manufactured as part of this project.

The first step in the sensor design is to establish a suitable software model. A finite element method (FEM) software package, Comsol®, is used to realise a FEM model of the sensor. This FEM model is used to simulate sensor behaviour in various configurations. The trends found in the FEM model results are used to compile a design flow diagram. This diagram is illustrated by applying it to single, double- and five-layer designs. The single- and double-layer sensors are manufactured and tested to validate the accuracy of the FEM model and design flow diagram.

Close correlation between the practical and predicted results is found for the single- and double-layer sensors. The sensitivity and working point rms voltage correlated exceptionally well for both sensors. Linearity does not correlate as closely due to the evaluation platform and circuitry but is still within acceptable limits when compared to other displacement sensors used in AMBs.

This project laid the foundation for PCB sensor design in the McTronX group. A comparison between the different sensors showed that the double-layer sensor is the best choice in terms of cost and performance. It is concluded that the PCB displacement sensor presented in this dissertation is a viable low cost option for displacement measurement in AMBs.

Acknowledgments

I would like to make use of this opportunity to thank and acknowledge the following people and institutions:

- Our heavenly Father; Soli Deo Gloria.
- My wife; Leenta, for always believing in me and being the best life partner anyone could ask for. "...But the greatest of these is love." 1 Corinthians 15:13b [NIV].
- Prof. George van Schoor and Dr. Eugén Ranft; exceptional supervisors, for their advice and support. Mentors of their calibre are very rare indeed.
- My family; Andries, Maria, Miemie, Grandfather Louis and Grandmother Bessie, for their love, support and encouragement.
- The McTronX research group; Kristoff, Jan, Stefan, Elna, Rikus, Elsebi, Jacques, Dewald, Jannik, Pieter, Kenny, Andries, André and Gordon, for advice over coffee and making research a team sport.
- M-Tech Industrial and THRIP for financial support.

"Whatever you do, work at it with all your heart, as working for the Lord, not for men, since you know that you will receive an inheritance from the Lord as a reword. It is the Lord Christ you are serving. " Colossians 3:23 - 24 [NIV]

Contents

List of Figures

List of Tables

LIST OF ABBREVIATIONS

ac	Alternating current
Al	Aluminium
AMB	Active magnetic bearing
CAD	Computer-aided design
dc	Direct current
FEM	Finite element method
Fe	Iron (Mild steel)
FFT	Fast fourier transform
FSO	Full scale output
GMD	Geometric mean distance
IQR	Interquartile range
MW	Modified wheeler
NWU	North-West University
PCB	Printed circuit board
PLL	Phase locked loop
PSU	Power supply unit
rms	Root mean square
rpm	Revolutions per minute
SMR	Start of measuring range
Ss	AISI 304 Stainless steel

LIST OF SYMBOLS

Latin letters

A	Track area	[m^2]
$\overline{B}$	Magnetic flux density	[T] = [Vs/m^2]
$\overline{D}$	Electric flux density	[C/m^2]
d	Diameter	[m]
$\overline{E}$	Electric field intensity	[V/m]
f	Frequency	[Hz]
f	Force (Chapter 2)	[N]
h	Height	[m]
$\overline{H}$	Magnetic field intensity	[A/m]
$\tilde{I}$	Current phasor	[A]
i	Current (ac)	[A]
I	Current (rms)	[A]
$\overline{J}$	Current density	[A/m^2]
L	Inductance	[H]
N,n	Number of turns in a coil	
R	Resistance	[Ω]
$\Re$	Reluctance	[A.t/Wb]
s	Airgap (Chapter 2)	[m]

T	Temperature	[°C]
$\tilde{V}$	Voltage phasor	[V]
w	Width	[m]
X	Reactance	[Ω]
$\tilde{Z}$	Impedance phasor	[Ω]

Greek letters

μ	Permeability	[H/m]
Φ	Magnetic flux	[Wb]
θ	Phase angle	[rad]
Φ	Sensing coil angle	[°C]
ϵ	Permittivity	$[C^2/Nm^2]$ = [F/m]
ρ	Fill ratio	
σ	Conductivity	[S/m] = [1/Ωm]

Latin subscripts

0	Free space
304Ss	AISI 304 Stainless steel
ac	Alternating current
ag	Airgap
ax	Axis
ave	Average
cu	Copper
dc	Direct current
em	Excitation coil maximum
exc	Excitation coil
Fe	Mild steel (Iron)
in	Inner
L	Inductance
out	Outer
r	Relative
ri	Rise
rms	Root mean square
s	Track spacing
sens	Sensing coil
t	Track

Chapter 1

Introduction

This chapter presents a short introduction to active magnetic bearings and the position sensors used in these systems. The problem statement, the issues that must be addressed to solve this problem and the methods that will be used to address these issues are introduced. The chapter concludes with an overview of the dissertation.

1.1 Background

This section gives an overview of the work done on AMBs, the position sensors used in these systems and eddy current displacement measuring.

1.1.1 Previous work

The School of Electrical, Electronic and Computer Engineering at the North-West University (NWU) has an active magnetic bearing (AMB) research group called McTronX. This group has successfully developed various laboratory AMB models, including radial and axial AMBs with speeds of up to 10 000 rpm as well as a flywheel energy storage system with an operating speed of 30 000 rpm [1], [2]. Different actuator configurations e.g. heteropolar and homopolar, have been researched as well as linear and switching power amplifiers. Integrated controllers as well as single board computers, used to control the AMBs, have also been explored [3].

Sensors are the main AMB components the group has not yet researched and developed extensively. Research is being done on self-sensing methods but it is too early to say whether these techniques could reliably and economically replace physical sensors. Self-sensing methods often lead to inferior system robustness, requiring more complex control and expensive controllers [4]. Developing sensors in-house will decrease AMB cost, as the sensors currently used make up a large portion of the total system cost. This will also enable the group to offer a complete solution without being dependent on external suppliers. The next section gives an introduction to AMBs.

1.1.2 Active magnetic bearings

The sensor will be developed for use in an AMB system. Figure 1.1 shows the main components of an AMB, including the sensor system, control system, power amplifiers and electromagnets. The main goal of an AMB is to levitate the rotor between the electromagnets, thus eliminating physical contact with the stationary parts of the system. To achieve this goal, the position of the rotor is measured and supplied to the control system. The control system changes the input to the power amplifiers in response to the position input, according to the control algorithm. Power amplifiers supply the electromagnetic actuators placed around the rotor with the power required to suspend the rotor. Accurate position measurement of the rotor is of utmost importance since rotor position is the main control variable in an AMB system.

1.1.3 AMB position sensors

Only non-contact position sensors, meaning there is no physical contact between the sensor and the target material, can be used in AMBs. The most common AMB sensor technologies include; optical, inductive, eddy current, Hall-effect, capacitive and self-sensing; all discussed in [5]. The most important sensor characteristics include; measuring range, linearity, sensitivity, resolution and frequency range [6].

The space between the non-contact position sensor and the target is commonly referred to as the airgap, since it is usually filled with air. AMBs can be placed inside the process and process material, meaning the airgap would be filled with water if used in a water pump or helium when used in a helium blower. The position sensor is also placed in the process material and thus it must be able to operate in these conditions. Sensors based on capacitive and optical principles are not well suited for these conditions. Sensors using magnetic principles are not

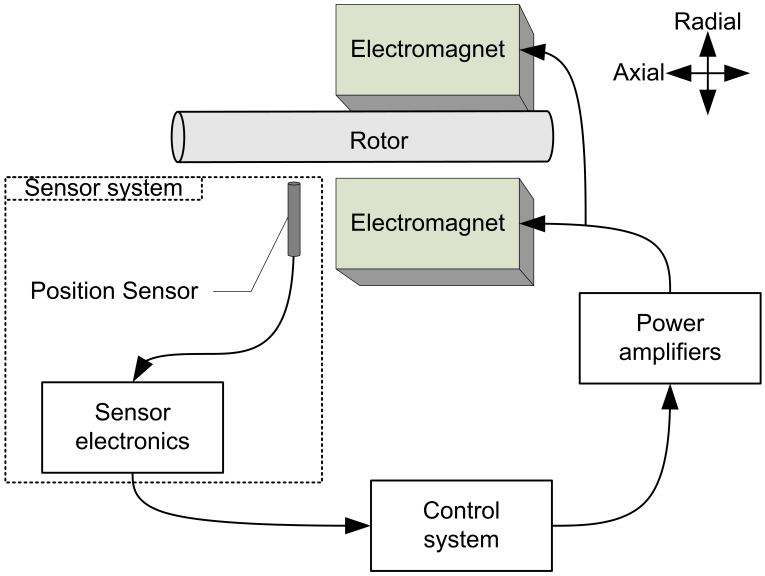

Figure 1.1: Basic radial AMB system diagram.

influenced by the process material when the latter is non-magnetic and non-conductive. These sensors are not influenced by dirt (dust and oil) in the airgap. The next section introduces the eddy current phenomenon.

1.1.4 The eddy current phenomenon

The word eddy is used to describe a circular movement in water or a small whirlpool [7]. Eddy or Foucault currents was first documented by J.D.L Foucault in 1851. This phenomenon is present whenever a conducting material is placed in a varying magnetic field. Faraday induction will cause voltage differences on the conducting material, which will lead to short-circuit currents flowing in the material. Eddy currents is commonly known as a cause of power losses in electrical motors and transformers. In most cases laminated cores and materials with low conductivity are used to minimise the effects of eddy currents [8].

The eddy current phenomenon will now be explained. Referring to Figure 1.2, a cross-sectional view of a circular conducting material (rotor) surrounded by a current carrying wire is shown. An alternating magnetic field is established by this current carrying wire. In this case the current flows in the anti-clockwise direction causing a magnetic field pointing out of the page near the rotor and into the page outside the coil. According to Lenz's law, the surface currents flowing in a clockwise direction will be caused by this magnetic field [9]. The flow of these surface currents causes the residual magnetic flux in the material to approach zero.

The eddy current phenomenon has certain properties that are advantageous when used in sensors. Eddy currents is not influenced by irregularities e.g. dirt, dust, oil etc., between the coil and the conducting material. The amplitude of the eddy current is dependent on the conductivity of the material and the magnetic field changes caused by the current flowing in a coil [10].

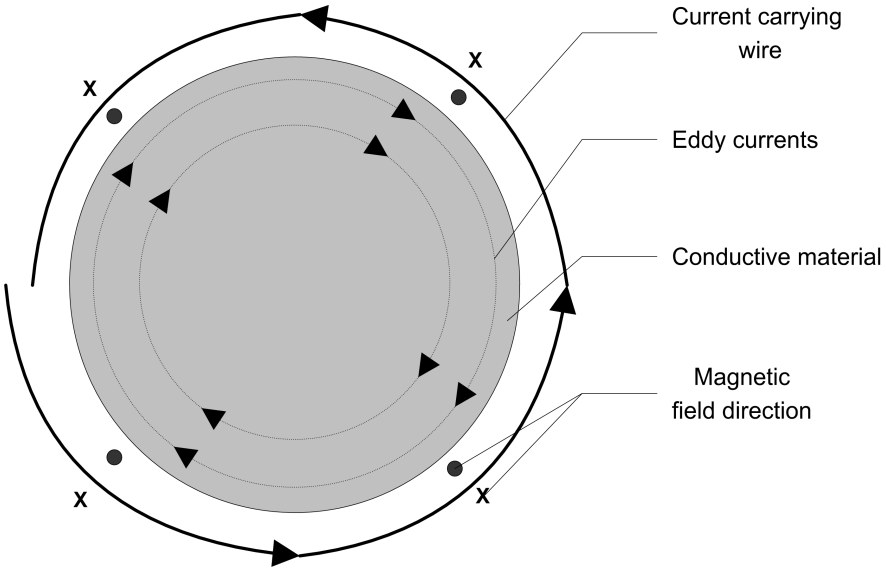

Figure 1.2: Eddy currents in cylindrical conductive material.

1.1.5 Measurement using eddy currents

Non-contact distance measurement using eddy currents has been studied for decades as can be seen in a 1975 patent by Kaisha [11]. An exciting coil, driven by operational amplifiers, carries an alternating current of constant frequency and amplitude. An alternating magnetic field is established, inducing eddy currents in a conducting material. The eddy currents will in turn cause a magnetic field that opposes the exciting magnetic field. This will cause a change in the exciting coil's inductance. The patent mentioned above also provides different techniques for measuring this change and relating it to the distance between the excitation coil and conducting material.

These early eddy current sensors had a few problems. The sensors were very susceptible to temperature changes. This would result in a change of the exciting coil's impedance. If a ferromagnetic bobbin was used, the permeability of the bobbin also changed when the temperature changed. Most of the sensors used resonant circuits to determine the change in inductance. This required a high stability oscillator. It is also difficult to adjust the resonant and oscillator frequencies to be equal. Another problem is that the manufacturing process of the excitation coil is labour intensive and expensive.

Most of the problems mentioned above have been resolved. Configurations that are capable of automatic temperature compensation are discussed in patent [12] and is shown in Figure 1.3. Advanced phase locked loops (PLLs) automatically adjust the oscillator frequency to match the resonant frequency. Printed circuit board (PCB) techniques are used to manufacture sensors at a fraction of the price and with very good repeatability [13].

The next section presents a radial displacement sensor, implemented on a PCB.

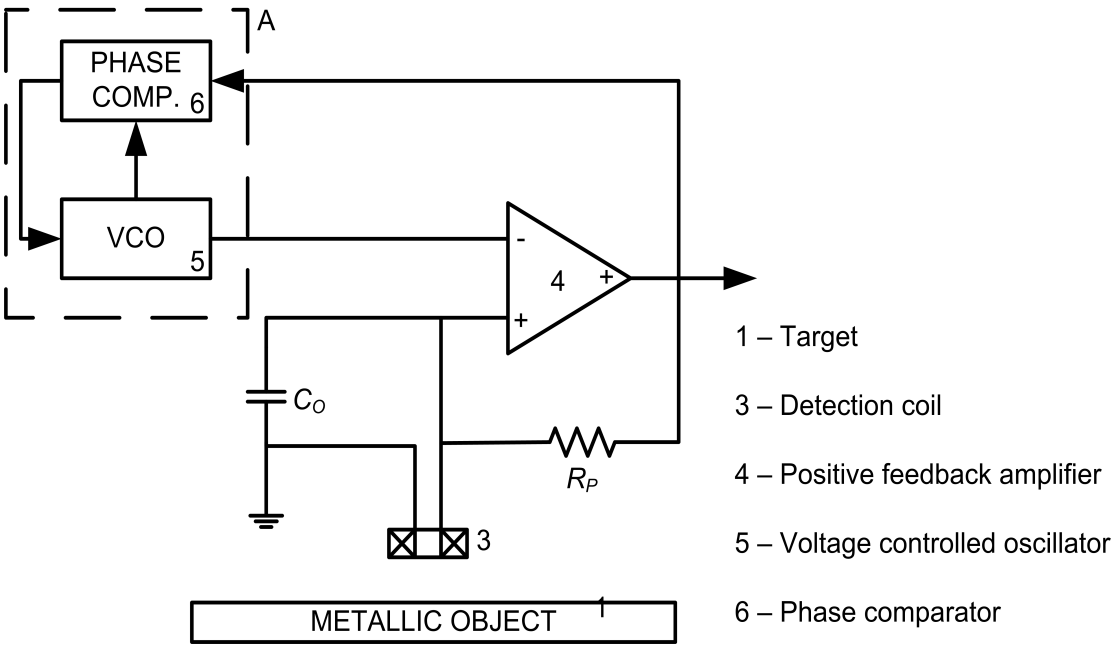

Figure 1.3: Eddy current sensor of 1980 [12].

1.1.6 New PCB sensor for AMBs

In 2004, P Bühler presented a patented radial sensor for AMBs, manufactured using PCB techniques [14]. A sketch of this sensor is shown in Figure 1.4. It features a magnetic field generating coil (excitation coil), placed around the target, and field measurement coils (detector coils), placed in specific sectors of the PCB. The excitation coil carries a signal with a modulation frequency ranging between 2 kHz and 3 MHz. A change in position will result in a change in the local magnetic fields. This change of magnetic flux is detected by the measuring coils, causing a change in the voltage induced in these coils. The voltage induced on these detector coils are used to derive the target movement [4].

This sensor offers various advantages, including:

- low cost
- a high level of reproducibility
- more sensitive than previous PCB sensors
- a very compact sensor
- the sensor probe only consist of a PCB track (no extra components)
- not susceptible to external magnetic fields (no magnetic shielding necessary)

Another exciting application of this type of sensor is high temperature (> 500 °C) environments. Using thin-film techniques to realise silver coils on ceramic substrates, the sensor was successfully implemented as shown in [15].

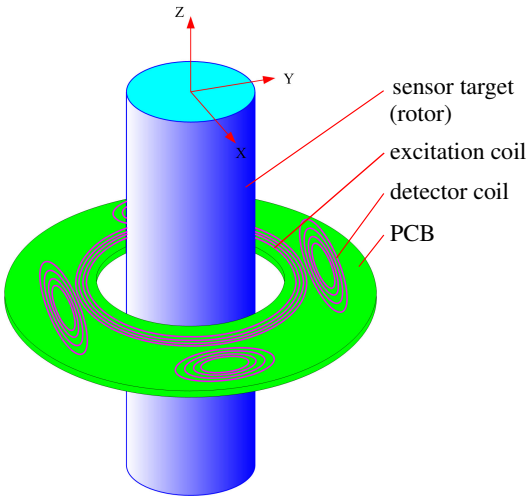

Figure 1.4: New PCB sensor for AMBs [4].

Previous work done by McTronX members, as well as a literature survey, showed that eddy current sensors as discussed in [4] and [14], are best suited for the needs of the McTronX group. The problem statement is presented next.

1.2 Problem statement

The objective of this project is to design, simulate, manufacture and test a low cost PCB based, eddy current displacement sensor for AMB systems.

The sensor system can be divided into two physical parts; the sensor (probe) and sensor electronics. This project focuses on the sensor since the McTronX group has no prior experience in PCB sensors. Deriving an optimal design process that can be used when designing a PCB sensor is one of the goals. This design tool can aid designers, inexperienced in eddy current displacement sensing, to design PCB sensors.

Modelling and simulating the PCB sensor is also an important part of this project. A software model can easily be modified to simulate the effect different configurations has on sensor performance. An accurate model can be used to design an optimal sensor and predict sensor output for a specific configurations.

In order to determine the accuracy of the simulation model, the sensor must be tested. Since the McTronX group does not have an evaluation platform for testing PCB sensors, one must be designed and manufactured as part of this project.

A part of the sensor electronics, the drive circuit, is needed to test the sensor. The drive circuit must thus also be designed, simulated and manufactured, but will not be analysed and optimised as with the sensor.

1.3 Issues to be addressed and methodology

PCB techniques will be used to decrease sensor costs dramatically. It will also be possible to manufacture multiple sensor layouts to find an optimal design. Some of the design and manufacturing phases will therefore be done more than once. The main issues that need to be addressed in this project as well as how these issues will be addressed is presented in this section.

1.3.1 Literature study

At the beginning of project a literature survey is done on relevant topics. This gives a better understanding of the problem and serves to identify possible solutions.

A detail study into eddy current sensors and their electronics is required. The eddy current phenomenon must be understood in order to use it in a displacement sensor. The different physical

applications and layouts of modern sensors are investigated to derive a good proposed solution. The composition and operation of exciting and sensing electronics is researched. Analysis techniques that can be used in the design phase must also be researched.

1.3.2 Sensor system design

The three main parts of the senor system that must be designed are the sensor, sensor electronics and evaluation platform.

The design flow diagram, that is used to design the sensor, must first be compiled. In this stage of the project a sensor with tracks on one side of the PCB (single-sided sensor) is used. The finite element method (FEM) software package Comsol® is used to simulate the proposed sensor for various setups. The behaviour of sensor parameters e.g. sensitivity and linearity are determined using the FEM model. From these results, trends are identified that can be used to design an optimal sensor. After compiling the sensor design flow diagram, it is illustrated by applying it on the single-layer sensor.

The FEM simulation as well as analytical techniques are used to determine the requirements of the electronics. Orcad® Pspice® is used to simulate the electronics. The sensor needs to be tested once the system is manufactured in order to compare design predictions and actual results. This test setup is designed using a computer-aided design (CAD) package, Solidworks 2007®. It is used to generate manufacturing drawings. The test setup is manufactured by Instrument Manufactures of the NWU.

1.3.3 Design verification

The sensor designed according to the design flow diagram must be tested and verified in order to validate the FEM model and design process. This requires that the sensor, sensor electronics and evaluation platform be manufactured and integrated. The sensor and sensor electronic's layout are done with Orcad® Layout®.

The sensor electronics drives the sensor in order to establish the needed magnetic fields. These fields act on the conductive target that is moved by the evaluation platform in relation to the sensor. The induced voltages must be captured and demodulated in order to compare the measured and predicted results.

1.3.4 Sensor optimisation

Once the FEM model and design process is validated, it can be used to explore the effect certain parameters have on the sensor performance in order to design an optimal sensor. The parameters that can be varied include the number of windings in the excitation and sensing coils, the track width, track spacing and insulation material thickness when considering multi-layer PCBs. The performance parameters, used to determine whether a sensor is optimal, are mainly

sensitivity and linearity although the average voltage level and physical size of the sensor are also taken into account. As stated earlier, the cost will ultimately determine which design can be manufactured since the main goal of the project is delivering a low cost solution.

1.4 Dissertation overview

This section presents an overview of chapter 2 - 6.

Chapter 2 : Literature study

Some of the relevant background theory and previous work done in the eddy current displacement sensing field are included in this chapter. Displacement sensors commonly used in AMBs are discussed as well as the environment these sensors are used in. The eddy current phenomenon and its use in displacement measuring are presented. The PCB sensor is discussed in detail and a transformer model for this sensor is presented. The chapter concludes by introducing the FEM package that will be used to model the sensor.

Chapter 3 : Sensor system design

Deriving the design flow diagram and applying it to a single-layer sensor is the focus of this chapter. The mechanical and electrical constraints placed on the sensor are presented. The FEM model of the single-layer PCB is discussed in detail and the results given. From the trends found in the FEM model and analytical formulas, the optimal design flow diagram is compiled. The design of a single-layer sensor concludes this chapter.

Chapter 4 : Design verification

This chapter presents the evaluation platform and the calibration of the single-layer sensor designed in chapter 3. The parts of the evaluation platform, including the mechanical platform, target, reference sensors and drive circuitry, are discussed. The demodulation method used is described and the test results, used to verify the FEM model and design process, are presented. A good correlation between the FEM model and measured results is achieved for three different target materials.

Chapter 5 : Optimal multi-layer design

Chapter 5 starts off with the design and testing of an optimal double-layer sensor. It is shown that the sensor's output and performance correlates well with FEM model predictions. This chapter also presents the optimal design of a five-layer sensor that is not manufactured because

of cost constraints. A comparison between the single-, double- and five-layer sensor gives valuable insight into the cost vs. performance trade-off. The chapter concludes by discussing some of the other sensor parameters that influence performance and cost.

Chapter 6 : Conclusions and recommendations

The final chapter summarises the most important conclusions of this project as well as some unresolved issues that warrant future work.

1.5 Conclusion

This chapter introduced AMBs and the position sensors used in these systems. The purpose of the project is highlighted and the problem is clearly defined. The main issues to be addressed and the methodology is also presented. The literature study, presented in the next chapter, gives an overview of the most important parts of this project.

Chapter 2

Literature study

This chapter starts by introducing the reader to active magnetic bearings (AMBs). A general overview of an AMB system is given to show the importance of displacement measurement. Then commonly used displacement sensors are discussed as well as their performance parameters. Eddy current displacement sensors are also discussed in more detail, familiarising the reader with its operation. The chapter is concluded with a discussion on the finite element method (FEM) used to analyse and design the sensor.

2.1 AMBs and displacement sensors

2.1.1 Introduction to AMBs

An AMB is an advanced mechatronic system used to support a rotating axis. AMBs are non-contact bearings which uses electromagnetic fields to levitate an axis.

AMBs are well suited for use in advanced applications. No lubrication as well as no physical contact make AMBs the obvious choice in sterile environments [6]. The AMBs will not cause contamination as could be the case with other bearing technologies. Low frictional losses give AMBs the competitive edge when considering high speed applications such as machine tools [6]. This application also requires high precision which can easily be achieved with an actively controlled magnetic bearing. Very low maintenance requirements make AMBs ideal for very short downtime applications such as turbomachinery and centrifuges [6]. These machines are commonly used by vital service providers such as power generation and water distribution.

The basic components that constitute a radial AMB is shown in Figure 2.1 which includes electromagnets, a sensor system, a control system, power amplifiers and a rotor. The sensor system detects the radial position of the rotor. This information is then sent to a control system responsible for controlling the rotor position. The control system output is connected to the power amplifiers which drives the electromagnets. Electromagnets convert electrical energy supplied by the power amplifiers to mechanical energy applied to the rotor. Levitating the rotor between

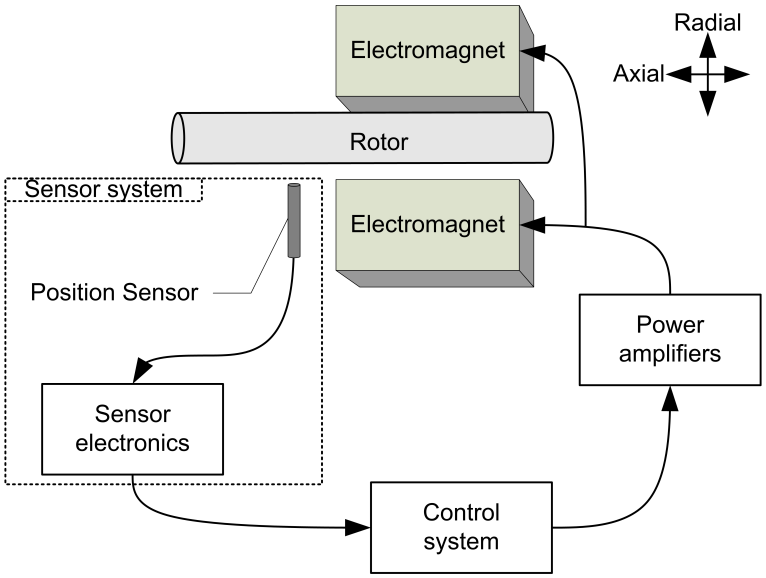

Figure 2.1: Basic radial AMB system diagram.

the electromagnets at a reference position is the main goal of this AMB [6].

The sensor system comprises of a sensor and sensor electronics, also shown in Figure 2.1. Rotor displacement is converted into an electrical signal by the sensor. This sensor signal is conditioned and amplified by the sensor electronics. Energy needed for sensor operation is supplied by the sensor electronics. Sensors used in AMBs are described in the next section.

2.1.2 Sensor characteristics and performance parameters

There are a few sensor specifications that need to be understood when specifying or designing a displacement sensor for an AMB system. In this section the specifications that are important for non-contact displacement sensing in AMBs will be discussed.

Measuring range

The measuring range of a displacement sensor is the distance over which the linearity definition of the sensor holds and is usually given in millimetres [6]. Sensing range is based on the range where there is a linear relation between the output signal and the actual displacement [16]. The start of the measuring range (SMR) is the minimum distance between the sensor tip and target. The SMR and measuring range are illustrated in Figure 2.2.

In AMBs the measuring range will normally be very small, as will be discussed in a succeeding section. Typical measuring ranges of eddy current sensors are between 0.5 mm and 80 mm. A sensor with a small measuring range also has a small SMR, typically between 0.05 mm to 1.5 mm [17].

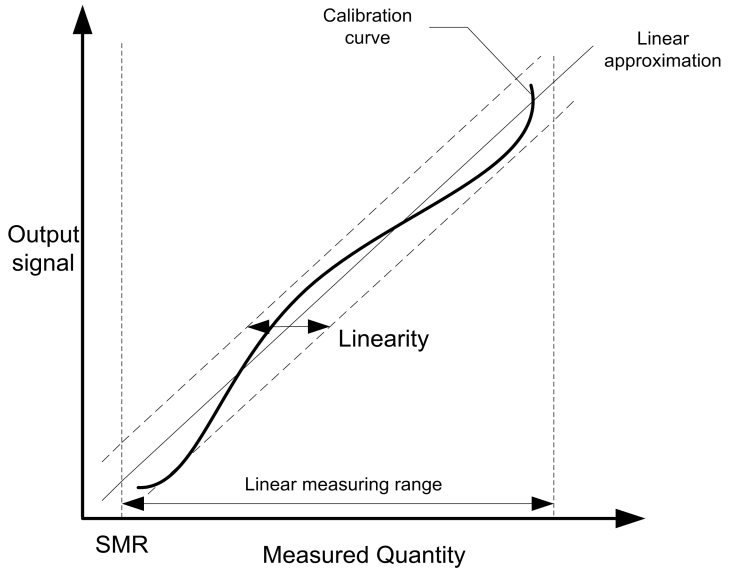

Figure 2.2: Measuring range and linearity [6].

Sensitivity

The sensitivity of a sensor is the slope of the calibration curve; sometimes called the scale factor [16]. In the case of a displacement sensor the sensitivity is given by the ration of the output signal over the displacement. The unit of sensitivity for an eddy current displacement sensor is $\frac{\mathrm{V}}{\mathrm{m}}$ [6]. Consider a sensor that has an output y which is a function of the input x. The relation $y = f(x)$ can be differentiated at point x_1 to find the sensitivity $S(x_1)$ at that point, as shown in (2.1) [16].

$$S(x_1) = \left.\frac{dy}{dx}\right|_{x=x_1} \tag{2.1}$$

It is generally true that a larger sensitivity is better. Note that the sensitivity measured at the sensor probe is smaller than the sensitivity realised at the output of the sensor electronics. The signal is amplified or scaled to be in a usable range e.g. 0 - 10 $\mathrm{V_{dc}}$, 0 - 24 $\mathrm{V_{dc}}$ or 4 - 20 mA. The sensitivity of eddy current displacement sensor systems ranges between 5 and 20 $\frac{\mathrm{V}}{\mathrm{mm}}$ [17].

Linearity

The linearity is an indication of how closely the calibration curve fits a straight line [16]. A straight calibration curve indicates a totally linear sensor. Linearity is given in a percentage of the full scale output (FSO). FSO refers to the whole range of output a sensor gives e.g. 0 - 10 $\mathrm{V_{dc}}$. The linearity is also illustrated in Figure 2.2.

The linearity will differ when using different straight line fits of the calibration curve. A few of these fits include; independent, zero-based, terminal-based, end-point and theoretical linear-

ity. Linearity is important as it gives the maximum error made when multiplying the sensor system output with a constant to find the position. When incorporating a microprocessor into the sensor electronics, the output can be linearised by using a look-up table or an nth order fitted function. Low cost, high volume produced microprocessors make this a viable option for implementing a linear sensor system with a non-linear sensor [16].

Bandwidth

The sensor has a finite bandwidth which limits the maximum rate of change in position the sensor can detect without attenuation and phase shift. When measuring rotor displacement the frequency of the target is related to the rotational speed and applied forces. Bandwidth gives an indication of the fastest change in position the sensor can detect accurately. The upper limit of this frequency range is called the cut-off frequency and occurs when the sensitivity is reduced with 3dB [6].

AMBs are used extensively in very high rotational speed applications, making the bandwidth an important factor. Consider a rotor vibrating at a frequency above the cut-off frequency. The sensor will not detect this vibration and thus the control system will not be able to compensate for this vibration. The system could become unstable or fail because of this undetected vibration. A frequency range of 0 - 10 kHz is commonly found in eddy current displacement sensors [16].

Repeatability

Repeatability gives a measure of the correlation between measurements taken by the same method, under the same conditions, in a short time interval [16]. Repeatability is given in percentage of FSO.

Repeatability is important when optimising an AMB's performance. Vibration and unbalance can be minimised by rotating the rotor around its midpoint or centre of mass. If the sensor position reading is not consistent it could worsen the vibration or unbalance. Repeatability might not cause AMB failure but it could degrade performance.

Resolution

The resolution of a displacement sensor is the smallest displacement that can be detected above the noise floor [6]. Resolution is dependent on the measuring principle, sensor's physical construction and the electronics used. It cannot be improved by amplification or modulation in sensor electronics and software. Resolution is given in either percentage of FSO or minimum displacement. Resolution can be specified for static situations where the target is stationary as well as for dynamic situation were the target is moving at a certain rotational speed or frequency [6]. The resolution is influenced by the noise present in the system. This in turn depends on varying factors that is influenced by dynamic situation of the system.

2.1.3 Position sensing in AMBs

AMBs are complex mechatronic systems which have various variables that can be measured. These include voltage, current, temperature, rotating speed, pressure and position. Position sensing is very important in an AMB system as the main control variable is the rotor position. The magnetic forces acting on the rotor are controlled to keep it at a reference position. A faulty position signal can cause the rotor to come into contact with the backup bearings or other stationary parts of the system. This causes mechanical wear on some of the components and could completely destabilise and destroy the AMB.

The position sensor location is important as it influences operation and performance. Usually the position sensor is placed very close to the electromagnetic actuator which comprises of the stator laminations and coil as shown in Figure 2.3. This is done to avoid measuring errors caused by rotor bending. Rotor bending occurs at discrete natural frequencies and if a node exists between the electromagnetic actuator and sensor positive feedback exists which destabilises the AMB. This phenomenon is called non-collocation and should be avoided. Placing the sensor close to the electromagnet can cause interference since this area is prone to stray electromagnetic fields. When using a switching power amplifier to drive the electromagnets, large electromagnetic pulses occur periodically at the switching frequency. These electromagnetic fields can contaminate the sensor and sensor wiring, causing an incorrect position reading [6].

The air-filled area between the electromagnet and rotor is called the airgap as shown in Figure 2.3. The force (f) applied to the rotor by the actuator's magnetic field is inversely proportional to the square of the airgap length (s). This can be seen in (2.2) with the number of conductor turns n, cross-sectional area A_a and current i. Airgap length is normally only a few tenths of a millimetre [6]. The total radial movement (when considering a radial AMB) is limited to less than two times the airgap. This means the displacement sensor has a very small range and must be very sensitive to radial rotor movement. The displacement sensor in an AMB system must never be in physical contact with the rotor. The high rotational speeds of the rotor would cause extensive wear to a contact sensor. For this reason AMBs necessitate non-contact position sensors. These are some of the factors that must be considered when designing and

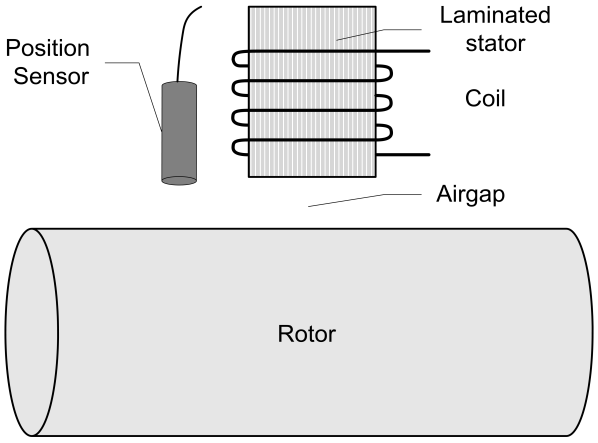

Figure 2.3: Radial AMB position sensor placement.

implementing a position sensor in an AMB. Different types of displacement sensors used in AMBs are discussed in the next section.

$$f = \frac{1}{4}\mu_0 n^2 A_a \frac{i^2}{s^2} \tag{2.2}$$

2.1.4 Different types of position sensors used in AMBs

The most common types of displacement sensors used in AMBs, according to [6], is introduced in this section. These sensors are all named after the operating phenomenon and an inductive displacement sensor will be discussed first.

Inductive position sensor

This sensor's operation will be explained with the use of Figure 2.4. It comprises a coil situated in a ferrite core. This coil forms part of an oscillating circuit. The coil's inductance changes when there are relative movement between the ferromagnetic target and the sensor. This detunes the oscillating circuit and thus changes the oscillating frequency. This change in frequency is proportional to the distance between the sensor and the target.

The modulating frequency of inductive displacement sensors are between 5 and 100 kHz. These sensors are usually not very susceptible to external magnetic interference since it is shielded by the ferrite core. There are cases where disturbances can occur when the AMB's are driven by switch mode power amplifiers that operates at frequencies close to the modulating frequency [6]. Bandwidth of this type of sensor could be too low for high speed applications. This sensor has a very good linearity and range well suited for AMBs. Inductive sensors are commonly used in AMBs [5]. Various patents has been grated for inductive displacement and proximity sensors [18].

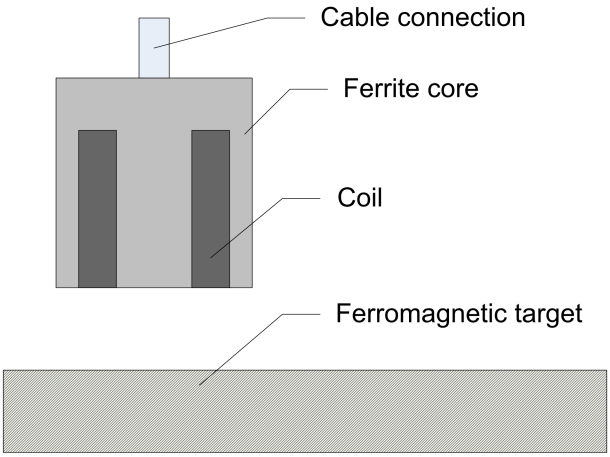

Figure 2.4: Inductive displacement sensor [6]

Capacitive position sensor

Changing the distance between a plate capacitor and target causes a change in capacitance of the capacitor. In this type of sensor the capacitor is excited with an alternating current and is shown in Figure 2.5. The amplitude of this signal is demodulated to yield he displacement as it is proportional to the clearance between sensor and target. This sensor typically has a good resolution as well as a bandwidth between 5 kHz and 100 kHz. The disadvantage of this type of sensor is the intolerance to dirt in the clearance; this changes the dielectric properties of the capacitor [6].

This type of sensor can be manufacture on a printed circuit board (PCB), as demonstrated in [19]. The advantages of PCB sensors are low cost and high repeatable manufacturing proses. The PCB capacitive sensor has a good resolution and low signal-to-noise ratio. This type of sensor is thus well suited for use in clean environments.

Optical position sensor

In optical sensing the obstruction of light rays is used to determine a target's position. This sensing principle requires a light source and light detector. The light detector outputs a voltage proportional to the intensity of the light shining on it. Movement of the target causes a change in the intensity of light shining on the detector. There are various ways to implement this phenomenon, mainly; Light barrier principle, refection principle and charge-coupled sensor. The light barrier principle is illustrated in Figure 2.6.

Optical sensors have very linear response when appropriate light sources and detectors are used. High bandwidth can be realised as light is a high frequency signal. This type of sensor is susceptible to dust and is mostly used in clean environments. The components used in this sensor cannot be manufactured without specialised equipment. Mass production of the components means this type of sensor is usually a cost efficient solution [6].

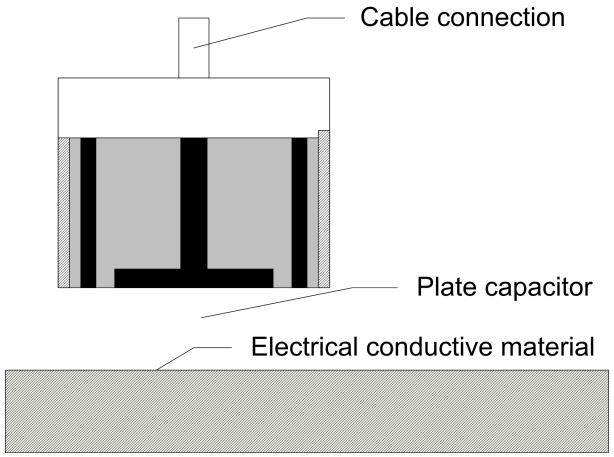

Figure 2.5: Capacitive displacement sensor [6]

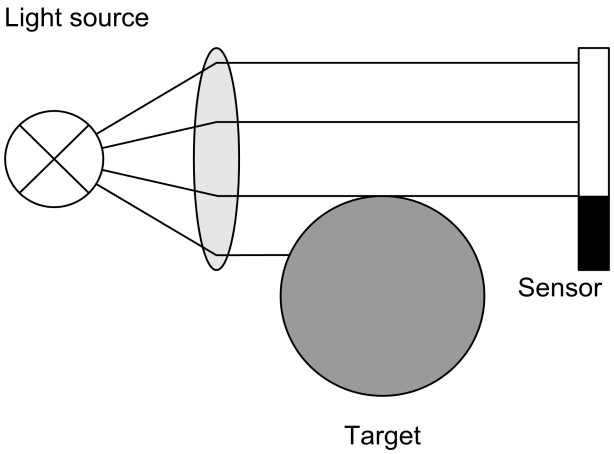

Figure 2.6: Optical displacement sensor [6]

Eddy current position sensor

The eddy current position sensor is similar to the inductive position sensor. A coil is also used as the probe as shown in Figure 2.7. This coil is not inclosed in a ferromagnetic core as the inductive sensor. The frequency of the drive signal is a lot higher than the inductive sensor, between 1 and 10 MHz. At these frequencies the eddy current losses are large and proportional to the coil's position relative to the target. Targets used with inductive sensors must be ferromagnetic, with eddy current sensors electrical conductivity is the prerequisite. The higher excitation frequency means eddy current sensors are less susceptible to noise caused by power amplifier switching [6]. Eddy current sensors are not influence by dust and dirt in the airgap unless these impurities are electrical conductive. The bandwidth of these sensors are 0 - 20 kHz.

This concludes the introduction to the most commonly used displacement sensors for AMBs.

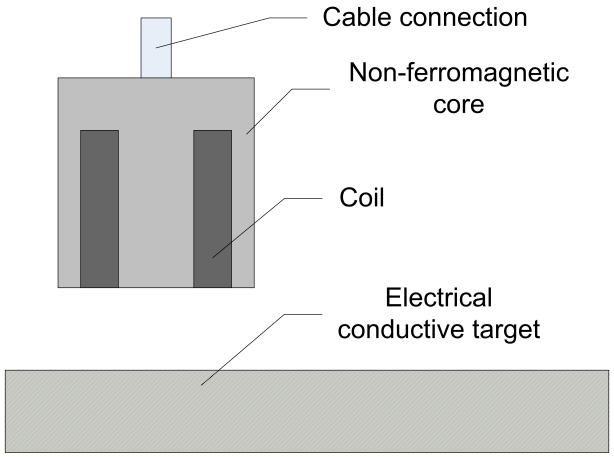

Figure 2.7: Eddy current displacement sensor [6]

This study will focus on eddy current displacement sensors and the next section will be dedicated to discussing this in more detail.

2.2 Eddy current displacement sensors

The environment and requirements of displacement sensors were introduced in the previous section as well as a few commonly used displacement sensors. This section will explain the use of eddy currents in displacement sensing. Two types of eddy current displacement sensors will be explained in detail.

2.2.1 The eddy current phenomenon

The word eddy is commonly used when describing water moving in a circular pattern like a small whirlpool [7]. Eddy or Foucault currents were first documented by J. D. L. Foucault in 1851. Eddy currents are induced in a conductive material whenever it is placed in a changing magnetic field. Figure 2.8 shows a current carrying wire, placed around a piece of cylindrical, conductive material. When an alternating current is flowing through the wire, a changing magnetic field is present around the conductor. This magnetic field will penetrate the conductive material when in close proximity of the wire. A voltage will be induced in the material by the changing flux as stated in Faraday's law [9]. The conducting material will provide a path for the resulting current. This current will be in a direction creating a magnetic field that opposes the field established by the current carrying wire, in accordance with Lenz's law [9]. The eddy current will thus try to eliminate the magnetic flux in the conductive material [8].

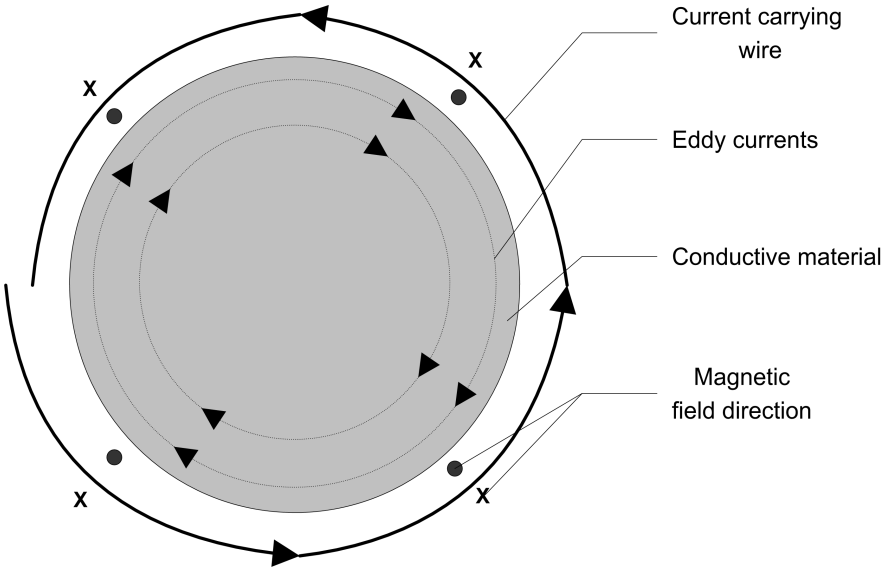

Figure 2.8: Eddy currents in cylindrical conductive material.

Eddy currents is best known as an energy loss component found in electrical machines such as motors and transformers. Together with hysteresis loss it forms the magnetic losses in electrical machines. Eddy current loss is countered by using laminated magnetic cores which forces the eddy current to flow in long, narrow paths. Eddy current losses are proportional to the square of the frequency of the current flowing through the conductors[20]. This makes it a big problem in AMBs with high frequency currents due to switching power amplifiers.

The eddy currents has an effect on the magnetic flux as well as the magnetic field distribution. Both of the above are dependent on the physical placement and geometry, which makes it possible to use the eddy current phenomenon to measure movement of conductive materials. As an example note that the change in the amplitude of the flux will change the inductance of a coil. Self inductance (L) is defined as the ratio of a incremental change in the magnetic flux (Φ) to a incremental change in the current (i) [20], given by (2.3), with N the number of turns in the coil.

$$L = N\frac{d\Phi}{di} \simeq N\frac{\Delta\Phi}{\Delta i} \tag{2.3}$$

Using the eddy current phenomenon to measure displacement has a few advantages. The eddy currents are not effected by the substance between the sensor and target, unless the substance is electrically conducting. This means that the eddy currents will not be influenced by irregularities such as dirt, dust and oil [4]. The target needs only to be conductive and not necessarily magnetic. Alloys such as stainless steel, commonly used for manufacturing high speed rotors, are non-magnetic and conductive. The amplitude of the eddy currents depend on the conductivity of the target[10].

2.2.2 Standard eddy current displacement sensor

Eddy current displacement sensors have been patented from as early as 1975 [11]. Figure 2.9 shows one of those sensors which has automatic temperature compensation. This is done by using a phase locked loop to automatically adjust the oscillating frequency of the circuit. The sensors usually has a resonant tank circuit; in this figure formed by the capacitor C_0 and sensing coil 3. A change in displacement would cause a change in the coil's inductance and thus change the oscillating frequency. This change in frequency is used to provide a position output.

Consider a sensor coil and target with the current flowing in a clockwise direction as shown in Figure 2.10. This will cause a magnetic field that points downward inside the coil and upwards outside the coil, according to Biot-Savart's law [21]. The magnetic field will induce eddy currents flowing in a counter-clockwise direction on the surface of the conductive material. A magnetic field is establish that opposes the field established by the coil. If the coil is moved closer to the target, the eddy currents induced will be larger, causing a bigger opposing magnetic field. This influences the total magnetic flux in the coil and thus also the coil's inductance as discussed in the previous section.

The sensor shown in Figure 2.10 can also be represented by the equivalent circuit shown in Figure 2.11. This model is based on the electrical transformer as discussed in [10],[22]. The

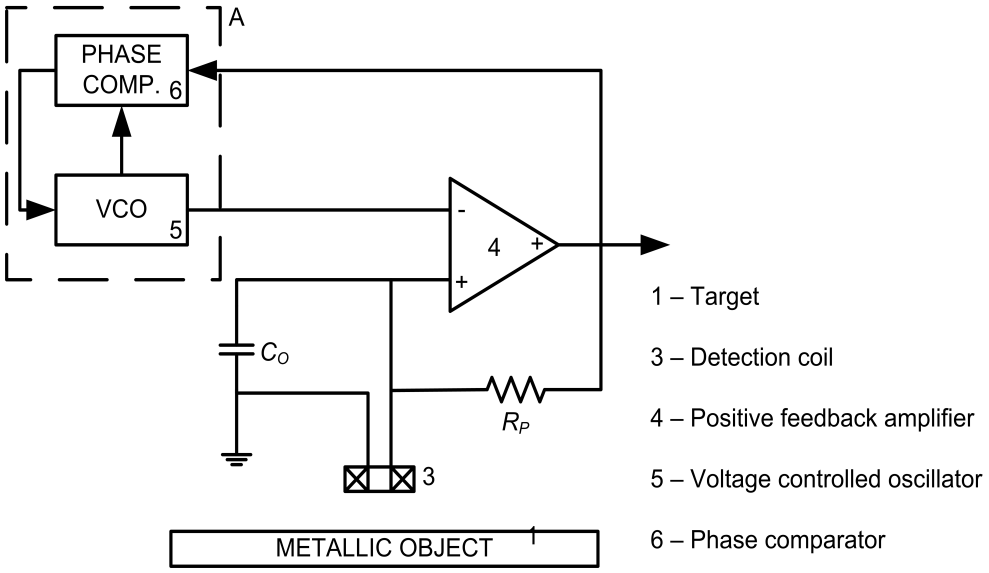

Figure 2.9: Eddy current sensor of 1980 [12].

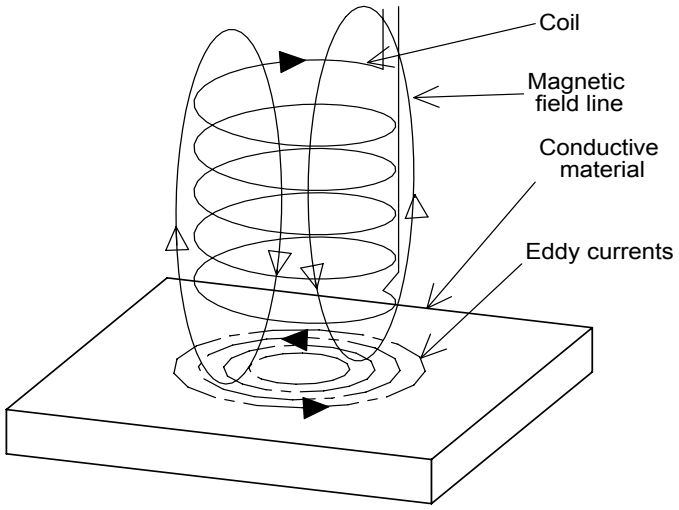

Figure 2.10: Eddy current displacement sensor coil [22].

multi-turn coil is driven by an alternating current source (delivering a peak current I_C), causing a peak voltage V over the coil. Each turn of the coil consist of a resistor (r), inductor (l) and eddy current induced voltage (u). The eddy current paths can be divided into N cylindrical rings which has an equivalent circuit consisting of a resistor (ρ), an inductor (λ) and the voltage induced (e). These components form a closed loop for each conducting ring, carrying the eddy current (i). Note that the eddy currents do not flow in the radial direction, thus no current flows between the conductive rings. There is mutual inductance (M) between a winding and conductive ring, mutual inductance (γ) between the windings of the coil as well as mutual inductance (m) between the conductive rings [23].

The main advantage of the standard eddy sensor is that this configuration applies the eddy current phenomenon in the most sensitive way. These sensors have been researched extensively thus equivalent circuits and simulation results are well documented. These sensors are also commonly used in nondestructive testing [24]. This type of sensor also has a few disadvantages when used in AMBs. The probes are normally placed in threaded enclosures. An example of such a probe can be seen on the right of Figure 2.12. It is difficult to position these sensors accurately, up to a few micro metres, in the AMB. These sensors take up a significant amount of radial space in the AMB, which could better be used as part of the actuator [4]. The measuring coil of these sensors are usually constructed from very thin wire which must be wound very precisely. The coil is normally wound by hand under a microscope, making manufacturing very labour intensive and expensive [15]. In order to measure the radial movement (x and y) at least two of these sensors are needed.

This concludes the discussion on the standard eddy current sensor. A different way to apply eddy current sensing is presented in the next section.

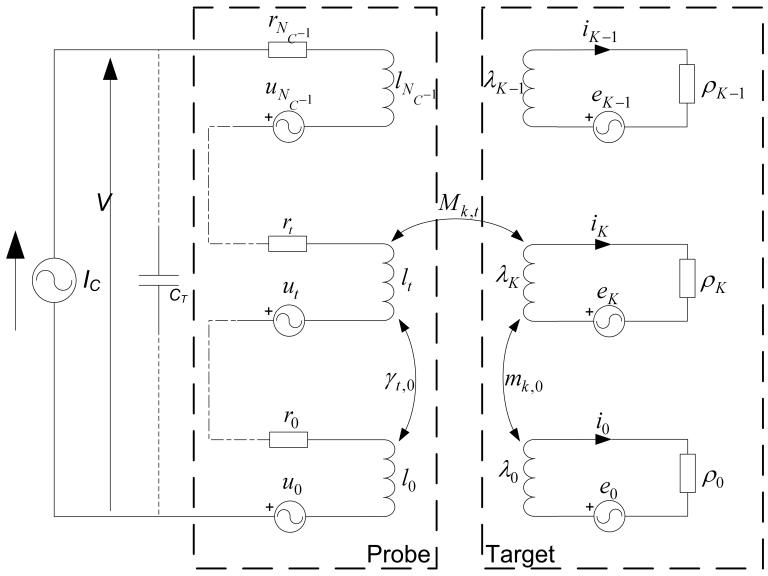

Figure 2.11: Eddy current displacement sensor transformer model [23].

Figure 2.12: Micro Epsilon eddy current displacement sensor [17].

2.2.3 PCB eddy current displacement sensor

A printed circuit board (PCB) based eddy current displacement sensor was patented by P. Bühler in 2002 [14] and is shown in Figure 2.13. The target of the sensor is a round rotor (2) which can move radially and thus cause a change in the airgap (10) size. A high frequency current flows in a coil (1) that surrounds the target. The secondary coils (4) are used monitor the rotor radial movement. All the coils are placed on an insulating substrate (14), commonly found in PCBs.

Figure 2.14 shows a vertical cut view of the PCB sensor when the current is flowing into the right part of the current carrying coil. The high frequency alternating current carrying coil is located around the electrical conductive target. The alternating current will cause an alternating magnetic field around the current carrying coil as stated by Biot-Savart's law [21]. This magnetic field will then induce eddy currents that flow on the surface of the rotor as stated by Faraday's law [9]. These eddy currents will flow in a direction that opposes the current in the coil. The primary magnetic field is weakened by the eddy current magnetic field. This results in less of the primary magnetic field linking with the detecting coil, thus inducing a smaller voltage where the target is closer.

To further explain the operation of the sensor and to derive an equivalent circuit, Figure 2.15 is used. The sensor and rotor top view is shown for two rotor positions; target in the middle and target in the top right position. Assume the current flows in a counter-clockwise direction to establish a magnetic flux flowing into the page in the area of the detector coils. When the rotor is in the middle the magnetic flux through the respective detector coils are the same as well as the eddy currents flowing on the surface of the rotor. In this case the voltage induced in the different detector coils are the same; induced voltage is directly proportional to the amount of magnetic flux passing through the coil. When the rotor is moved into the upper right corner a larger voltage will be induced in that part of the rotor and a smaller voltage in the lower left area. The magnetic flux in the upper right detector coil will be smaller and the flux in the lower left detector coil larger.

The magnetic flux density decay in the movement range of the rotor is shown in Figure 2.16. It can be seen that the magnetic flux density decays almost linearly with position. When the rotor

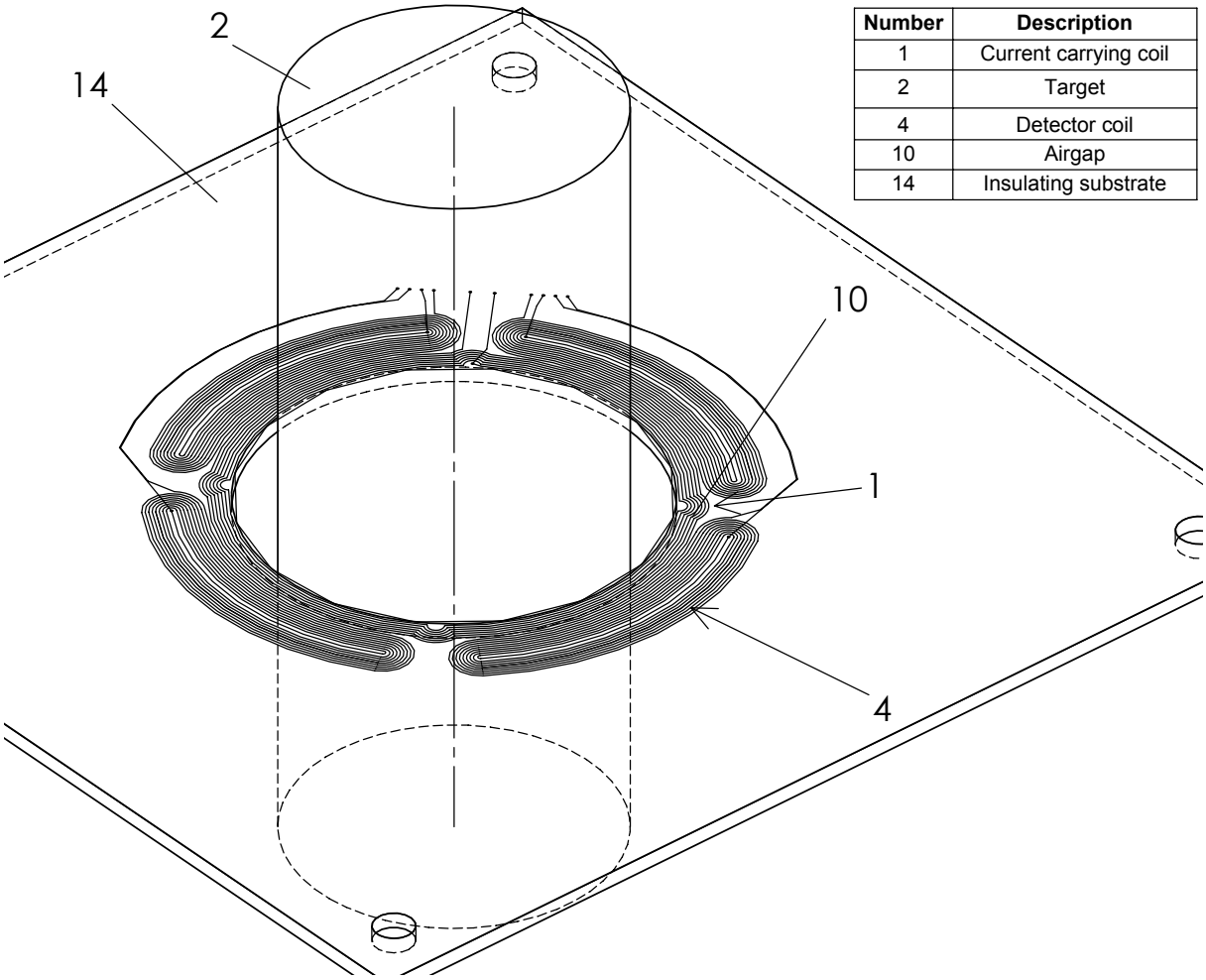

Number	Description
1	Current carrying coil
2	Target
4	Detector coil
10	Airgap
14	Insulating substrate

Figure 2.13: Mecos PCB eddy current displacement sensor [14].

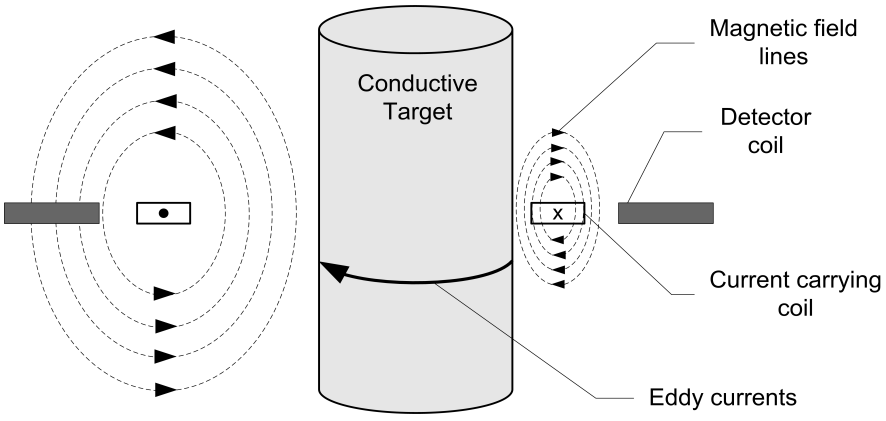

Figure 2.14: PCB eddy current displacement sensor operation [4].

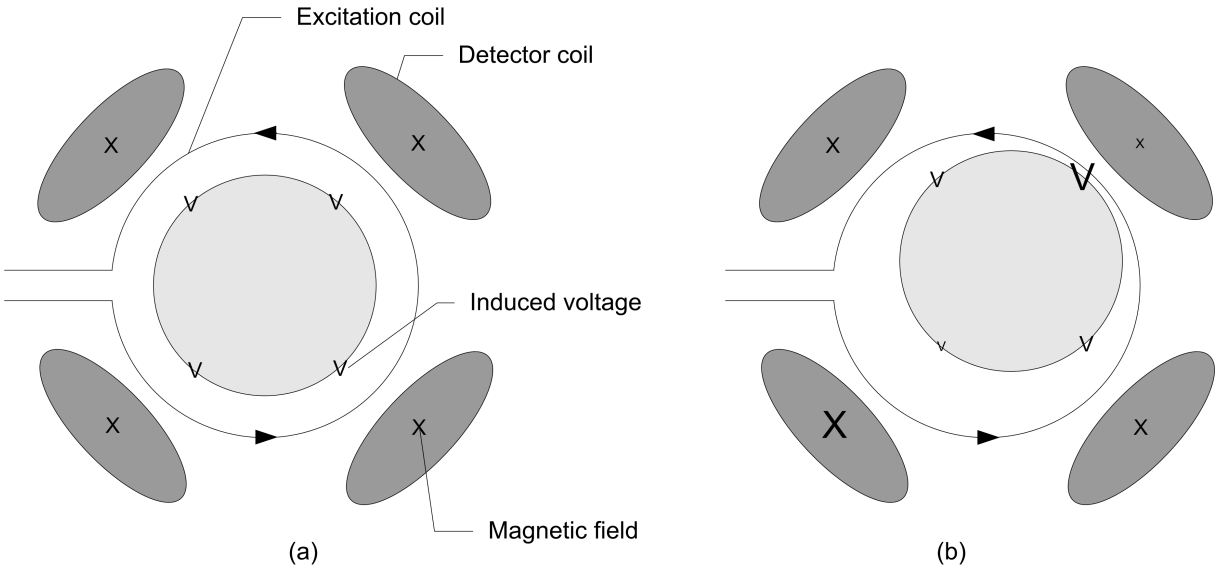

Figure 2.15: Top view of PCB sensor with (a) the target in the middle. (b) the target on the right top corner.

moves closer to the sensor on one side the opposite side of the rotor will move further from the sensor. The linearity of the magnetic flux density decay causes the sum of the induced voltages to remain constant. All the induced voltages are connected in series through the conducting ring of the target. The amplitude of the eddy current will remain constant regardless of where the rotor is inside the sensor.

The equivalent transformer circuit for the PCB type sensor is shown in Figure 2.17. The excitation coil is driven by a high frequency current source, delivering a peak current of I_C. The

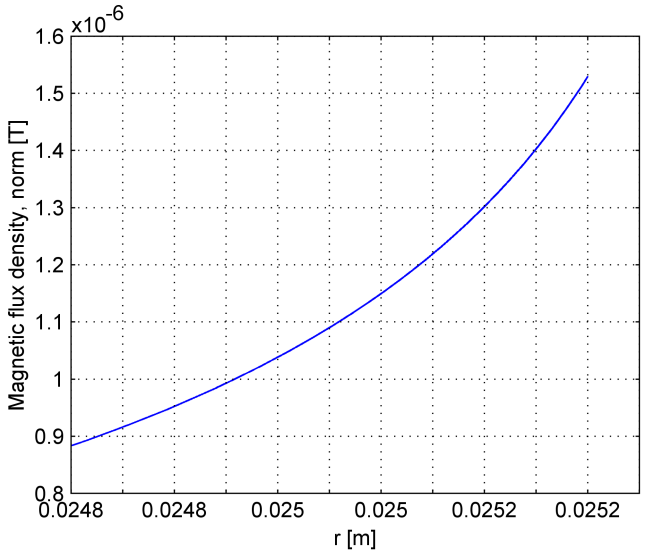

Figure 2.16: FEM generated magnetic flux decay over rotor movement range.

excitation coil consists of the conductor resistance (r), coil inductance (l) and an eddy current induced voltage (u). The eddy current conducting ring constitutes the material resistance (ρ), inductance (λ) and induced voltage (e). The PCB sensor also has four sensing coils with inductance ($\alpha_1 - \alpha_4$) and termination resistances ($R_1 - R_4$). These resistors will have large values, limiting the current flow in these coils to low levels. The voltage across the resistance will be used to determine position. The mutual inductance (M) between the excitation coil and target stays constant as discussed in the previous paragraph. A change in the mutual inductance (m) between the excitation coil and sensing coils causes a change in induced voltage on the sensing coils.

The disadvantage of using this kind of sensor is that the eddy current effect is not used in the most sensitive way. This specific configuration is also not widely documented. There are significant advantages offered by this PCB type sensor. Detector electronics only needs to amplify and linearise the sensing coil voltages. Manufacturing of this kind of sensor is very cost effective and the manufacturing technique yields high repeatability. Only one sensor is used to measure both the x and y radial movement. Axial movement and rotational speed can also be measured with this sensor by only modifying the detector electronics. This sensor takes up very little radial space, making a more compact AMB possible. Measurement with this sensor is done in differential mode, making it less susceptible to noise and temperature effects.

This concludes the discussion of eddy current displacement sensors for AMBs. In the next section the analysis tool that will be used in the design of a PCB sensor is introduced.

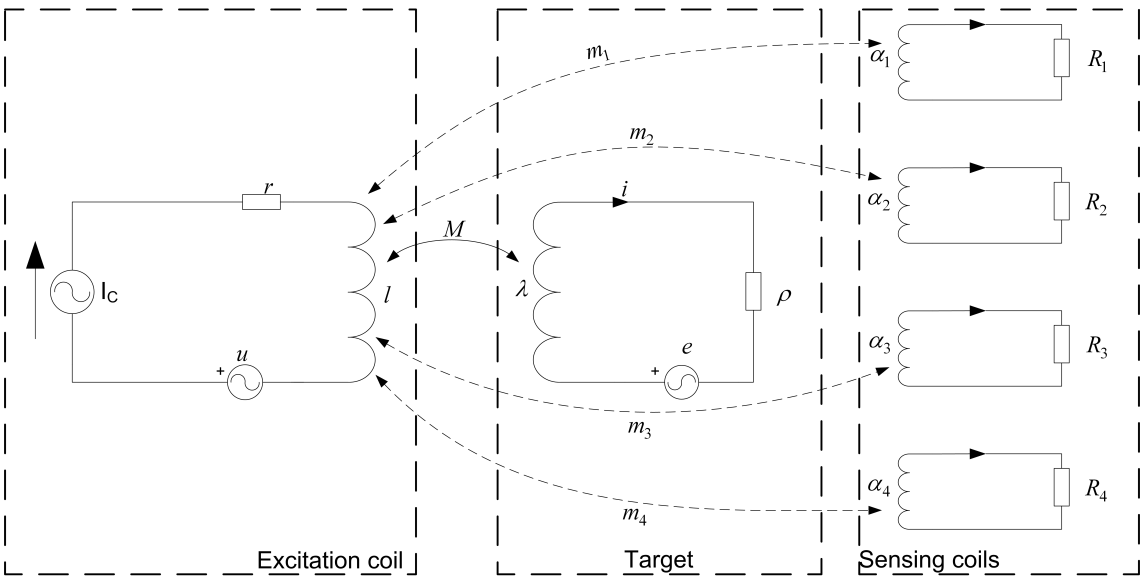

Figure 2.17: Equivalent circuit of PCB type sensor.

2.3 Finite element method (FEM)

In order to fully understand the complex reality humans regularly reduce large problems into smaller problems. This concept also forms the bases for FEM, solving a large, complex problem by dividing it into a finite number of smaller, solvable problems [25]. The FEM as it is known today was first suggested by R. W. Clough in 1960 [26]. The idea can be traced back to a mathematician, R. Courant's, paper of 1943. Computers capable of solving these calculation intensive analysis only became available in the 1950's. In these early years FEM was used in aerospace and aeronautical engineering to give designers an idea of structural performance without first building a prototype. Currently the FEM is used in various disciplines including structural, nuclear, electronic and mechanical engineering [27].

Engineering problems can be solved by deriving differential equations that describe the variables involved in the problem. To solve linear (and sometimes nonlinear) partial differential equations is quite challenging, even impossible. By dividing a complex geometry into finite elements, the differential equation problem is reduced to an algebraic problem. A computer can be used to solve the algebraic equations that describe the problem, calculating the answer for each node [27]. Using FEM to analyse electromagnetic systems such as non-contact displacement sensors has various advantages. Magnetic fields, magnetic flux and eddy currents are abstract, invisible concepts, making them difficult to understand. A FEM software package such as Comsol Multiphysics® can visually represent these phenomenon. This program can also be used to test the viability of a sensor and evaluate its performance in various environments without manufacturing a prototype for each situation.

The number of nodes in the geometry directly influences the resources needed to solve it. In some cases the three dimensional reality can be approximated with a two dimension model without lowering the accuracy of the model extensively. Figure 2.18 shows how the PCB sensor can be approximated with a two dimensional model. This simulation will be discussed in more detail in chapters to come. The eddy currents flow in the outside ring on the rotor, thus axial symmetry Quasi-Statics Azimuthal Currents application mode of Comsol® can be used.

The first step in modelling with FEM is drawing/defining the geometry, in this case a two dimensional sketch. This sketch must also include a boundary that limits the solution region. The next step is defining the electromagnetic properties. Three electrical properties that must be defined, starting with permittivity (ϵ) as in (2.4) with electric flux density ($\overline{D}$) and electric field density ($\overline{E}$). Permeability (μ) is defined in (2.5) with magnetic flux density ($\overline{B}$) and magnetic field density ($\overline{H}$). Conductivity (σ) is also defined in (2.6) where ($\overline{J}$) is the current density. The magnetic field can be established with electrical currents or permanent magnets [27]. The current density in the excitation component must also be assigned.

$$\epsilon = \frac{\overline{D}}{\overline{E}} \tag{2.4}$$

$$\mu = \frac{\overline{B}}{\overline{H}} \tag{2.5}$$

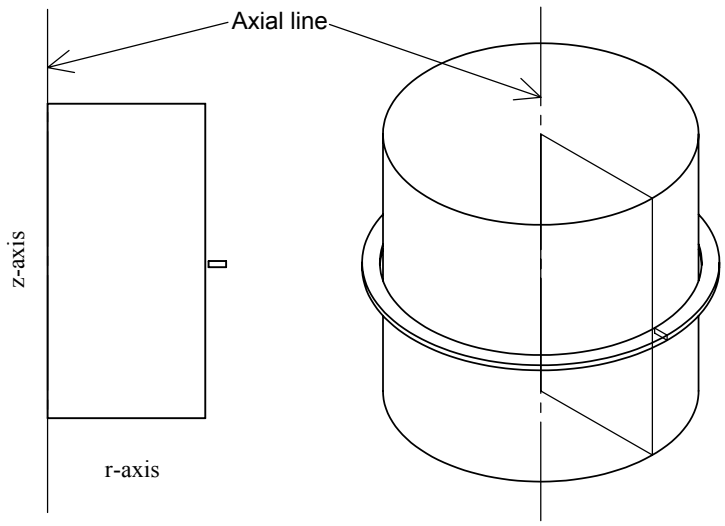

Figure 2.18: Axial symmetry approximation of the sensor

$$\sigma = \frac{\bar{J}}{\bar{E}} \tag{2.6}$$

The next step is dividing the geometry into a finite number of triangles. This process is called creating the mesh. Note that the elements will be smaller in areas with smaller geometry details [27]. The electric and magnetic fields are now solved at all the node points by using the governing equation (2.7) [28]. This equation uses the angular frequency (ω), voltage applied to the loop ($\mathbf{V}_{loop}$) and current density due to an external source ($\mathbf{J}^e_\varphi$).

$$(j\omega\sigma - \omega^2\varepsilon)\mathbf{A}_\varphi + \nabla \times (\mu^{-1}\nabla \times \mathbf{A}_\varphi) = \frac{\sigma \mathbf{V}_{loop}}{2\pi r} = \mathbf{J}^e_\varphi \tag{2.7}$$

By integrating the current density calculated in (2.7) the current flowing in the loop (I) can be calculated as shown in (2.8).

$$\int_S \mathbf{J}^e_\varphi . ds = I \tag{2.8}$$

The FEM model is used in the design process were analytical models are not viable or available. It can be used to investigate the effect changing the geometry and materials used without manufacturing multiple sensors. An important step when using a FEM model is verifying the model with practical results measured on a designed sensor. When discrepancies are found, these should be used to refine the model to more closely approximate the reality.

2.4 Conclusion

This chapter presented some background on AMBs and the sensors used in these systems. Some of the most important sensor characteristics and performance parameters were discussed. Rotor position is the main control variable in an AMB system. It is discussed in terms of how position should be measured as well as some of the commonly used types of position sensors. Eddy current sensors are the main focus of this project and were discussed in detail. The chapter concludes by presenting the FEM that will be used in the eddy current displacement sensor design process.

Chapter 3

Sensor system design

This chapter presents the design process for a PCB based eddy current displacement sensor. First the sensor constraints are discussed to set forth the requirements of the sensor. Next the FEM model, used to simulate the sensor, is explained. This model will be used to understand sensor behaviour and compile a design flow diagram. Finally a single-layer optimal PCB sensor is designed to illustrate the design flow diagram.

3.1 Sensor constraints

The goal of this project is to design an optimal PCB based eddy current displacement sensor for use in AMBs. This section will introduce the sensor requirements as well as some constraints.

3.1.1 Mechanical constraints

Mechanical constraints are the physical limitations that must be considered in the sensor design. These limitations are illustrated in Figure 3.1. The mechanical constraints are influenced by the AMB environment the sensor will work in and the PCB manufacturing techniques.

Sensor measuring range

The total radial movement range (w_{mr}) of the rotor is limited by the backup bearing. This movement range is the displacement that must be measured with the sensor and is shown in Figure 3.1. The sensor's measuring range is determined by the backup bearing which in turn is influenced by the airgap between the electromagnet and rotor. In most cases this airgap is designed to be very small since the magnetic force is inversely proportional to the square of the airgap, as described by (2.2). The sensor measuring range is usually a few tenths of a millimetre.

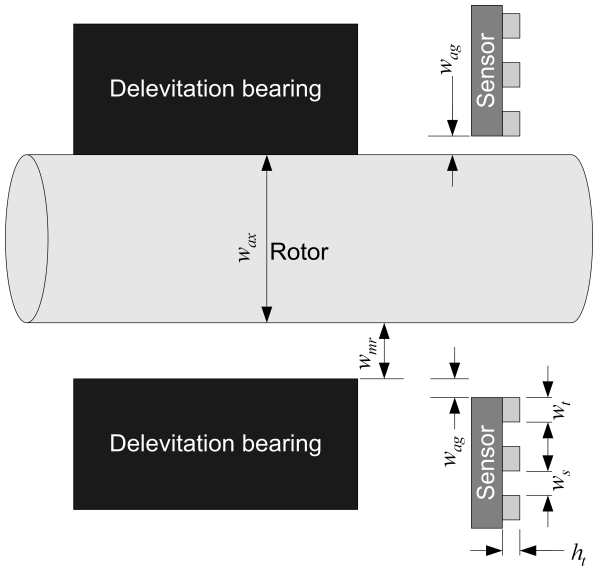

Figure 3.1: Mechanical limitations side view.

Sensor airgap

The distance between the edge of the backup bearing and the edge of the sensor is the airgap width (w_{ag}). This is the distance between the sensor and rotor when the rotor is in contact with the backup bearing. It must be large enough to ensure the sensor is not damaged when a delevitation occurs and is also shown in Figure 3.1.

Axis diameter

The axis diameter (w_{ax}) gives the size of the sensor target and is shown in Figure 3.1. Axis diameter is determined by the application the AMB will be used in. The rotating speed and forces applied to the rotor are considered when designing the rotor.

Track height

The track height (h_t) is determined by available PCB sheet copper thickness and is indicated in Figure 3.1. The copper thickness is specified in ounces (oz) with 1 oz being approximately 35 nm thick. Standard PCB copper thicknesses are 0.5, 1 and 2 oz.

Track width

The track width (w_t) is dependent on the manufacturing process used to build the sensor and is shown in Figures 3.1 and 3.2. Modern manufacturing processes make it possible to construct very thin tracks on a PCB. Very thin tracks can cause the sensor cost to increase and limit the

manufacturers able to construct the sensor. A thinner track is also more fragile and could easily be broken if not handled carefully.

Track spacing

The track spacing (w_s) is also dependent on the manufacturing process. Using a milling machine with a v-shaped tip to manufacture the PCB is an example of this constraint. The machine must mill out the copper to a set depth to separate the copper tracks, thus placing a limitation on the gap width. Track spacing and track width usually have the same minimum value.

Via diameter

Manufacturing capabilities limit the via diameter (d_{via}), indicated in Figure 3.2. A via is used to establish an electrical connection between different layers of a PCB. Vias are used in this sensor to provide return paths for the currents flowing in planar coils. This limitation influences the sensor performance. Placing a large via causes some of the sensing coil windings to be further away form the excitation coil. This makes the voltage induced on the sensing coil smaller which in turn makes the sensor less sensitive for a change in position.

Sensing coil angle

The sensing coil angle (ϕ) gives an indication of how much of the radial space of the target will be measured by a specific sensing coil. When four sensing coils are used the theoretical maximum sensing coil angle is 90 °. This cannot be realised practically because of the specific coil

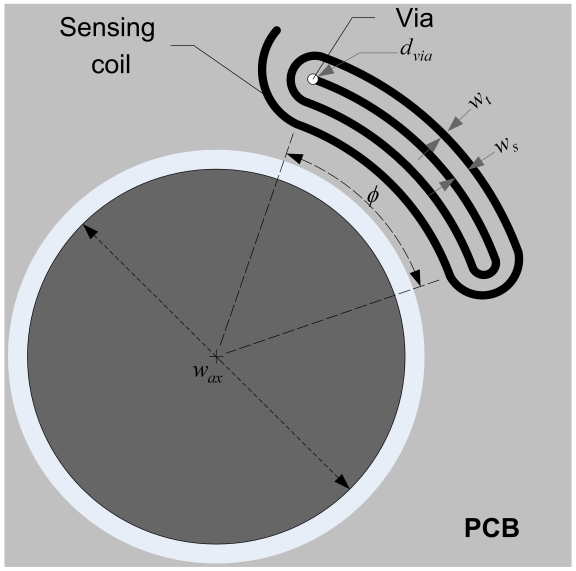

Figure 3.2: Mechanical limitations top view.

profile. A large sensing coil angle ($\phi > 80^\circ$) could cause large cross-coupling effects between adjacent sensing coils. Figure 3.2 shows a sensing coil where $\phi = 50^\circ$.

3.1.2 Electrical constraints

These constraints are influenced by the sensor probe and sensor electronics.

Supply power

The excitation circuitry must drive the excitation coil at a constant current, thus eliminating the effect temperature has on the coil's resistance. The maximum voltage that can be applied to the excitation coil is influenced by the electronic components in the excitation circuit. The supply voltage is set at -15 to 15 V_{dc}. This correlates with a maximum rms voltage of 10.6 V_{rms} applied to the excitation coil, limiting the coil's inductance when the current is controlled at 0.1 A_{rms}.

Output voltage range

The sensor's output is a voltage proportional to the position of the rotor. The output voltage range must be compatible with the controller which uses the voltage to control the rotor position. A voltage range of 0 - 10 V_{dc} is chosen as it is compatible with current hardware used in McTronX AMBs.

Operating frequency

The excitation frequency of an eddy current sensor is usually between 1 and 10 MHz. The operating frequency influences the penetration depth and excitation coil inductance. It is also important when designing the excitation circuitry and demodulation circuitry connected to the sensing coils.

Sensitivity

Sensitivity is one of the most important sensor system characteristics as it directly influences the sensor performance and electronic designs. A large sensitivity is desirable as it minimises the negative effects of noise. It also has a positive influence on the sensor resolution. The sensor's sensitivity (S) can be calculated using (3.1) with output voltage range (ΔV) and measuring range (Δx).

$$S = \frac{\Delta V}{\Delta x} \tag{3.1}$$

Linearity

The linearity of the sensor also influences all the subsystems of the sensor system. A very linear sensor output will simplify the sensing circuitry and subsequent signal conditioning. The linearity should be at least 6 % FSO which is the specification for an eddy current displacement sensor with a similar measuring and output voltage range [17].

3.1.3 Design outcomes

The goal is to derive the process for designing an optimal PCB displacement sensor. The sensor is modelled using Comsol® to investigate the sensor behaviour. The primary investigated variable is the voltage induced in the sensing coil. When the voltage is known for different airgaps, the sensitivity and linearity can be determined. A design flow diagram can be derived using this data for different sensor setups. The number of excitation windings, number of sensing windings, excitation frequency and target material are some of the sensor parts that can be changed to investigate their effect. The dimensions used in the FEM model section are based on the specification for a single-layer sensor, shown in Table 3.1

3.2 FEM model

The FEM model is used as a design tool and will be discussed in this section. An overview of the steps involved is given as well as results. These will be used to derive the optimal flow diagram discussed later in this chapter.

3.2.1 FEM model development

In order to compile the FEM model a few steps must be followed. These include; drawing the geometry, defining the materials used in the geometry, creating the mesh and finally solving the model.

Draw the geometry

The sensor probe shown in Figure 2.13 is modelled using Comsol Multiphysics®. The sensor is assumed to be axially symmetrical and can thus be approximated by the geometry shown in Figure 3.3. The rotor is represented by a rectangle. The excitation coil is also represented as a rectangle of track height (h_t) and width of the whole excitation coil $\{n_{exc} \times (w_s + w_t)\}$. The excitation coil's individual tracks are not modelled as this would increase the number of nodes that must be solved with no significant improvement in model accuracy. This approximation has a similar magnetic field pattern as individual tracks and the same response is expected.

The sensing coil is represented by a line equal to the radial length of all the sensing coil tracks combined $\{2 \times n_{sens} \times (w_s + w_t)\}$. Only the amount of magnetic flux passing through the sensing coil is important when calculating the voltage induced in the sensing coil.

These assumptions have an effect on the results that can cause the model to differ from the practical system. All the materials are assumed to have completely smooth edges. In reality the target's manufacturing process used cannot guarantee a completely smooth surface. The skin depth or penetration depth indicates the depth a signal of frequency (f) penetrates a material with a certain permeability (μ) and conductivity (σ) as shown in (3.2) [29]. This is determined for some of the materials commonly used in AMB rotors e.g. aluminium (Al), mild steel (Fe) and AISI 304 Stainless steel (304Ss) as shown in 3.3. The shin dept is very small compared to the rotor diameter. This means that surface irregularities have a significant effect on the correlation between simulation and practical results. Irregularities in the magnetic field can be caused by material impurities. This could cause a false reading since the sensing coil voltage is proportional to the magnetic field.

$$\delta = \sqrt{\frac{2}{2\pi f \mu \sigma}} \tag{3.2}$$

In the model the rotor is stationary, thus the rotating effects are ignored. The surface and material irregularities mentioned above could cause a noise component at the rotational frequency to be induced on the position signal. The signal operational frequency is significantly higher than the rotational speed, thus this noise component can easily be filtered out.

The resistance and inductance of the coils cannot be determined when using this FEM model were the coils are approximated with one coil. These parameters are directly related to the number of windings of the coil. When all the individual coils are included in the FEM model these parameters can be determined but this makes the model more computational intensive.

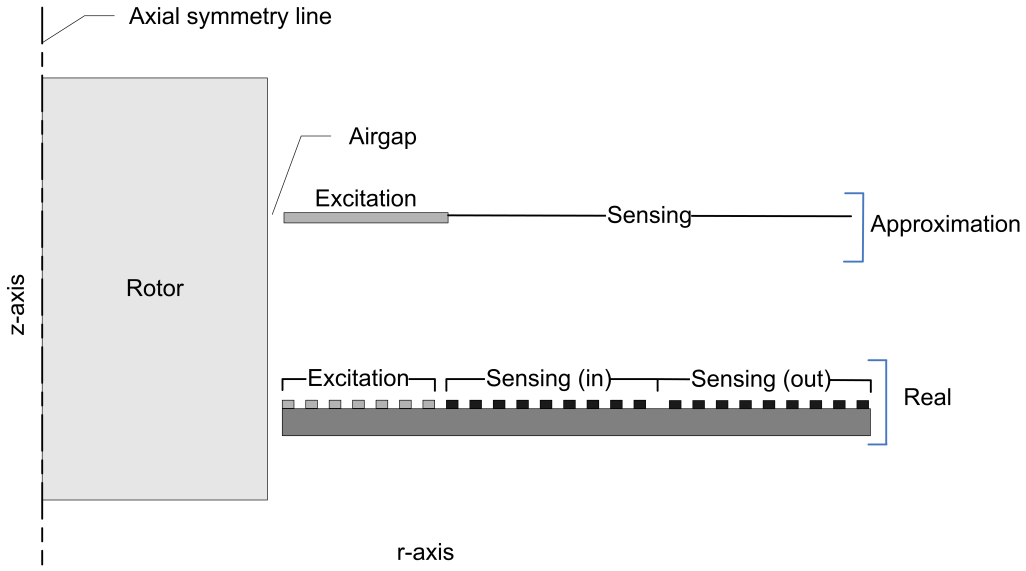

Figure 3.3: Model assumptions.

$$\begin{aligned}
\delta_{Al} &= \sqrt{\frac{2}{2\pi(2\times10^6)(\mu_0)(1)(3.7\times10^7)}} \\
&= 58.5\mu\text{m} \\
\delta_{Fe} &= \sqrt{\frac{2}{2\pi(2\times10^6)(\mu_0)(4000)(1.12\times10^7)}} \\
&= 1.681\mu\text{m} \\
\delta_{304Ss} &= \sqrt{\frac{2}{2\pi(2\times10^6)(\mu_0)(1)(1.388\times10^6)}} \\
&= 302\mu\text{m}
\end{aligned} \tag{3.3}$$

Define properties

The rotor is the sensor target and must be constructed from a conductive material for eddy currents to flow. The conductivity (σ) and permeability (μ) of the rectangle representing the rotor is assigned according to the rotor material used. It is assumed that these properties are uniform and constant throughout the rotor. Using high quality material as target will ensure this is a good assumption.

The excitation and sensing coils are realised with copper tracks on a PCB. The rectangle modelling of the excitation coil forms a ring around the rotor when rotating the geometry around the axial symmetrical line. This can clearly be seen in Figure 2.18. If this rectangle is given the properties of copper it simulates an electrically short-circuited ring, which is not the case. The rectangle is given the properties of air ($\sigma = 1,\ \mu_r = 1$). The excitation is done by this rectangle which is given a current density of half the current density expected in a winding. The current density is chosen half of that expected since the winding only occupies half of the rectangle. The limits of the solution area is set to magnetic insulation and the rest of the geometry has the properties of air.

Figure 3.4 shows the FEM implemented geometry of the PCB sensor. The rotor or target are represented by the two rectangles numbered 1 and 2. Rectangle number 5 is the excitation coil and the area numbered 3 is air. The line right of rectangle 5 constitutes the sensing coil. Comsol's mesh refined function is used in the rectangle formed by the two rectangles numbered 2 and 4.

Create the mesh

The next step is dividing the geometry into finite elements or "meshing" it. Comsol has automatic meshing and mesh refining capabilities. Irregularities in the initial results indicated that the mesh was not small enough around the excitation and sensing coils. A block was drawn around these parts and the mesh refined in it, solving the problem. The meshed geometry of the excitation coil is shown in Figure 3.6. On the left the target (rotor) rectangle is shown and to the right the refined mesh rectangle.

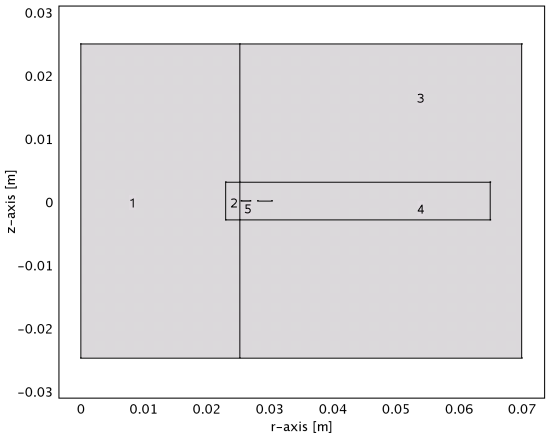

Figure 3.4: FEM geometry.

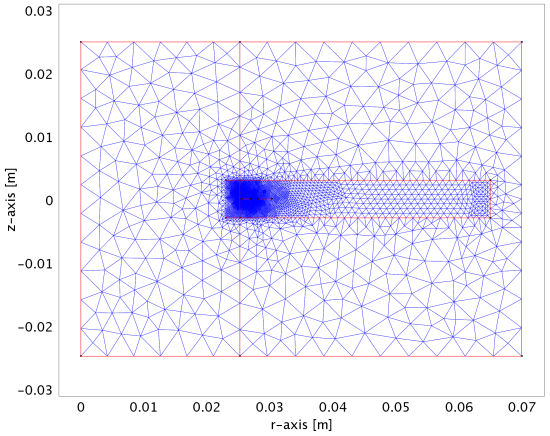

Figure 3.5: Mesh overview.

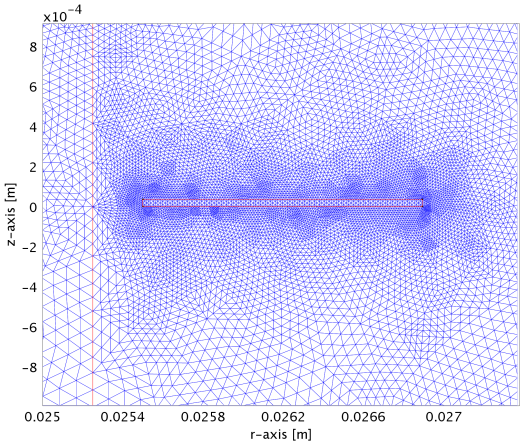

Figure 3.6: Closer view of excitation coil mesh.

Solve the model

Next the model is solved for a set of constants. The results are used to calculate the characteristics of the sensor and this is discussed in the following section. The magnetic field is shown in Figure 3.7

3.2.2 FEM result calculation

The voltage detected on the sensing coil is calculated using the FEM model. This is used to predict the sensor characteristics which in turn influences the optimal design flow diagram. This section presents the FEM results and points out useful trends.

First the total magnetic flux (Φ) flowing through a sensing winding is calculated using (3.4), with B the magnetic flux density and A the area. The voltage induced on the sensing coil is then calculated using Faraday's law shown in (3.5), were N is the number of turns in the coil and Δt is the period of the excitation current. This voltage changes with radial target position relative to a specific part of the sensor as discussed in section 2.2.3.

$$\Phi = \int \mathbf{B} d\mathbf{A} \tag{3.4}$$

$$e = N\frac{d\Phi}{dt} \simeq N\frac{\Delta\Phi}{\Delta t} \tag{3.5}$$

In the FEM model the airgap size is changed by changing the rotor dimensions. Increasing the rectangle diameter representing the rotor, will cause the airgap size to decrease and vice

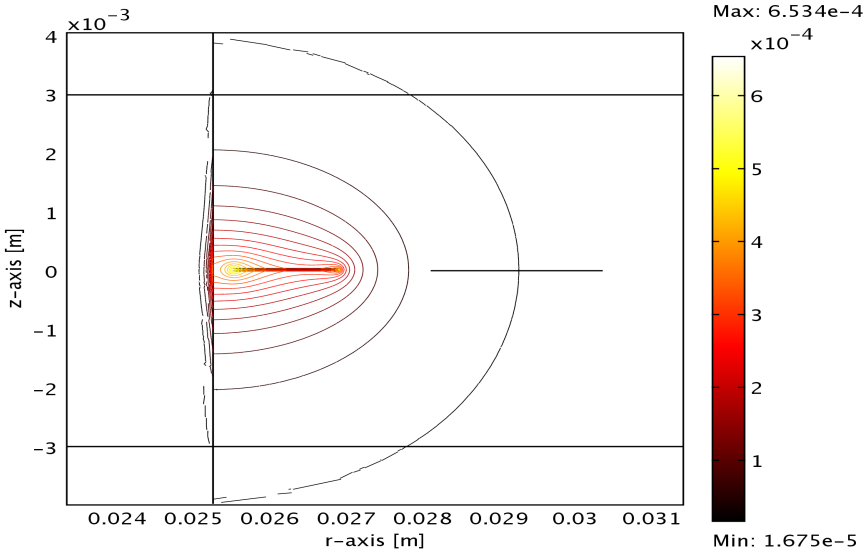

Figure 3.7: Magnetic field.

versa. This influences the eddy current path length, but since the sensor is mostly reliant on the magnetic field coupling, this is not assumed to have a large effect. The voltage calculated using the FEM model for different airgap sizes and materials is shown in Figure 3.8. Note that the target is in the centre of the sensor when the airgap is 0.5 mm. The airgap can change between 0.25 mm and 0.75 mm, resulting in a 0.5 mm movement range.

The different materials behave similarly. Target conductance (σ) influences the amount of eddy current flowing in the target. This in turn influences the sensing coil voltages. Larger eddy currents cause smaller sensing coil voltages and vice versa. Copper is the most conductive ($\sigma = 5.998 \times 10^7 \frac{\mathrm{S}}{\mathrm{m}}$) and results in the smallest voltage of the four targets as shown in Figure 3.8. Stainless steel (AISI 304) is the least conductive ($\sigma = 1.38 \times 10^6 \frac{\mathrm{S}}{\mathrm{m}}$) and thus has the largest voltage. Mild steel is the only material where the voltage vs. movement is not very linear. Only mild steel has strong ferromagnetic properties ($\mu_r = 4000$); all the other materials shown are non-magnetic ($\mu_r = 1$). This indicates that there could be a connection between linearity and the target's magnetic properties.

The sensor will be operated differentially, meaning physically opposing sensing coil voltages are subtracted to give an output. The sensing coils each occupy less than a quarter of the total area around the target. When the target moves closer to one sensing coil, it moves away from another. The sensor is symmetrical, thus when the target is (0.5 mm - x) from one sensing coil, it will be (0.5 mm + x) from the opposing sensing coil. The voltage data shown in Figure 3.8 are used to calculate differential sensor performance. It is assumed all the sensing coils have the same chatacteristic curve.

To illustrate differential measurement, assume the target is 0.35 mm (0.5 mm - 0.15 mm) from a sensing coil. A voltage of 0.1875 V is induced on this sensing coil if a copper target is used, according to Figure 3.8. In this situation the target is 0.65 mm (0.5 mm + 0.15 mm) from the

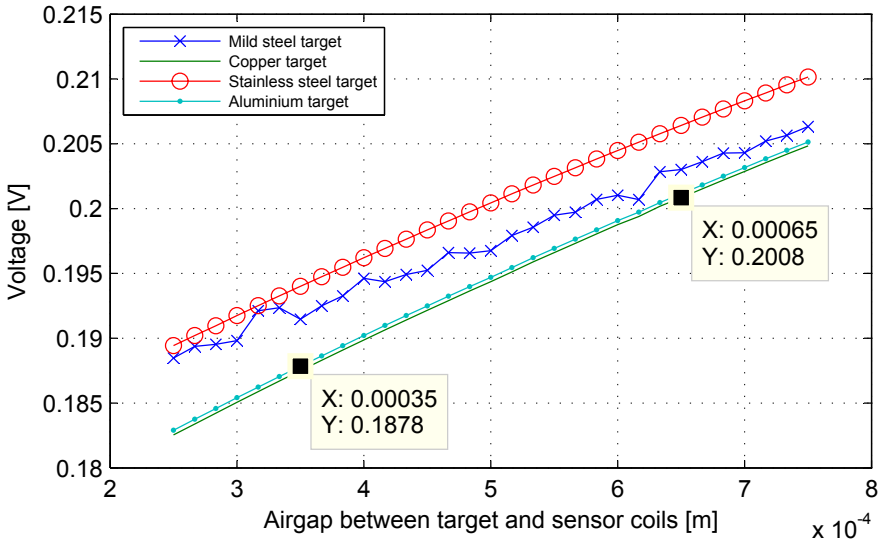

Figure 3.8: Sensing coil voltage for different airgap sizes and different target materials ($n_{exc} = 7$, $n_{sens} = 11$).

opposing sensing coil and 0.2008 V is induced. These voltages are subtracted and results in 0.0133 V. It is important to note that this differential voltage is centred around 0 V.

The differential voltage vs. movement plot data can be used to determine the linearity and sensitivity of the sensor for a specific sensor setup. A first order straight line fit is performed on the differential results, as seen in Figure 3.9. The gradient of this line is the sensitivity of the sensor. This can be determined using (3.6), were ΔV is the total change in voltage and Δx the total change in position. Linearity is expressed as a percentage of FSO and is determined using (3.7). In this equation V_{MT} and V_{MB} are the maximum deviation in voltage above and below the straight line fit, respectively. The largest and smallest airgap are represented with x_{MAX} and x_{MIN}, respectively.

$$S = \frac{\Delta V}{\Delta x} \tag{3.6}$$

$$\text{Linearity}(\%) = \frac{V_{MT} - V_{MB}}{x_{MAX} - x_{MIN}} \times 100 \tag{3.7}$$

The linearity and sensitivity are the main characteristics calculated in the FEM that will be used in optimal sensor design. This section discussed the process of determining it with the use of the FEM model. The next section discusses the trends found in these characteristics that are crucial for the optimal design flow diagram.

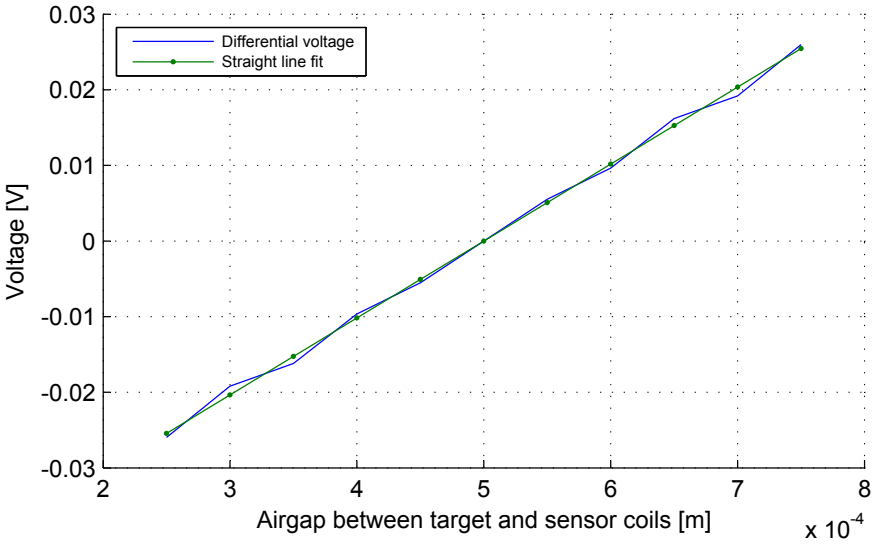

Figure 3.9: Differential voltage and its straight line fit for different airgap sizes ($n_{exc} = 7$, $n_{sens} = 11$).

3.2.3 FEM results

It is necessary to optimise the sensor characteristics such as linearity and sensitivity in order to design the best possible sensor. The number of sensing and excitation coil windings are two of the variables that must be chosen in order to achieve this goal. It is important to mention that all the results used in this section are based on differential measurements.

Sensitivity

Sensitivity of the sensor is very important as it has a direct influence on the complexity of the demodulation circuitry as well as the sensor's susceptibility to noise interference. When designing an optimal sensor, the goal is to design a sensor with the largest possible sensitivity.

Figure 3.10 shows the sensitivity for different combinations of excitation and sensing coil windings. It seems that increasing the number of sensing coil windings (n_{sens}) causes a larger sensitivity. When increasing the number of excitation coil windings (n_{exc}) there seems to be a definite turning point. These observations can be investigated more closely by keeping one of the variables constant and varying the other.

Figure 3.11 shows the sensitivity for 1, 5 and 10 windings on the excitation coil, with the number of sensing coil windings ranging between 1 and 15. It is clear that for all three cases an increase in n_{sens} causes an increase in sensitivity. The gradient of these lines increase with larger n_{exc} values. Further investigation into the gradient might give valuable insights.

The gradient of the sensitivity for $n_{exc} = 1, 5, 10$ and $n_{sens} = 1 \rightarrow 15$ is shown in Figure 3.12. A definite turning point can be seen on the $n_{exc} = 5$ graph where $n_{sens} = 5$. This means that using

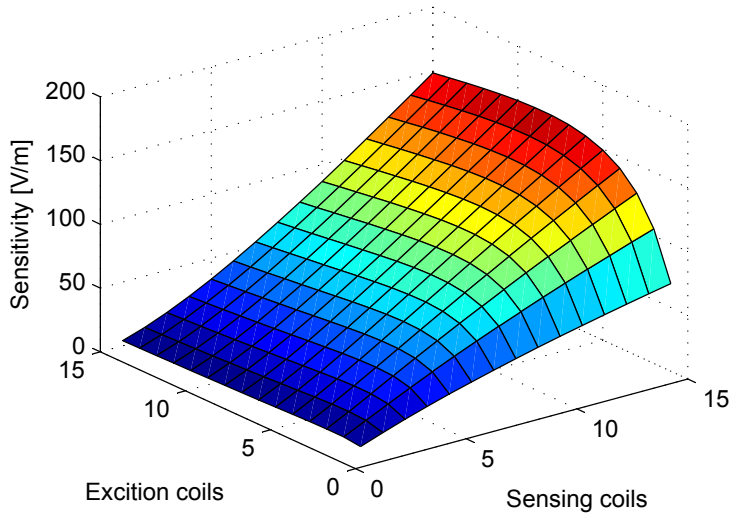

Figure 3.10: Sensitivity for excitation coil windings ($n_{exc} = 1 \rightarrow 15$) and sensing coil windings ($n_{sens} = 1 \rightarrow 15$).

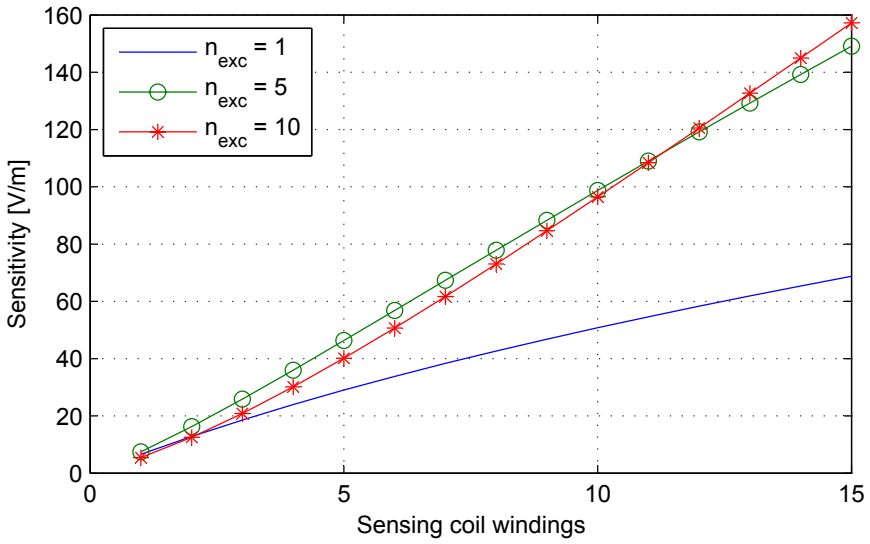

Figure 3.11: Sensitivity for excitation coil windings ($n_{exc} = 1, 5, 10$) and sensing coil windings ($n_{sens} = 1 \rightarrow 15$).

more than 5 sensing coil windings when $n_{exc} = 5$ will cause an increase in sensitivity since the gradient is still positive. The problem is that the rate the sensitivity increase is declining when using more sensing coil windings. To design an optimally sensitive sensor the number of sensing coil windings must equal this turning point. The same argument can also be followed for the other two graphs shown. When using one excitation coil winding the optimal will be at $n_{sens} = 1$ and when using ten excitation coil windings it will be at $n_{sens} = 15$.

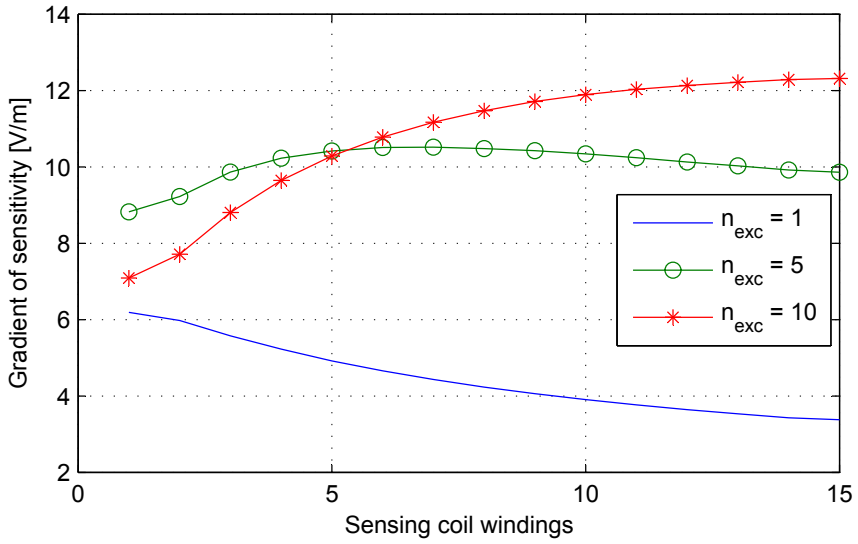

Figure 3.12: Gradient of sensitivity for excitation coil windings ($n_{exc} = 1, 5, 10$) and sensing coil windings ($n_{sens} = 1 \rightarrow 15$).

In Figure 3.13 the sensitivity is shown when the number of sensing coil windings are kept constant and the number of excitation coil windings are varied. A clear turning point can be seen in all the graphs. To design an optimal sensor the number of excitation coil windings must be chosen at this turning point.

This concludes the discussion on the trends found in sensitivity. The next section will look at the trends found in linearity.

Linearity

Linearity of a sensor is important as it directly influences the complexity of the sensor demodulation circuitry or software. A completely linear sensor transfer means that any change in sensor output is directly proportional to the movement of the target. In this section the sensor linearity is examined to find trends that can be used in sensor optimisation.

Figure 3.14 shows the linearity in percentage (% FSO) for different combinations of excitation coil windings ($n_{exc} = 15 \rightarrow 1$) and sensing coil windings ($n_{sens} = 15 \rightarrow 1$). It seems that increasing the number of either the sensing or excitation coil windings has a positive effect on the linearity of the sensor. When $n_{exc} \geq 5$ and $n_{sens} \geq 5$ the linearity is smaller than 0.5 % FSO, an acceptable linearity. Optimising the sensor linearity is thus not as complex as the sensor sensitivity.

This concludes the discussion of the FEM model results that will be used when compiling the design flow diagram. In the next section, the analytical formulas needed for an optimal flow diagram are presented.

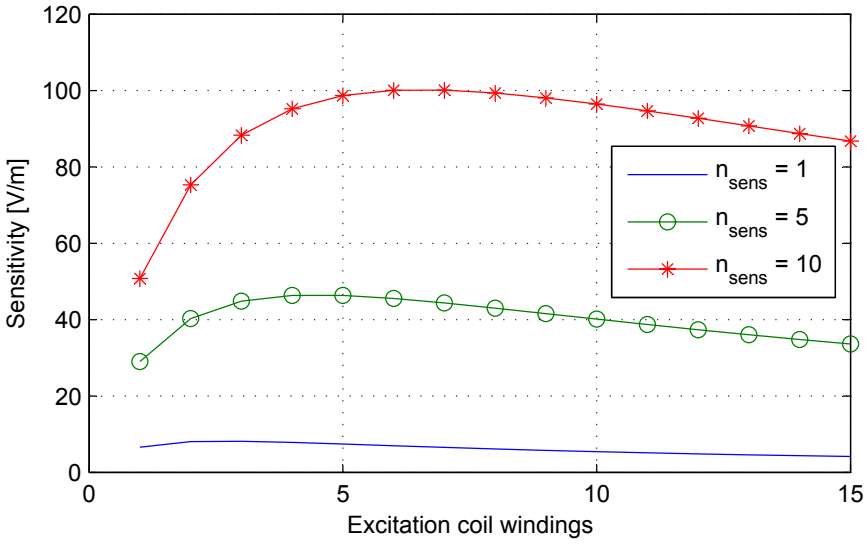

Figure 3.13: Sensitivity for excitation coil windings ($n_{exc} = 1 \rightarrow 15$) and sensing coil windings ($n_{sens} = 1, 5, 10$).

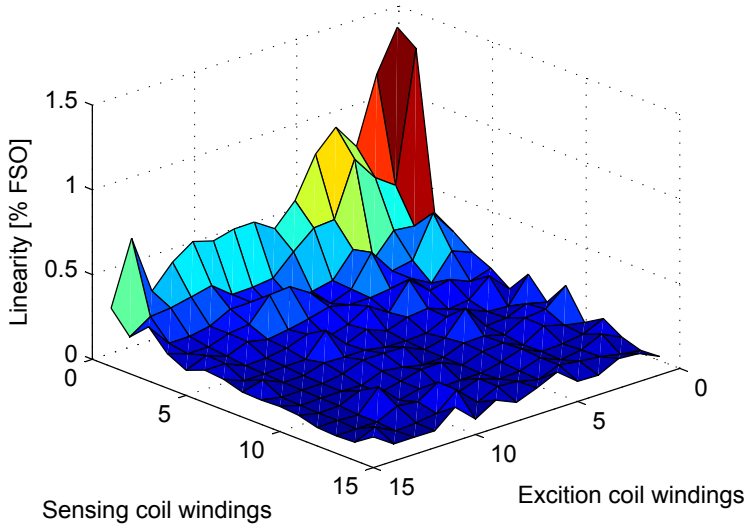

Figure 3.14: Linearity for excitation coil windings ($n_{exc} = 15 \rightarrow 1$) and sensing coil windings ($n_{sens} = 15 \rightarrow 1$).

3.3 Analytical formulas for design

3.3.1 Temperature rise in a current carrying PCB track

When current flows in a PCB track there will be copper losses caused by the track resistance. This loss component is proportional to the square of the current flowing in the track and is commonly known as the I^2R loss [30]. The power dissipated in the track causes its temperature to rise. The PCB and track can be damaged if the track temperature rises too much. The rise in temperature also influences the track resistance which influences the current flowing though the track. This in turn influence the induced sensing coil voltage and thus the whole sensor's operation. It is important to know what temperature rise a certain current will cause in a track when designing a PCB sensor.

The IPC-2221 standard can be used to calculate a conductor's temperature rise resulting from the current flowing in it [31]. This equation is shown in (3.8), where the track area (A) is equal to the product of the track width (w_t) and track height (h_t). The rms current (I_{rms}) , the temperature rise (T_{ri}) and constants ($b = 0.44$, $c = 0.725$, $k = 0.048$ when external tracks are used) are also used in this equation.

$$A = w_t \times h_t = \left(\frac{I_{rms}}{k \times T_{ri}^b}\right)^{\frac{1}{c}} \times (25.4 \times 10^{-6})^2 \tag{3.8}$$

This formula can be modified to make the temperature rise the subject of the equation as shown in (3.9). This form is more usefull in the design process.

$$T_r = \left[\frac{I_{rms}\times(25.4\times10^{-6})^{2c}}{A^c k}\right]^{\frac{1}{b}} \tag{3.9}$$

3.3.2 Inductance of PCB coils

The number of excitation coil windings influences the inductance of the excitation coil. This in turn influences the excitation circuitry. It is important to be able to analytically predict the inductance of the excitation coil when designing the sensor. This section introduces such analytical formulas that can be used to calculate the inductance of planar PCB coils.

There are two formulas presented in [32] that could be used to calculate the inductance of the excitation coil. The first equation is called the "Modified Wheeler Formula" (MW) which was derived by modifying the original Wheeler formula found in [33]. This equation is shown in (3.10), where n is the number of turns in the coil, μ_0 is the permeability of free space, d_{ave} is the average coil diameter, ρ is the fill ratio and K_1 = 2.25 and K_2 = 3.55 are constants when a octagonal coil is used.

$$L_{MW} = K_1\mu_0\frac{n^2 d_{avg}}{1+K_2\rho} \tag{3.10}$$

$$\begin{aligned}\rho &= \frac{d_{out}-d_{in}}{d_{out}+d_{in}}\\ d_{out} &= d_{in}+(w_t\times 2\times n)+(w_s\times 2\times n)\\ d_{ave} &= \frac{d_{out}+d_{in}}{2}\end{aligned}$$

The "Geometric Mean Distance Formula" (GMD) is based on assuming the sides of the spirals are made up of symmetrical current sheets which have the same current densities [34]. This equation is shown in (3.11), where c_1 = 1, c_2 = 2.46, c_3 = 0 and c_4 = 0.2, are constants when a octagonal coil is used. Some of the variables are illustrated in Figure 3.15, including the outer diameter (d_{out}) and inner diameter (d_{in}) of the coil.

$$L_{GMD} = \frac{\mu_0 n^2 d_{avg} c_1}{2}(\ln(c_2/\rho)+c_3\rho+c_4\rho^2) \tag{3.11}$$

This concludes the discussion of the analytical formulas that are needed for the sensor design. The next section presents the proposed design flow diagram for designing an optimal PCB displacement sensor.

3.4 Design flow diagram

The optimal design flow diagram summarises all the previous sections of this chapter and is shown in Figure 3.16. The analytical formulas are used to determine the optimal number of

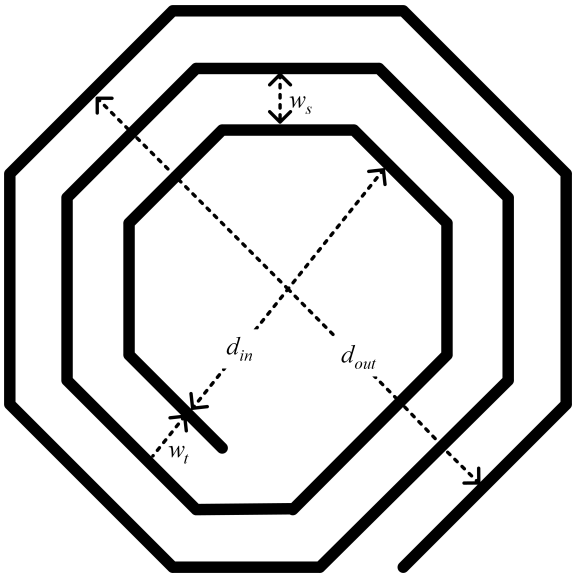

Figure 3.15: Octagonal coil [32].

excitation coil windings. Trends found by using the FEM model are used to choose the optimal number of sensing coil windings.

First the track dimensions (w_t, h_t) and rms current (I_{rms}) are used in (3.9) to determine the temperature rise caused by the specified current. This ensures the tracks are not damaged by overheating during normal operation. Next the maximum excitation coil inductance (L_{em}) the excitation circuitry can drive is determined. The excitation circuitry is designed to produce a specified rms voltage (V_{rms}) and rms current (I_{rms}) at the specified frequency (f). The goal is to have as many as possible excitation coil windings. Sensitivity and linearity are both factors that influence the number of excitation coil windings. The number of excitation coil windings (n_{exc}) can be determined from the maximum excitation coil inductance (L_{em}) by using (3.10) and (3.11). Other factors influencing these formulas are the track dimensions (w_t, h_t) and the axis diameter (w_{ax}).

All the input constants for the FEM model are now ready. These are; airgap (w_{ag}), frequency (f), track width (w_t), track height (h_t), tracks spacing (w_s), rms current (I_{rms}), axis width (w_{ax}), via diameter (d_{via}), sensing coil angle (ϕ), number of excitation coil windings (n_{exc}) and the target material. The FEM model is simulated for a range of sensing coil windings. Sensitivity and linearity are the main simulation outputs. First the sensitivity is optimised by choosing n_{sens} on the turning point of the sensitivity gradient as discussed earlier. Then the linearity for this combination of n_{sens} and n_{exc} is compared to the specified minimum linearity. If the linearity is not good enough the specifications must be changed. When the linearity is acceptable the optimal sensor design is complete.

This concludes the discussion of the design flow diagram for designing an optimal PCB displacement sensor. In the next section an optimal single-layer sensor is designed using this flow diagram.

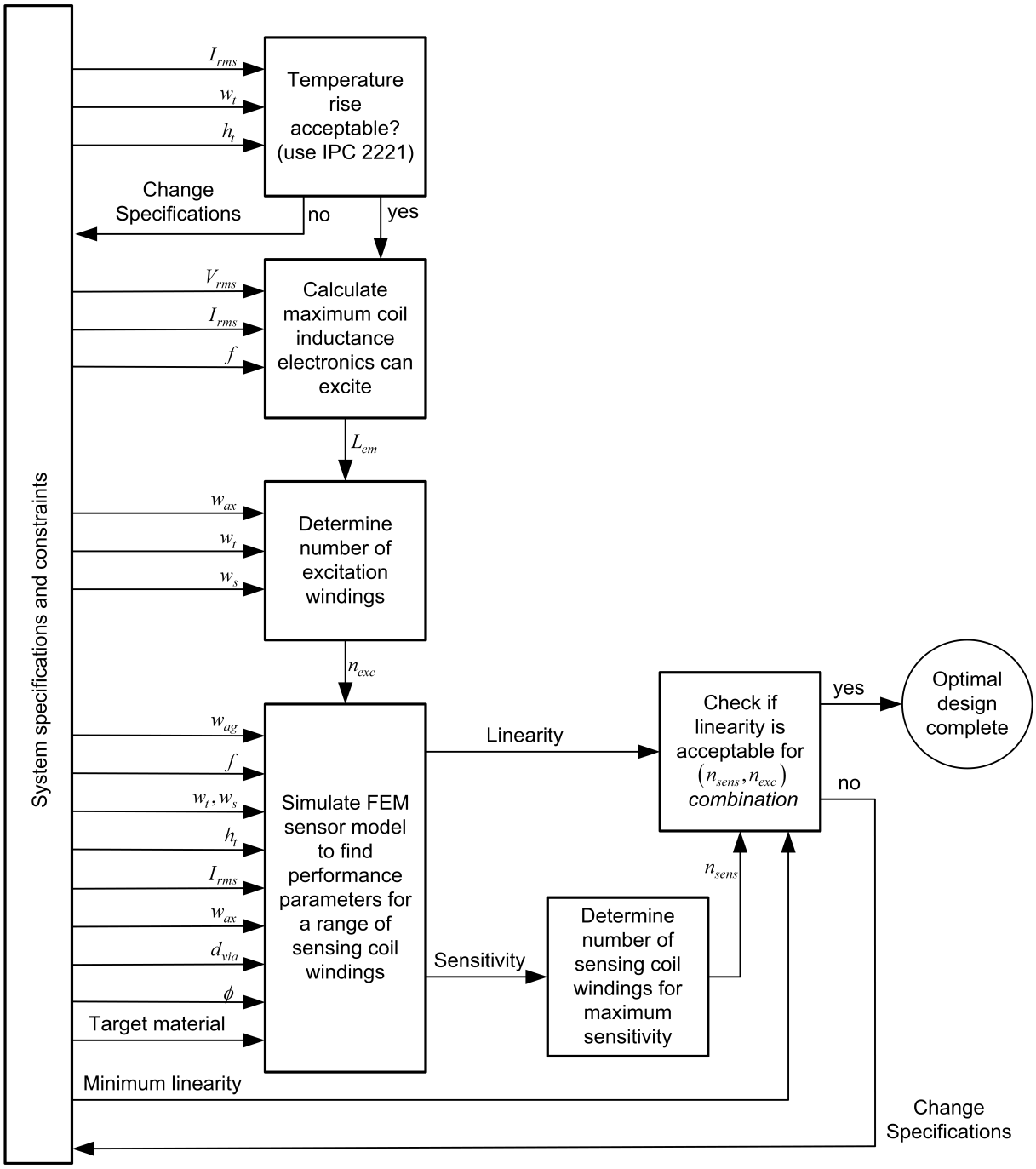

Figure 3.16: Optimal design flow diagram.

3.5 An optimal single-layer PCB sensor design

A technique can easily be understood when it is applied to an example. This section gives an example of the process that is followed to design an optimal PCB sensor.

The electrical and mechanical constraints for this specific case are given in Table 3.1. The electrical constraints are related to the current source electronics. The mechanical constraints are linked to PCB manufacturer' capabilities and the sensing target.

The first step is checking that the tracks will be able to handle the specified current (I_{rms}). Using (3.9), the temperature rise equals 0.1043 °C. This is a very small temperature rise, meaning excitation coil failure caused by overheating is not expected.

$$\begin{aligned} T_r &= \left[\frac{I_{rms}\times(25.4\times10^{-6})^{2c}}{A^c k}\right]^{\frac{1}{b}} \\ &= \left[\frac{0.1\times(25.4\times10^{-6})^{2\cdot0.725}}{(35\times10^{-6}\times200\times10^{-6})^{0.725}\times0.048}\right]^{\frac{1}{0.44}} \\ &= 0.1043\ ^\circ\text{C} \end{aligned}$$

Next the maximum impedance (Z_{exc}) of the excitation coil can be calculated using (3.12). In this equation R_{exc} is the resistance of the excitation coil and X_{exc} is the reactance of the excitation coil.

$$\begin{aligned} \tilde{Z}_{exc} &= R_{exc} + jX_{exc} \\ \left|\tilde{Z}_{exc}\right| &= \frac{V_{rms}}{I_{rms}} \\ &= \frac{10.6}{0.1} \\ &= 106\ \Omega \end{aligned} \tag{3.12}$$

Table 3.1: Electrical and mechanical constraints of a single-layer sensor

Electrical	Value	Unit
Maximum rms Voltage (V_{rms})	10.6	V
Maximum rms Current (I_{rms})	0.1	A
Operating Frequency (f)	2	MHz
Mechanical		
Track height (h_t)	35	µm
Sensor measuring range (w_{mr})	500	µm
Min track width (w_t)	200	µm
Min track spacing (w_s)	200	µm
Airgap (w_{ag})	250	µm
Via diameter (d_{via})	700	µm
Axis diameter (w_{ax})	50	mm
Sensing coil angle (ϕ)	50	degrees
Axis material	Aluminium	

The X_{exc} will be much larger than R_{exc} because of the very high excitation frequency ($f = 2\,\text{MHz}$). When assuming the reactance makes up 95% of the impedance ($X_{exc} = 100.7\,\Omega$), the maximum excitation coil inductance (L_{em}) can be calculated as shown in (3.13).

$$\begin{aligned} L_{em} &= \frac{X_{exc}}{2\pi f} \\ &= \frac{100.7}{2\pi(2\times10^6)} \\ &= 8.013\mu\text{H} \end{aligned} \tag{3.13}$$

The next step is calculating the number of excitation coil windings (n_{exc}) that result in an inductance smaller or equal to L_{em} using (3.10) and (3.11). The resulting inductances for 1 to 10 excitation coil windings are shown in Figure 3.17. It can be seen that using 7 excitation coil windings will result in an inductance smaller than the requirement as calculated in (3.13).

The resistance of the excitation coil can now be determined as shown in (3.14). This is a formula usually used to calculate dc resistance. In this case it is also valid since the skin depth for copper (δ_{cu}), calculated in (3.15), is bigger than the track thickness. This calculated resistance is about 2.57 % of the total impedance which shows that assumptions made for (3.13) were valid.

$$\begin{aligned} R_{exc} &= \frac{\rho_r l}{A} \\ &= \frac{\rho_r n \pi d_{ave}}{w_t h_t} \\ &= \frac{1.66\times10^{-8}(7)\pi(52.4\times10^{-3})}{(35\times10^{-6})(200\times10^{-6})} \\ &= 2.732\ \Omega \end{aligned} \tag{3.14}$$

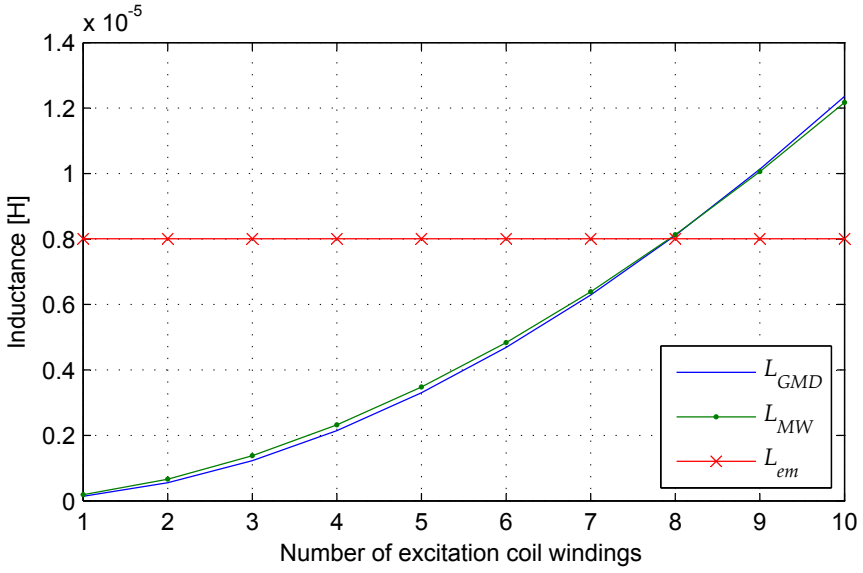

Figure 3.17: Excitation coil windings vs. Induction calculated with formulas.

$$\begin{aligned} \delta_{cu} &= \sqrt{\frac{2}{2\pi f \mu \sigma}} \\ &= \sqrt{\frac{2}{2\pi(2\times10^6)(\mu_0)(1)(5.998\times10^7)}} \\ &= 45.95\ \mu\text{m} \end{aligned} \tag{3.15}$$

The FEM simulation is used to determine the number of sensing coil windings necessary for an optimal sensitivity and linearity. To determine the number of sensing windings that results in a maximum sensitivity, the turning point of the gradient of the sensitivity must be found. In Figure 3.18 it can be seen that the turning point occurs at n_{sens} =11. This results in a sensitivity of 111.5 V/m as can be seen in Figure 3.19.

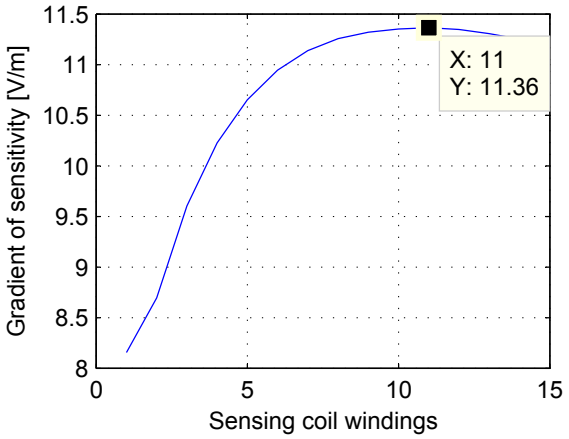

Figure 3.18: Gradient of sensitivity vs. sensing windings for a constant excitation coil windings ($n_{exc} = 7$) and sensing coil windings ($n_{sens} = 1 \rightarrow 15$)

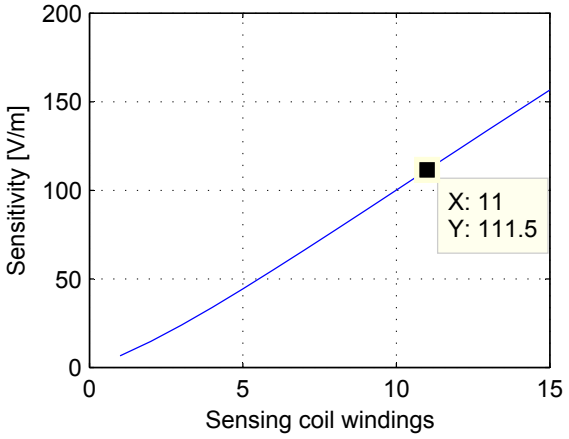

Figure 3.19: Sensitivity vs. sensing windings for a constant excitation coil ($n_{exc} = 7$) and sensing coil windings ($n_{sens} = 1 \rightarrow 15$)

According to the simulation, the linearity of the sensor will be 0.141 % FSO as can be seen on Figure 3.20. This is a very good linearity and is acceptable for the desired application. This

means that, for the environment and constraints specified at the beginning of this section, the optimal single-layer sensor is one with seven excitation coil windings and eleven sensing coil windings per sensing coil.

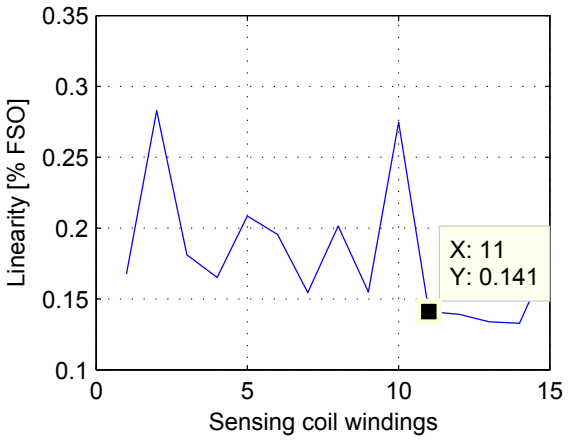

Figure 3.20: Linearity vs. sensing windings for a constant excitation winding ($n_{exc} = 5$) and sensing coil windings ($n_{sens} = 1 \rightarrow 15$)

3.6 Conclusion

This chapter set out to describe the tools needed to design an optimal PCB eddy current displacement sensor. It started by describing the process and application specific constraints. A FEM model for the sensor was compiled using these constraints. The FEM model was used to understand the relation between some of the variables and the performance parameters. Next some analytical formulas that can be used in the design process are presented. All this knowledge are then combined to compile an optimal sensor design flow diagram. It was opted to keep this flow diagram as simple and logical as possible. Lastly the flow diagram is applied in a specific scenario to further clarify its use.

Chapter 4

Design verification

In this chapter the sensor designed in the previous chapter is tested and the results compared with the FEM model results. The evaluation platform used to carry out the measurements is discussed in the first part of this chapter. In the second part of this chapter the sensor results are presented and discussed.

4.1 Evaluation platform

When designing the evaluation platform, the main goal is moving a round target relative to the PCB sensor. This movement must be measured with a reference sensor in order to calibrate the PCB sensor. The evaluation platform will be discussed in detail, starting with an overview of the system.

4.1.1 System overview

The main components of the evaluation system and the connections between these components are shown in Figure 4.1. There are different interfaces involved, including electrical, magnetic and mechanical. The electrical interface is established by a conducting wire or PCB track, the magnetic interface by magnetic fields through air and magnetic materials. Where physical contact is involved, the interface type is mechanical. The target's position is sensed by both types of sensors, Micro-Epsilon ($\mu\epsilon$) and PCB, via magnetic interfaces. The target is mechanically connected to the positioning bolts. Movement of the target, relative to the sensors, is established with these positioning bolts. The signal generator and excitation drive circuit establish the needed magnetic fields through the excitation coil. The voltages induced on the sensing coils are measured and stored using the detector. The calibration position sensors (Micro-Epsilon) also gives a voltage output which are measured and stored by the detector. The detector is a digital oscilloscope that can export the data for manipulation in a mathematical program such as MATLAB®.

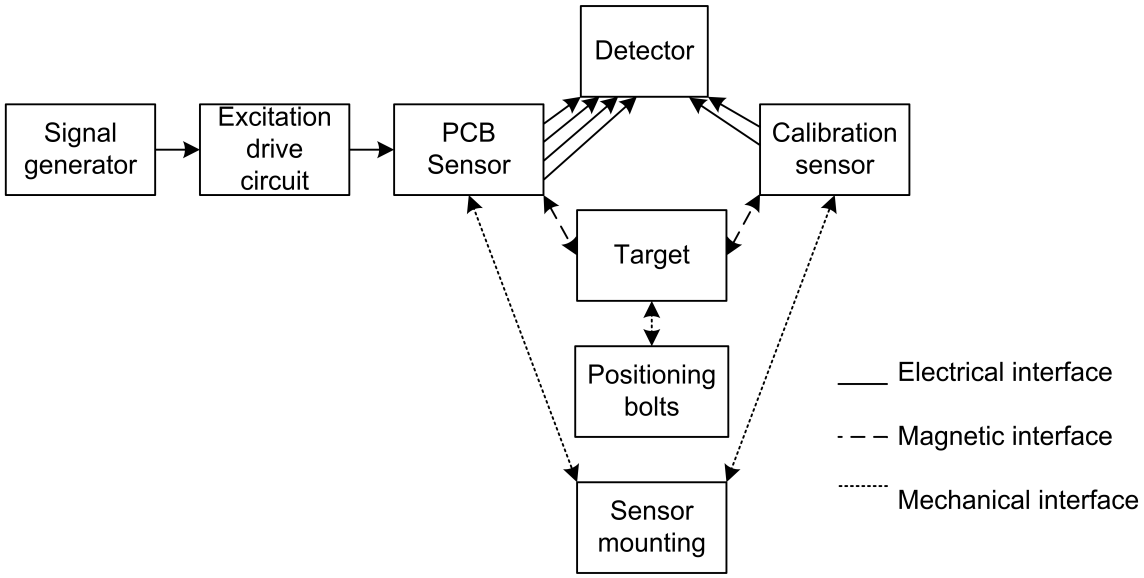

Figure 4.1: Evaluation platform system flow diagram.

The mechanically constructed parts of the evaluation platform are shown in Figure 4.2. The parts are; (1) Target, (2) Micro-Epsilon ($\mu\epsilon$) sensor mounting plate, (3) Positioning bolt container, (4) Leg, (5) PCB sensor mounting pillars and (6) Positioning bolt hole. The detail mechanical manufacturing sketches are included in Appendix B.

4.1.2 Sensor target

An example of the 50 mm diameter test target is shown in Figure 4.3. The target is manufactured from two solid round bars, pressed into each other. The $\mu\epsilon$ calibration sensor senses on the smaller diameter (2) bar. This part of the target is threaded on the tip (3) to keep the target form tilting when moving. The positioning bolts also acts on the (2) part of the target. Displacement is sensed by the PCB sensor on the larger diameter (1). The smaller diameter must be made from aluminium as the $\mu\epsilon$ calibration sensors are manufactured for sensing movement of aluminium targets.

The PCB sensor must be tested on different materials with various conductive (σ) and magnetic (μ) properties. The materials chosen as test targets are; aluminium, mild steel and stainless steel. Aluminium ($\sigma = 3.7 \times 10^7 \frac{\mathrm{S}}{\mathrm{m}}$, $\mu_r = 1$) is the target material used by $\mu\epsilon$ sensors and is a good electrical conductor. Mild steel ($\sigma = 1.12 \times 10^7 \frac{\mathrm{S}}{\mathrm{m}}$, $\mu_r = 4000$) is a inexpensive ferromagnetic material that is widely used. The mechanical properties exhibited by stainless steel (AISI 304, $\sigma = 1.38 \times 10^6 \frac{\mathrm{S}}{\mathrm{m}}$, $\mu_r = 1.008$) makes it well suited for use in the manufacturing of high speed rotors. Three test targets are manufactured from the above mentioned materials. For all of these test targets the $\mu\epsilon$ sensing part are manufactured from the same aluminium.

The penetration depth of the sensor, calculated using (3.2), is very small. This makes it possible to place a ring of a certain material over the target. A good sensing material with poor mechanical properties can thus be used in conjunction with a material with good mechanical

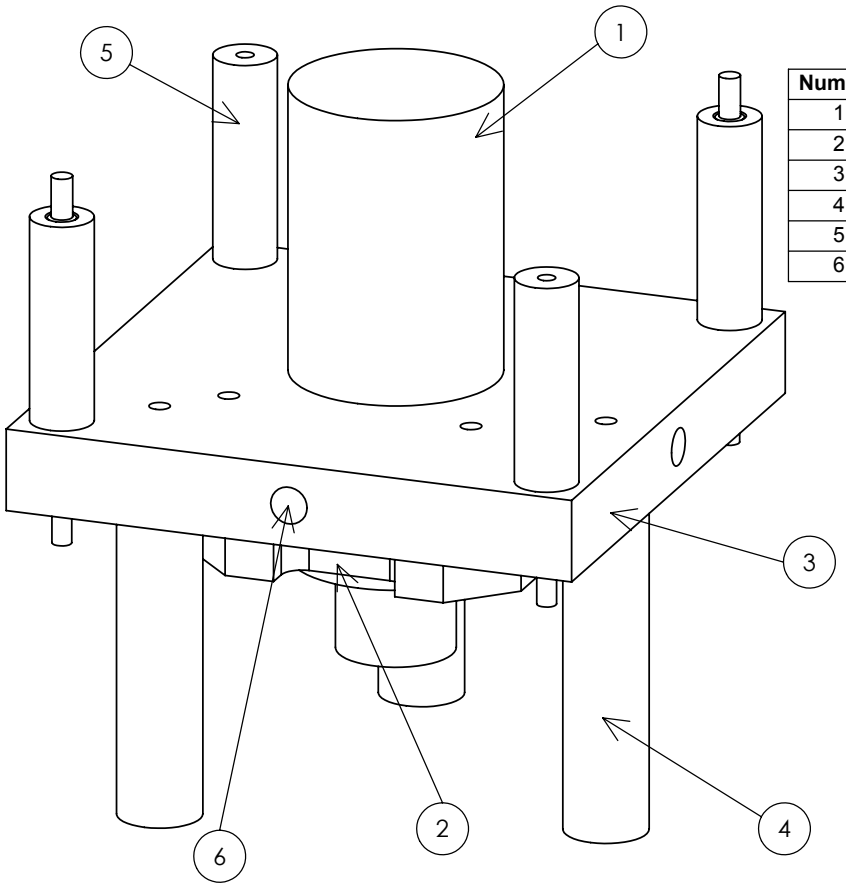

Number	Description
1	Target
2	Micro Epsilon mount
3	Positioning bolt mount
4	Leg
5	PCB mount pillar
6	Positioning bolt hole

Figure 4.2: Evaluation platform overview.

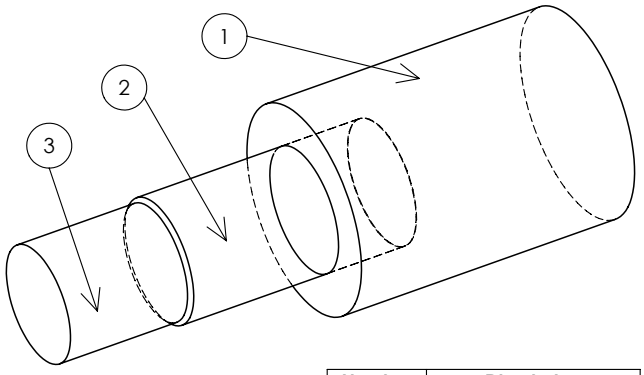

Number	Discription
1	PCB target
2	Micro Epsilon taret
3	Threaded tip

Figure 4.3: Target for evaluation platform.

properties. This could be used in high speed rotor designs were good mechanical properties are necessary.

The four position bolts, placed 90 ° apart, are used to move the target. The target is kept tangent to the sensors using a nut screwed onto the threaded end of it.

4.1.3 Sensors

The PCB and $\mu\epsilon$ sensors must be securely mounted on the evaluation platform. The PCB sensor is mounted on four pillars; two having 5 mm guiding pins and the other two, M5 threaded holes. Two bolts are screwed into these holes to keep the PCB sensor securely in place. The $\mu\epsilon$ sensor probe has an M5 threaded casing and can thus easily be mounted in threaded holes. It is used to sense on the smaller diameter part of the target. A locknut is used to keep the $\mu\epsilon$ sensor in place.

The eddyNCDT 3701 sensor manufactured by $\mu\epsilon$ is chosen as calibration sensor. It is designed for use in AMBs, which is also the intended application of the PCB sensor. This sensor has exceptional resolution ($<$ 0.00016 % FSO), repeatability ($<$ 0.001 % FSO) and sensitivity (10 $\frac{\text{V}}{\text{mm}}$). Its linearity ($\pm$ 6 % FSO) is not desirable but is negligible when calibration of the sensor is done. This sensor has a 1 mm measuring range and 0.1 mm start of measuring range (SMR) [17].

The $\mu\epsilon$ sensor must be calibrated since the target is round and the sensor has a non-linear calibration curve. The sensor was calibrated using a milling machine, capable of measuring in 5 µm increments. The sensors output voltages are recorded as the target is moved in 20 µm steps. The results are shown in Figure 4.4. The linearity of the two sensors are 17.5% (sensor A) and 21.8% (sensor B) respectively. This means these sensors are more non-linear when measuring on a round target than the 6% stated in the instruction manual and datasheet. These results will be used when calibrating the PCB sensor.

4.1.4 Drive circuit

The drive circuit must excite the excitation coil of the PCB with an alternating current of a constant rms level. The block diagram of the drive circuitry is shown in Figure 4.5. Note that a signal generator is used as oscillator to extend testing capabilities. The oscillator will form part of the drive circuit in the final product. The oscillator supplies a sinusoidal voltage at the operating frequency (2 MHz) for the voltage-to-current (V/I) control circuit. A reference input for the power stage is generated by this circuit, according to the input from the oscillator and the output of the power stage. A resistor is used to measure the current flowing to the PCB sensor. The main parts of the drive circuit will be discussed in this section.

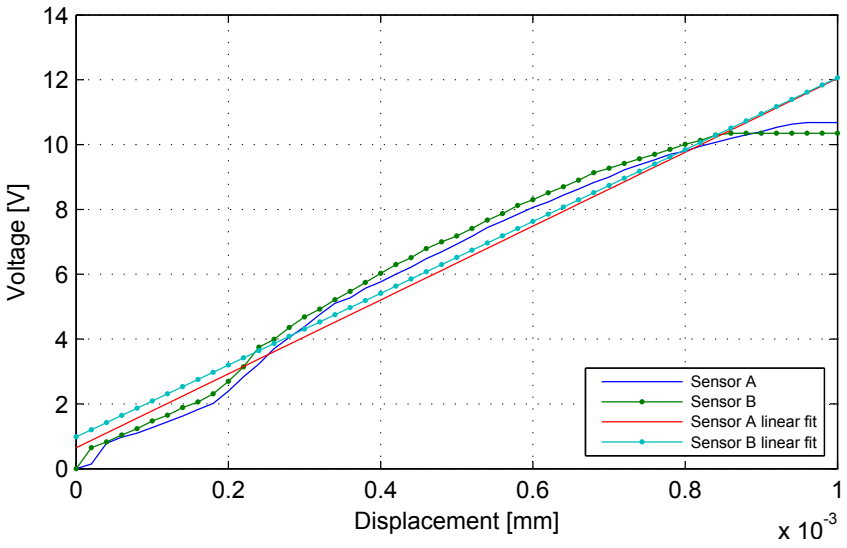

Figure 4.4: Calibration curves of $\mu\epsilon$ sensors.

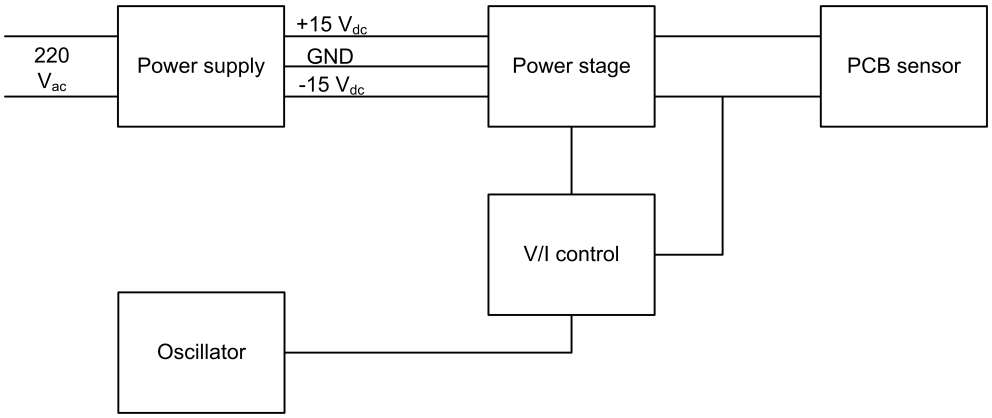

Figure 4.5: Drive circuit block diagram.

Power supply

The power supply (PSU) converts 220 V_{ac} to $\pm$ 15 V_{dc}, used to power the rest of the circuitry. First the 220 V_{ac} is transformed to two 12 V_{ac} signals using a centre tap transformer (T1). This alternating output is then rectified using a full wave rectifier (U13). Electrolytic capacitors (C28, C29) filter the voltage ripple present on the rectified voltage. Positive (U10) and negative (U12) voltage regulators ensure the output voltage stays stable at $\pm$ 15 V_{dc}. Tantalum (C18, C19) and ceramic (C2, C3) capacitors reduces supply fluctuations. A schematic representation of the PSU is shown in Figure 4.6.

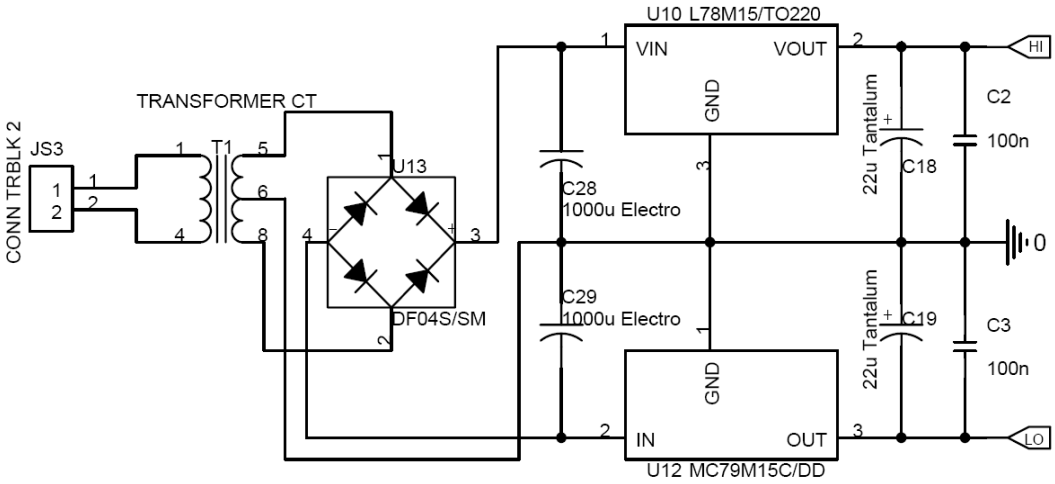

Figure 4.6: Power supply.

Power stage

Supplying the necessary power to the excitation coil at the needed frequency could load operational amplifiers (op amps) beyond its capabilities. A power stage is used to prevent this and consists of two transistors connected in a totem pole arrangement [35]. A NPN transistor (Q13) is connected to the positive supply (HI) with its collector. A PNP transistor (Q14) is connected to the negative supply (LO) via its collector. The control signal is connected to the transistors' bases and the output to the emitters. As in the PSU, tantalum (C20, C30, C21, C31) and ceramic (C13, C12) capacitors are used to ensure a stable voltage supply. This also decouples the power stage from the rest of the circuit, reducing the noise caused by a fluctuating supply. A schematic representation of the power stage is shown in Figure 4.7.

V/I control

The PCB sensor drive circuit must drive the excitation coil at a constant rms current. This can be accomplished using a voltage-to-current converter as described in [36] and shown in Figure 4.8. Note that the power stage is inserted between pin 6 of U5 and the left side of R5. Pins 4 and 5 of P1 are connected to the excitation coil. JS 2 is connected to the oscillator. Buffering the output voltage (V_{OUT}) using U8 ensures that the output is not loaded extensively by the feedback loop. Opamp U4 is configured in an inverting summing circuit, used to determine the difference between V_{IN} and V_{OUT}. An inverting opamp circuit is implemented using U5. The current flowing through the excitation coil is given in (4.1). Note the current flowing through the excitation coil (I_{OUT}) is proportional to the voltage form the oscilator (V_{IN}).

This concludes the discussion of the drive circuit components. The complete circuit diagram and circuit layout are included in Appendix C. The next paragraph presents some simulation results.

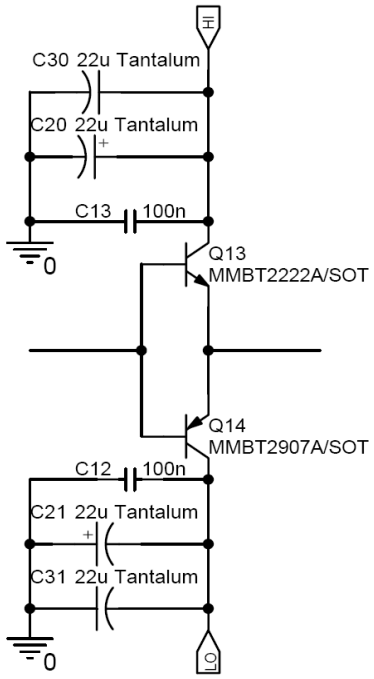

Figure 4.7: Power stage.

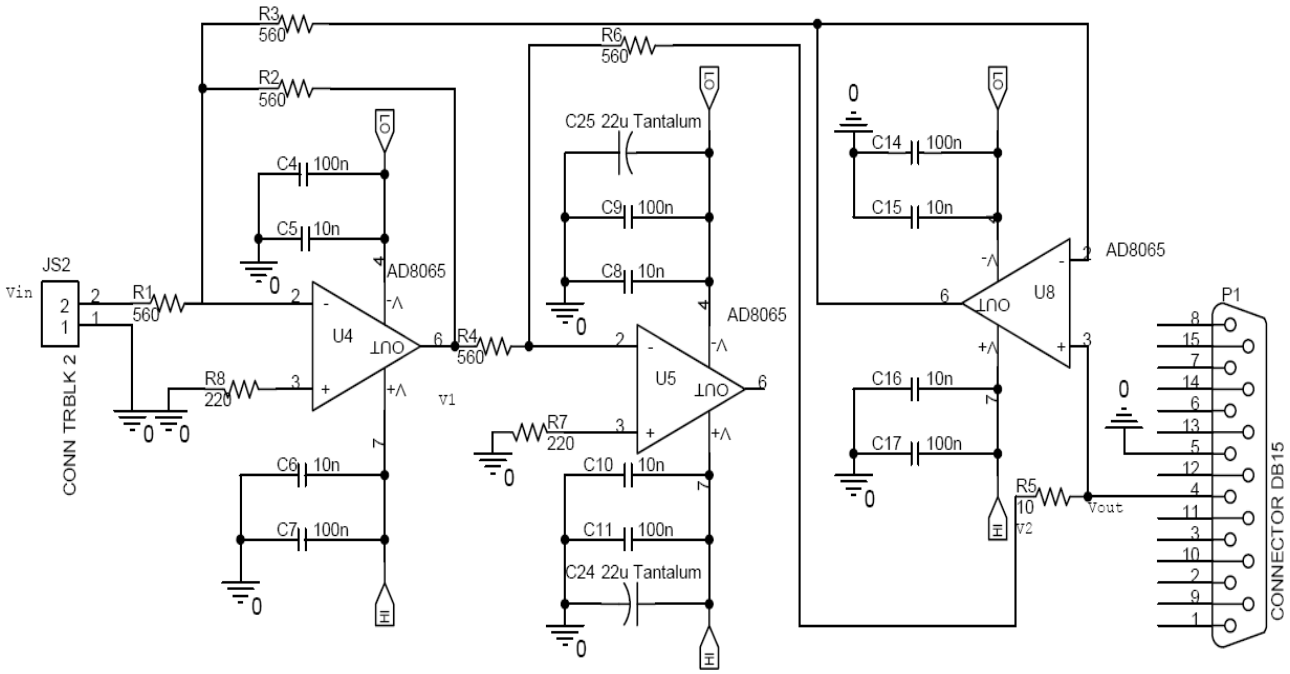

Figure 4.8: Control circuit.

$$\begin{aligned} I_{OUT} &= \frac{V_2 - V_{OUT}}{R5} \\ &= \frac{-(-V_{IN} - V_{OUT}) - V_{OUT}}{R5} \\ &= \frac{V_{IN}}{R5} \end{aligned} \tag{4.1}$$

Orcad® simulation results

The drive circuit is simulated as a complete system using Orcad®. The simulations are done using the sensor designed in the last part of the the previous chapter. The excitation coil inductance and resistance are chosen as 8 μH and 2.7 Ω respectively.

First the input voltage, supplied by the oscillator, and the output current, delivered to the excitation coil, are plotted as shown in Figure 4.9. The rms current is also shown and is close to 0.1 A as desired. A large phase shift is caused by the large inductive component of the excitation coil, as discussed in section 3.5.

The input and output voltages are shown in Figure 4.10. The input voltage is 0.707 V_{rms} and the output voltage is 9.5 V_{rms}. A prominent voltage ripple can be seen on the peaks of the output voltage. This is caused by transistor switching since the transistors are not biased. The ripple occurs each time the current flow direction changes - causing one of the transistors to stop conducting and the other one to start conducting.

From these results it seems that the circuit will be able to drive the excitation coil of the PCB sensor designed in the previous chapter.

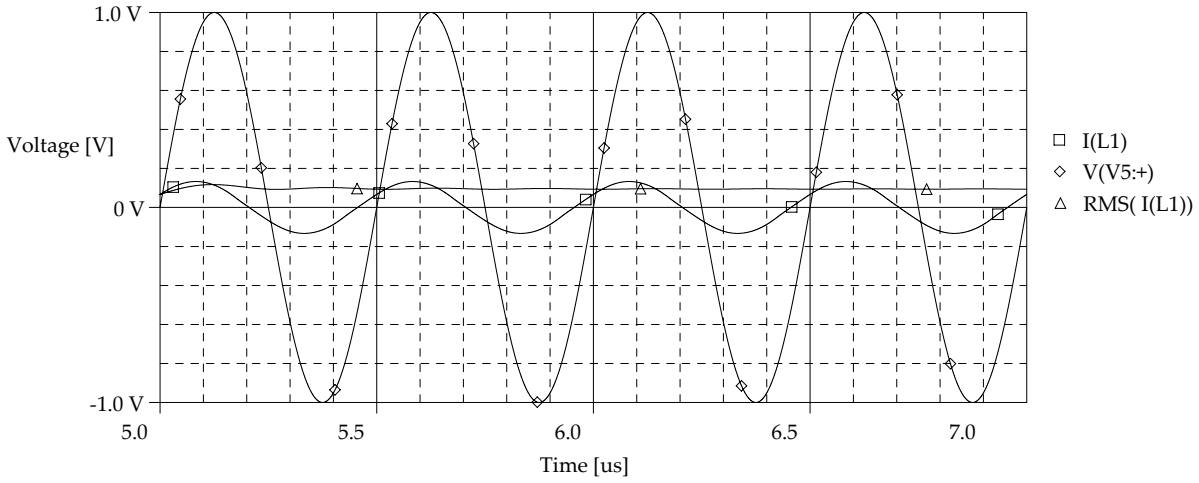

Figure 4.9: Input voltage and output current vs. time.

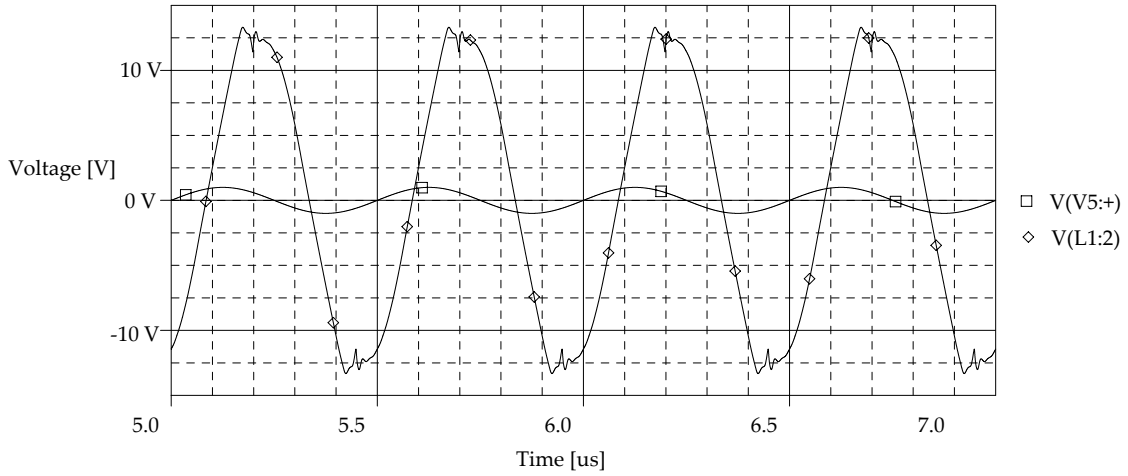

Figure 4.10: Input and output voltage.

4.2 Single-layer PCB sensor calibration

The sensor designed in chapter 3 is tested using the evaluation platform described in the first part of this chapter and the results are documented in this section. Simulation results are compared to measured results and the discreptancies analysed. Excitation and sensing coil properties, as well as sensitivity and linearity are presented.

In Figure 4.11, a top view of the sensor designed in chapter 3 is shown. The sensor has 7 excitation coil windings and 11 sensing coil windings per sensing coil. Coil tracks are only placed on the top layer and this sensor is thus defined as a single-layer PCB sensor. In this sensor the bottom layer of the PCB is used to provide return paths for the currents flowing in the coils. Later in this document sensors with tracks on multiple layers are analysed. Note that the sensing coils are numbered in a clockwise manner, starting with sensing coil 1 at the top of the photo. This numbering convention will be used in the rest of the document.

The $\mu\epsilon$ sensors that are used to determine target movement are mounted in line with the sensing coils. The sensor mounted in line with sensing coil 1 and 3 is called $\mu\epsilon$ A and the one mounted in line with sensing coil 2 and 4 is called $\mu\epsilon$ B. The next section will discuss the technique used to measure and interpret the voltage induced on the sensing coils.

4.2.1 Sensing coil induced voltage: measurement and demodulation

Designing demodulation circuitry or software for the induced sensing coil voltages is not part of this project's scope. These voltages are recorded in order to compare the simulation and practical results. Sensing coil voltages were captured using a LeCroy® WaveRunner® 6030A digital oscilloscope and demodulated using MATLAB®.

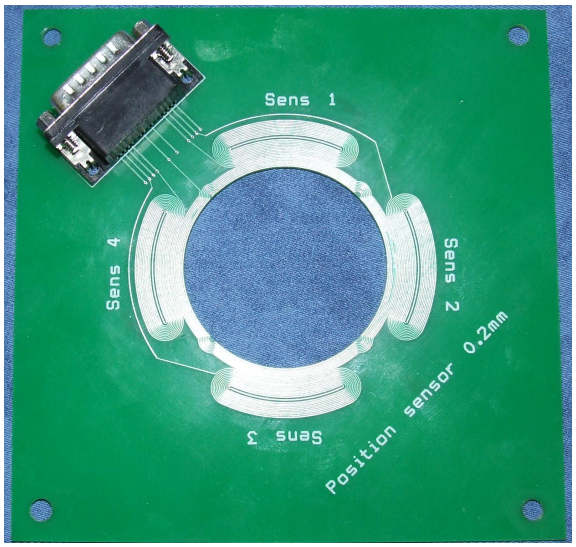

Figure 4.11: Single-layer sensor top view.

Figure 4.12 shows 2500 points, or 1 µs of the raw data captured using the oscilloscope. The induced signal has the same high frequency oscillation on the peaks as the simulated excitation coil voltage shown in Figure 4.10. Unlike the simulation other noise components also influence the signal. Other high frequencies not caused by transistor switching can be seen in the waveform. The data is sampled at 2.5 GHz, thus there are 25 000 data points when 10 µs of data is captured.

The excitation frequency is 2 MHz and thus only the 2 MHz component of the induced sensing coil voltage must be extracted from the signal shown above. This is done by performing a fast fourier transform (FFT) on the data using MATLAB®. The MATLAB® code used to perform

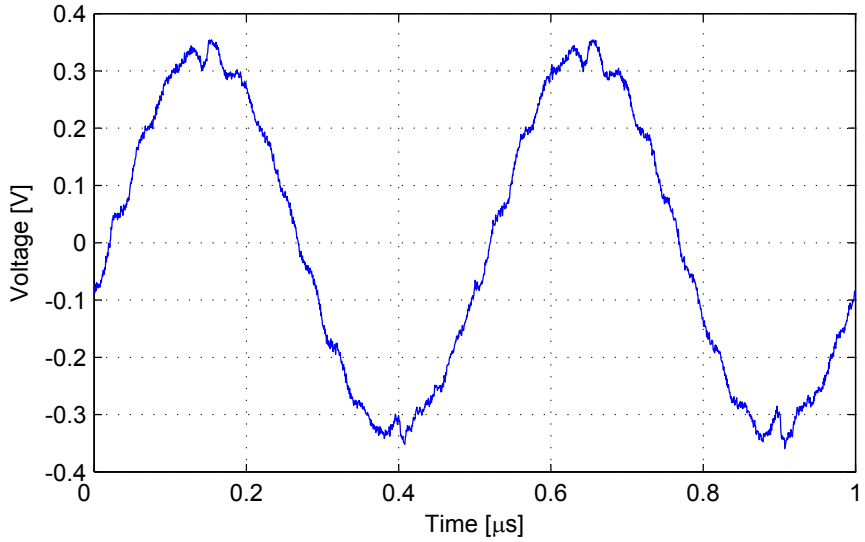

Figure 4.12: Measured induced sensing coil voltage before demodulation.

this transform is included on the data DVD found in section D.5. The absolute value of the FFT near the excitation frequency is shown in Figure 4.13. The peak value of the signal at 2 MHz is 0.335 V. Voltages demodulated using this method will be used in the rest of this chapter.

The demodulation process used on the measured data was discussed in this section. In the next section the resistance and inductance of the sensor coils are characterised and compared to predicted values.

4.2.2 PCB coil characterisation

One of the first steps when designing the PCB sensor is to design the excitation coil. In this section, the resistance and inductance of the manufactured, single-layer sensor's coils are measured.

Excitation coil and sensing coils' inductance and resistance are measured with a Grundig digimess® RLC 300 at 10 kHz. All the coils are measured at least three times and the averaged results are summarised in Table 4.1. It is clear that the excitation coil inductance is greatly influenced by the presence of the aluminium target. The excitation coil inductance changes 43% when the target is inserted. Sensing coil inductance is also smaller with the target but this is less than 5%. A less than 10% change in resistance is found for all of the coils.

Inductance and resistance can also be calculated using the voltage and current waveforms. This can be done by representing the voltage and current as phasors and applying (4.2). Voltage, current and impedance phasors are represented by $\tilde{V}$, $\tilde{I}$ and $\tilde{Z}$ respectively. The phase angle between voltage and current is θ. R_{exc} and L_{exc} are the resistance and inductance of the excitation coil respectively. The reactance is represented by X_L and the excitation frequency by f.

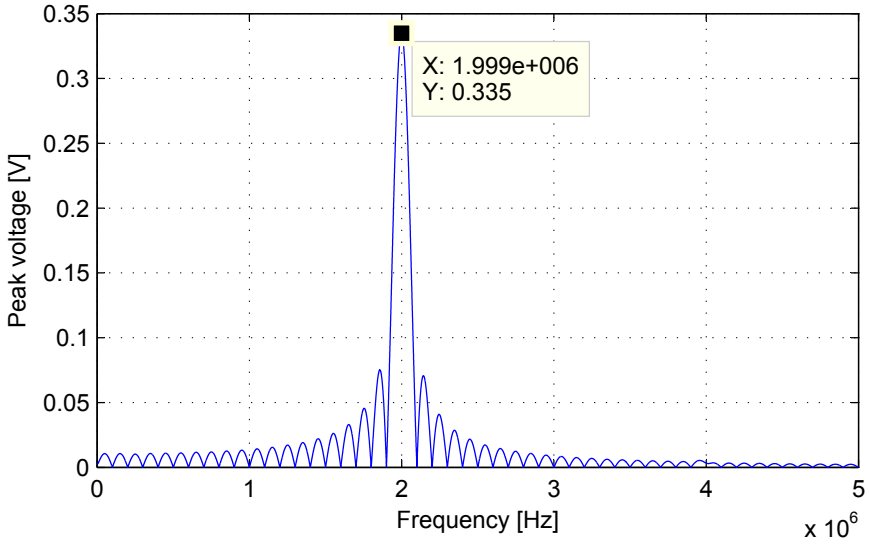

Figure 4.13: Frequency plot.

Table 4.1: RLC measurements

Coil	L with target [µH]	L without target [µH]	R with target [Ω]	R without target [Ω]
Excitation	3.716	6.553	4.317	4.365
Sensing 1	2.775	2.813	2.814	3.105
Sensing 2	2.856	2.879	2.965	3.042
Sensing 3	2.775	2.875	2.973	3.044
Sensing 4	2.844	2.811	3.011	3.045

$$\begin{aligned} \tilde{Z} &= \frac{\tilde{V}}{\tilde{I}} = \frac{V\angle 0}{I\angle\theta} \\ &= R_{exc} + jX_L \\ L_{exc} &= \frac{X_L}{2\pi f L_{exc}} \end{aligned} \tag{4.2}$$

Figure 4.14 show the results of applying (4.2) for an excitation frequency between 0.5 - 2.5 MHz. The excitation coil inductance is shown on the left and resistance on the right. It is clear that the inductance is halved when placing the target in the sensor. Resistance of the excitation coil is not influenced as much by the presence of the target. Changes in excitation coil resistance at high frequencies without the target can be attributed to excitation circuitry limitations. The excitation coil impedance is too big and the circuitry cannot deliver the rated excitation voltage and current, causing false readings.

When considering Figure 4.14 it is clear that the formulas (Modified Wheeler and Geometric Mean Distance) used in the previous chapter are for planar coils with air cores. These formulas do not take into account the target's effect on excitation coil inductance. This results in the sensor not being optimal as more excitation coils could have been used. In further designs this must be taken into account.

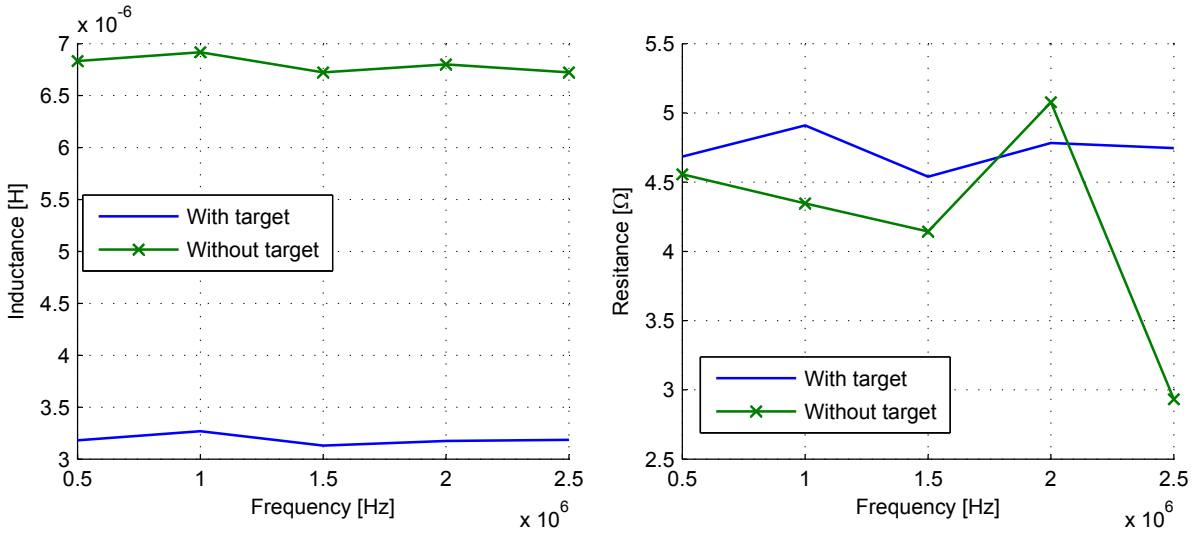

Figure 4.14: Excitation coil inductance and resistance vs. frequency calculated using waveforms.

4.2.3 Induced sensing coil voltages

In the previous section static sensor coil characteristics were discussed. Target movement dependent characteristics are presented in this section. First the voltages detected on the sensing coils are shown and then differential measurements are discussed.

The induced voltages measured on the sensing coils must be compared to voltages predicted using the FEM model. The demodulation method, implemented in MATLAB®, was discussed earlier. There are factors that must be taken into account when performing the measurements and interpreting the results. These factors include differences in voltages measured using different probes, oscillator drift and differences in sensing coils. Refer to Appendix A for detail discussion of the measuring irregularities.

To minimise these factors, all the results shown in this section are based on statistical mean values. For each target position, the voltage waveform is captured ten times in 5 second intervals. The medians of the data are used when representing induced sensing coil voltages for a changing airgap. Illustrated in Figure 4.15 are the boxplots for different target positions. The figure shows the medians connected with a line. Note that these results are not differential.

As stated earlier, sensing coils 1 and 3 are in line with the $\mu\epsilon$ A sensor and sensing coils 2 and 4 are in line with the $\mu\epsilon$ B sensor. Movement in the $\mu\epsilon$ A sensor direction thus causes a change in the induced voltage measured on sensing coils 1 and 3. In this scenario the voltage induced on sensing coils 2 and 4 remain constant since the target is not moving in relation to these coils. Following the same reasoning, it is also true that movement in $\mu\epsilon$ B direction causes a change in induced voltage in sensing coils 2 and 4 but not in sensing coils 1 and 3.

A median plot for movement in both the $\mu\epsilon$ A and B directions is shown in Figure 4.16. The

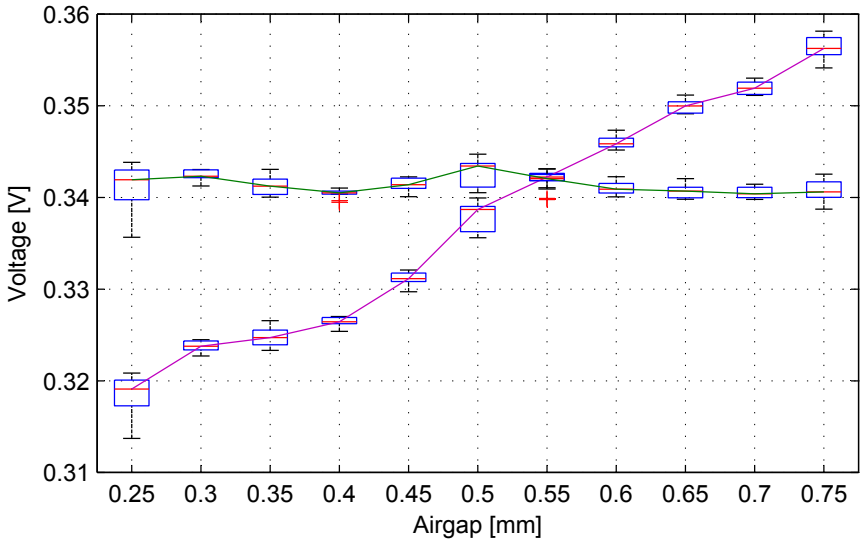

Figure 4.15: Boxplot of sensing coils (1,2) induced voltage vs. airgap for movement in $\mu\epsilon$ A direction

results for opposing sensing coils are inversely proportional. An increase in sensing coil 1 voltage coincides with a decrease in sensing coil 3 voltage and vice versa. In this situation the target is not moving relative to sensing coils 2 and 4, thus the voltage stays constant as shown in Figure 4.17.

Good correlation between the measured and simulated results are observed in both Figure 4.16 and Figure 4.17. The maximum offset error of about 6 % can be attributed to the factors such as sensing coil differences, discussed in Appendix A. The measured results are much more non-linear than the simulated results. Note that the non-linearity of the $\mu\epsilon$ sensors were incorporated in these figures. The linearity is influenced by the moving technique. It is very difficult to move the target to a position, within a few micrometres, by turning a bolt. A more accurate actuator would greatly increase the evaluation platform's cost, but would give more linear results.

The developed PCB sensor will be used in differential mode, meaning opposing sensing coil outputs are subtracted. The calibration curve of the PCB sensor will be based on the differential results, shown in Figure 4.18. The opposing sensing coil pares (1 and 3, 2 and 4) are subtracted from each other when the sensor is operated differentially. Figure 4.18 summarises the results of Figures 4.16 and 4.17 for movement in the $\mu\epsilon$ A and B directions.

4.2.4 Comparing different target materials

The effect using different target materials has on the induced sensing coil voltages is explained in this section. The induced voltages measured using the single-layer PCB sensor, and predicted using the FEM model are shown in Figure 4.19. Excellent correlation between the predicted and measured results for the aluminium (Al) and stainless steel (Ss) targets are observed.

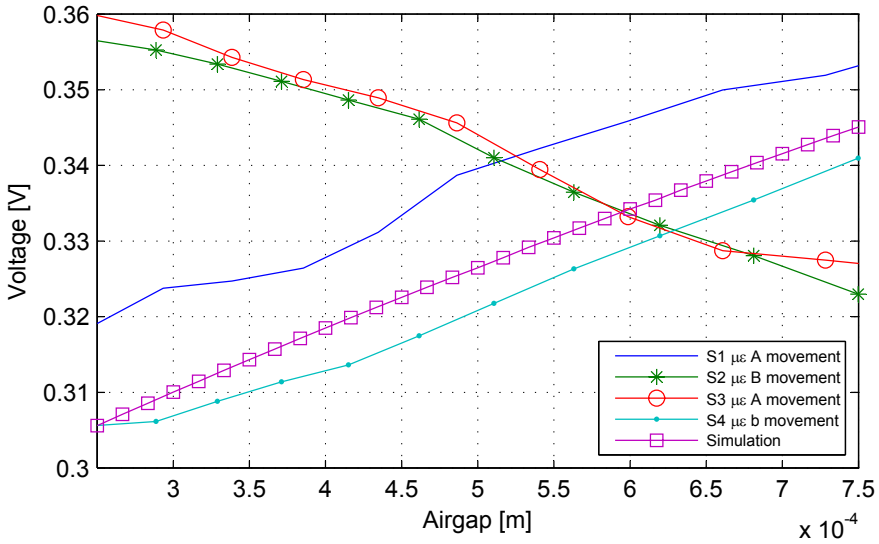

Figure 4.16: Changing measured and simulated induced sensing coil voltage voltage vs. airgap for movement in $\mu\epsilon$ A and B directions

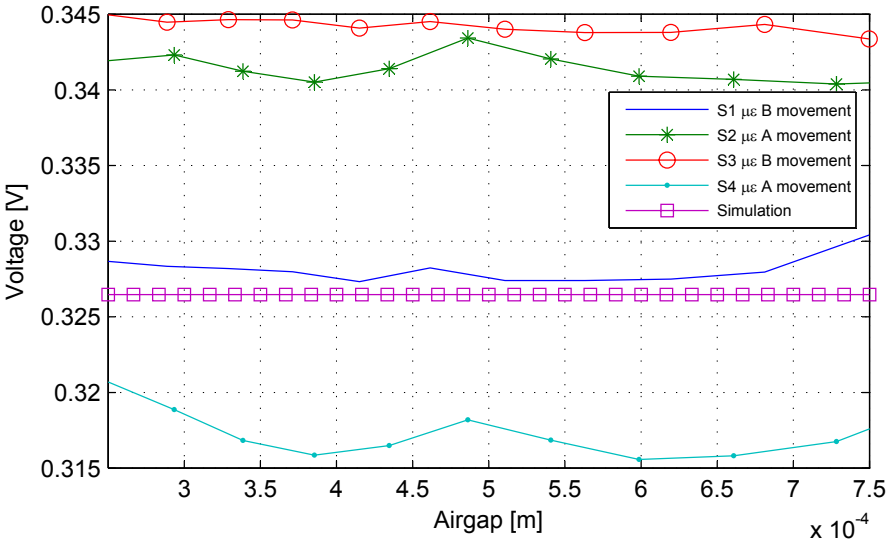

Figure 4.17: Constant measured and simulated induced sensing coil voltage vs. airgap for movement in $\mu\epsilon$ A and B directions

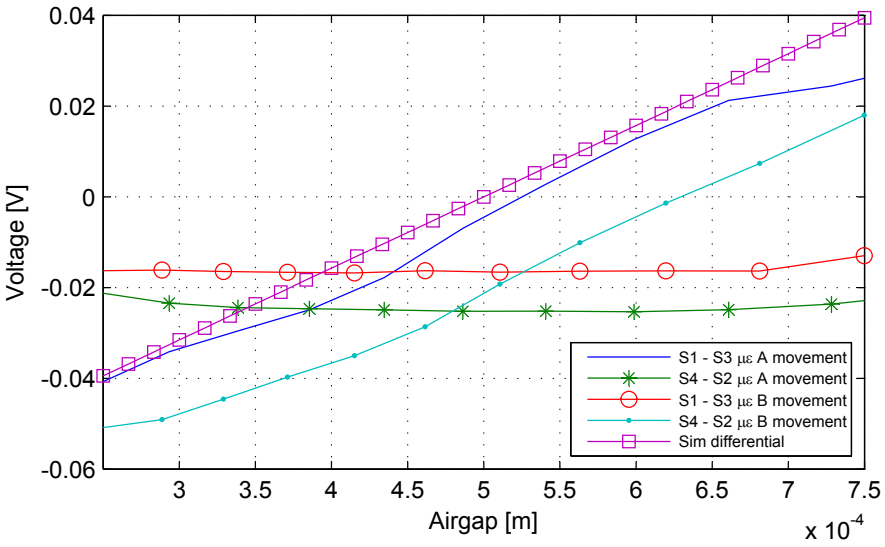

Figure 4.18: Differential sensing coil voltage vs. displacement (Sensor A and B) [2 MHz]

This confirms the accuracy of the FEM model for different target materials.

It can also clearly be seen that the predicted and measured results for the mild steel (Fe) does not correlate as good as the other materials. When considering the mild steel, the dc level of the induced voltage is larger than simulated results suggest. Conductivity's (σ) effect on the dc level of the induced sensing coil voltage was discussed in section 3.2.1. The magnetic and electric properties (σ, μ) of pure iron were used when modelling the mild steel. Although mild steel mainly consists out of iron, there are also other materials present to give certain mechanical properties. These impurities influence the σ and μ of mild steel, resulting in a difference between the simulated results and practical results. The skin depth for iron as calculated in (3.2) is the smallest of all the targets. This means that the mild steel target is the most susceptible to measuring irregularities caused by an uneven surface.

4.2.5 Calibrate performance parameters

Sensitivity

Sensitivity is the main optimisation parameter and it must be correctly predicted by the FEM model. Table 4.2 shows the measured and simulated sensitivity. It is clear that the largest difference in simulated and measured values are found when the mild steel target is used. Differences between simulation and practical in terms of electric and magnetic properties are responsible for this. These differences were discussed in the previous section.

Good correlation is observed between the simulated and measured results for the aluminium and stainless steel. The accuracy of the FEM model in terms of sensitivity is acceptable when

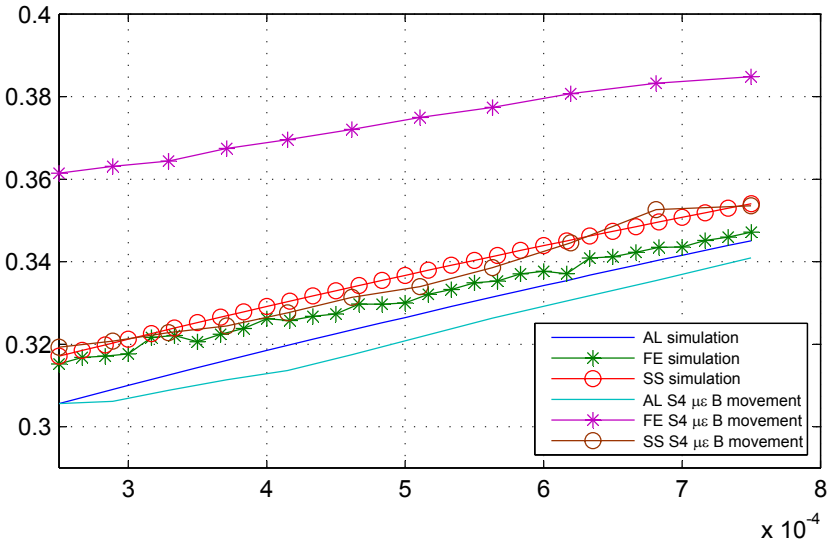

Figure 4.19: Changing sensing coil voltage (measured and simulated) vs. airgap when using different target materials

using it as a design tool. Differences could be caused by irregularities in the target material.

Table 4.2: Sensitivity comparison

Material	Sensing coil	Simulated [V/m]	Measured [V/m]	Difference [%]
Al	1	158	155.41	1.63
Al	2	158	140.12	11.31
Al	3	158	151.49	4.12
Al	4	158	147.85	6.42
Fe	2	127.73	94.49	25.59
Fe	4	127.73	99.84	21.84
Ss	2	148.62	138.35	6.91
Ss	4	148.62	148.37	0.17

Linearity

A very linear sensor output simplifies the demodulation circuitry or software. Linearity predicted by the simulation are compared to measured results in Table 4.3. The measured results are much more non-linear than expected for all the materials. All of the sensing coils have a linearity of between 10 % and 20 %. The linearity is very sensitive for the measuring irregularities such as oscillator drift, discussed in Appendix A. Difficulties with precise target positioning can also cause the linearity to deteriorate. Comparing the PCB sensor (9 % $\rightarrow$ 19 %) to the $\mu\epsilon$ sensors (17 % and 22 %) shows that these two sensors have similar linearities.

Table 4.3: Linearity comparison

Material	Sensing coil	Simulated [%]	Measured [%]
Al	1	0.14	13.46
Al	2	0.14	12.66
Al	3	0.14	18.83
Al	4	0.14	11.35
Fe	2	3.61	10.36
Fe	4	3.61	9.61
Ss	2	0.06	19.10
Ss	4	0.06	16.16

4.3 Conclusion

This chapter introduced the evaluation platform used to test PCB sensors. The targets, comparative sensors and drive circuit are all discussed in that section. The single-layer PCB sensor designed in chapter 3 is calibrated in the second part of this chapter. A very good correlation between simulated and measured results are found. The results for different targets are also

compared to simulated results. Only the mild steel has significant differences caused by incorrect material properties. The performance parameters correlate very well with the simulated results.

Chapter 5

Optimal multi-layer design

This chapter focuses on a double- and five-layer PCB sensor design and characterisation. Both these sensors are designed using the optimal design flow diagram discussed earlier. A double-layer sensor is manufactured and tested in the same way that the single-layer sensor was characterised. The chapter also compares the single-, double- and five-layer sensors in terms of cost and performance. The chapter is concluded with a discussion on additional performance influencing parameters.

5.1 Optimal double-layer sensor

5.1.1 Design process

Specifications

An optimal double-layer sensor is designed using the flow diagram presented in section 3.4. The first step in the design process is defining the electrical and mechanical constraints of the double-layer sensor as shown in Table 5.1. This sensor's constraints also include the thickness of the insulating material. The spacing between the top layer tracks and the bottom layer tracks are determined by this constraint. This must be incorporated into the FEM model in order to generate correct simulation results.

Temperature rise in excitation coil track

The next step is to determine the temperature rise in the track as a result of current flow. Temperature rise is only influenced by the track area and current flow, as shown in (3.9). These parameters are the same for this sensor as it was for the single-layer sensor. The temperature rise is thus also $T_r = 0.1043\ ^\circ\text{C}$, as was calculated for the single layer sensor in section 3.5.

Table 5.1: Electrical and mechanical constraints of a double-layer sensor.

Electrical	Value	Unit
Maximum rms Voltage (V_{rms})	10.6	V
Maximum rms Current (I_{rms})	0.1	A
Operating Frequency (f)	2	MHz
Mechanical		
Track height (h_t)	35	µm
Sensor measuring range (w_{mr})	500	µm
Min track width (w_t)	200	µm
Min track spacing (w_s)	200	µm
Airgap (w_{ag})	250	µm
Via diameter (d_{via})	700	µm
Axis size (w_{ax})	50	mm
Insulating material thickness	1.6	mm
Sensing coil angle (Φ)	50	degrees
Number of track layers	2	
Axis material	Aluminium	

Maximum excitation coil inductance

Drive circuitry requirements are also the same for the single and double-layer sensor. This means the excitation coil inductance also has the same maximum value : $L_{em} = 8.013$ µH. The formulas (Modified Wheeler(MW) and Geometric Mean Distance(GMD)) used in chapter 3 cannot be used to calculate the inductance when the target is placed in the sensor. Using Faraday's law of induction, (5.1) can be derived [20]. In this equation L is the inductance, N is the number of turns in the coil and $\mathcal{R}$ is the reluctance.

$$L = \frac{N^2}{\mathcal{R}} \tag{5.1}$$

Maximum number of excitation coil windings

The geometry and airgap of the single and double-layer sensors are similar. Since the reluctance of the excitation coil is dominated by the airgap component, it can be assumed that reluctance is constant, thus reducing (5.1) to (5.2). A constant (k) can be calculated from the inductance measurements shown in section 4.2.2, resulting in $k = 75.89 \times 10^{-9}$ H. Using k in (5.3), the maximum number of coils (N_{max}) is 10. The number of excitation coil windings is divided equally between the two layers, making $n_{exc} = 5$ on each of the two layers. This method for determining the inductance can be referred to as the reluctance method.

$$L_{em} = kN_{max}^2 \tag{5.2}$$

$$\begin{aligned} N_{max} &= \sqrt{\frac{L_{em}}{k}} \\ &= \sqrt{\frac{8\mu}{75.89\text{n}}} \\ &= 10.2 \\ \therefore N_{max} &\simeq 10 \end{aligned} \tag{5.3}$$

FEM model

The next step is solving the FEM model in order to find the number of sensing coil windings (n_{sens}) for an optimal position sensor. The FEM model must be altered to include the coils placed on the bottom layer of the PCB. Figure 5.1 shows the FEM geometry and magnetic field lines for n_{exc} = 5 and a insulation thickness of 1.6 mm. Even with such a large distance between the two excitation coils there exist magnetic coupling between these coils. The advantages this coupling holds will be discussed later in this chapter. It is assumed that for this design the standard 1.6 mm insulation is used during manufacturing.

The FEM model results are used to determine the optimal number of sensing coil windings. As discussed earlier this is on the turning point of the sensitivity's gradient. Figure 5.2 shows the sensitivity's gradient for $n_{exc} = 5$ and it is clear the turning point is where $n_{sens} = 7$. This results in a sensitivity of 250.1 V/m as shown in Figure 5.3.

The final step is verifying the combination chosen has an acceptable linearity. The linearity for $n_{exc} = 5$ and $n_{sens} = 7$ is 0.108 % FSO, as shown in Figure 5.4. This is an acceptable linearity for the application this sensor will be used in.

In this section the design of a double-layer sensor was presented. In the following section the

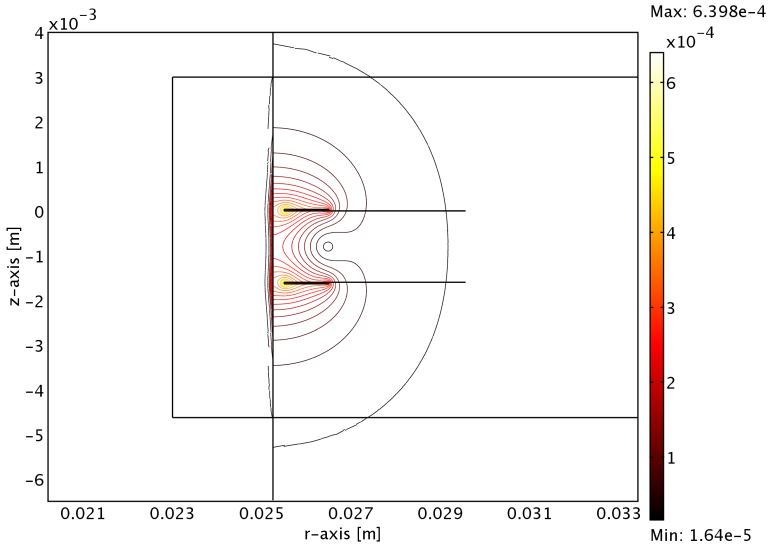

Figure 5.1: Domain plot of double-layer FEM model.

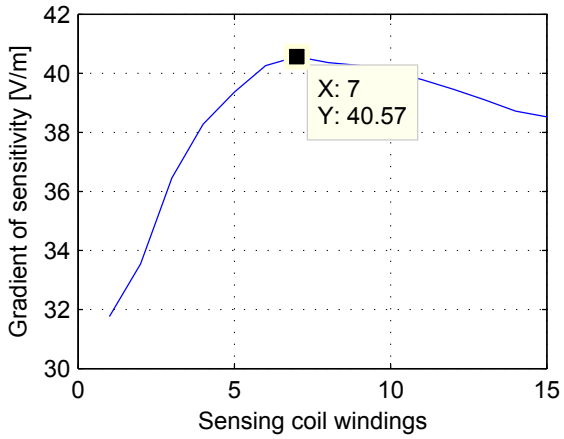

Figure 5.2: Gradient of sensitivity vs. sensing coil windings ($n_{sens} = 1 \rightarrow 15$) for a constant excitation coil ($n_{exc} = 5$).

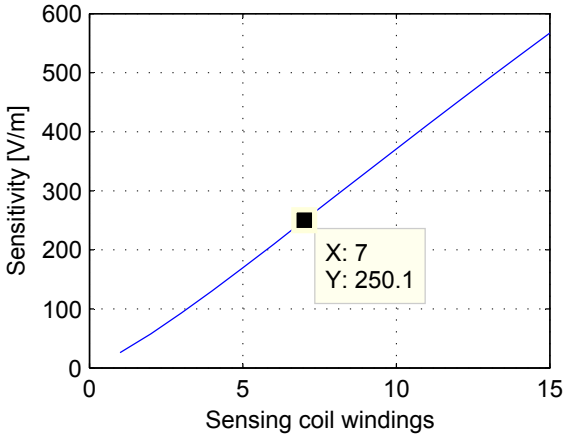

Figure 5.3: Sensitivity vs. sensing coil windings ($n_{sens} = 1 \rightarrow 15$) for a constant excitation coil ($n_{exc} = 5$).

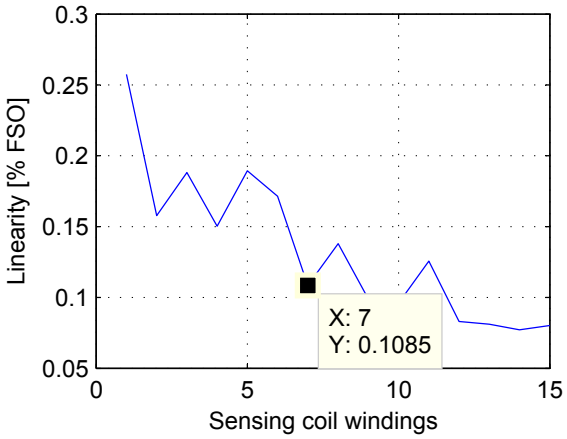

Figure 5.4: Linearity vs. sensing coil windings ($n_{sens} = 1 \rightarrow 15$) for a constant excitation winding ($n_{exc} = 5$).

manufactured double-layer sensor is characterised.

5.1.2 Sensor calibration

The manufactured optimal double-layer sensor is shown in Figure 5.5. The layout is similar to the single-layer sensor, except the coils are located on both sides of the PCB. There are 5 excitation coil windings on each side, resulting in a total of 10 excitation coil windings. Similarly there are 14 sensing coil windings per sensing coil, 7 on each layer. The excitation coils are routed to ensure the excitation current flows in the same direction on both levels. In this configuration the magnetic fields established in one level interacts with the sensing coils on the other level. The advantages of this interaction are explored later in the chapter.

One of the tracks between the DB 15 connector and sensing coil 2 was not connected correctly. This made it impossible to measure the induced voltage on this coil. The problem is solved by connecting the connector and track with a piece of copper wire that is roughly the same length the track should have been. The effect of this modification is explored later in the chapter.

Note that $\mu\epsilon$ sensor B is placed in line with sensing coils 1 and 3, and $\mu\epsilon$ sensor A in placed in line with sensing coils 2 and 4. In the next section the excitation coil is characterised.

Excitation coil characteristics

The excitation coil impedance is limited by the excitation circuit's capabilities. It is important to find a method that can be used to accurately predict these properties. Table 5.2 shows a summary of the predicted and measured values for resistance and inductance of the excitation

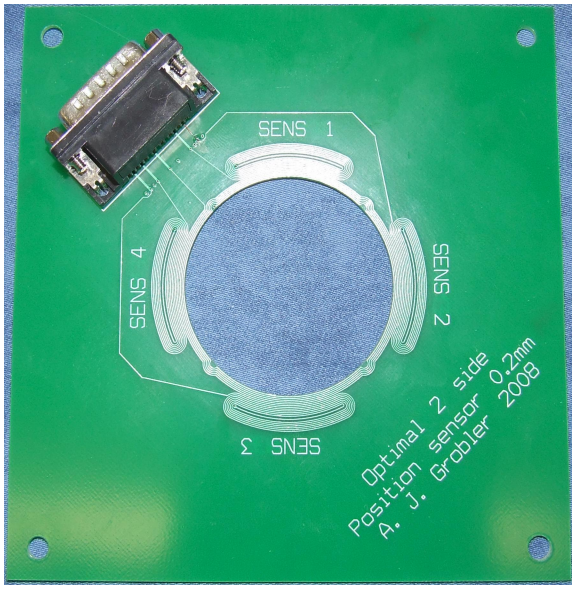

Figure 5.5: Double-layer sensor top view.

coil. These parameters were measured using the Grundig digimess® RLC 300 and calculated from the captured waveforms. The excitation coil inductances with the target in place is an important unknown when performing an optimal design. The two methods shown in the table that can be used to determine this property (FEM model and reluctance method are both inaccurate. The FEM result is smaller and the reluctance method result larger than the measured results respectively.

The FEM model results differ less than 13 % from the reality (Captured waveforms). It does not take into account the effect the insulating material's properties have on the properties of the excitation coil and must be refined. Reluctance method is based on the single-layer geometer which magnetically differs from the double-layer geometer. A more accurate way of predicting the excitation coil parameters must be found.

Induced sensing coil voltage comparison

A comparison between the measured and predicted induced voltages is done in this section. Figure 5.6 shows the induced voltages of all the sensing coils when moving the target in the $\mu\epsilon$ A and B directions. The expected results obtained using the FEM model are also shown in this figure.

Comparing the FEM model with a 1.6 mm airgap between the two layers to the measured results, a large dc offset is observed. It seems that the magnetic field coupling between the two layer's tracks are larger in the FEM model than the practical setup. The magnetic field coupling can be decreased in the simulation by moving the two layers further from each other. Figure 5.6 shows that the FEM model results for a 2.2 mm insulation layer correlates better with the measured results than the 1.6 mm insulation layer results.

When moving the target in the $\mu\epsilon$ A direction, the induced voltage on sensing coils 2 and 4 changes and the induced voltage of sensing coils 1 and 3 remains constant. Figure 5.7 shows the simulated and measured induced voltages for the sensing coils that are not influenced by the target movement. It is expected that the results of sensing coils 1 and 4 as well as 2 and 3 will be almost the same. This phenomenon is discussed in section A.5 of Appendix A and can be seen, for the single-layer sensor, in Figure 4.17. The absence of this pattern could be the effect of the modification made on the board that was discussed earlier.

Table 5.2: Excitation coil characteristics summary: Double layer.

	Target in place		No target	
Method	L [µH]	R [Ω]	L [µH]	R [Ω]
FEM model	4.043	9.578	11.158	4.263
Reluctance method	8	-	-	-
Modified Wheeler	-	-	12.170	-
Geometric Mean Distance	-	-	12.360	-
Captured waveforms	4.644	8.678	12.480	6.465
RLC meter	5.234	7.942	11.852	7.945

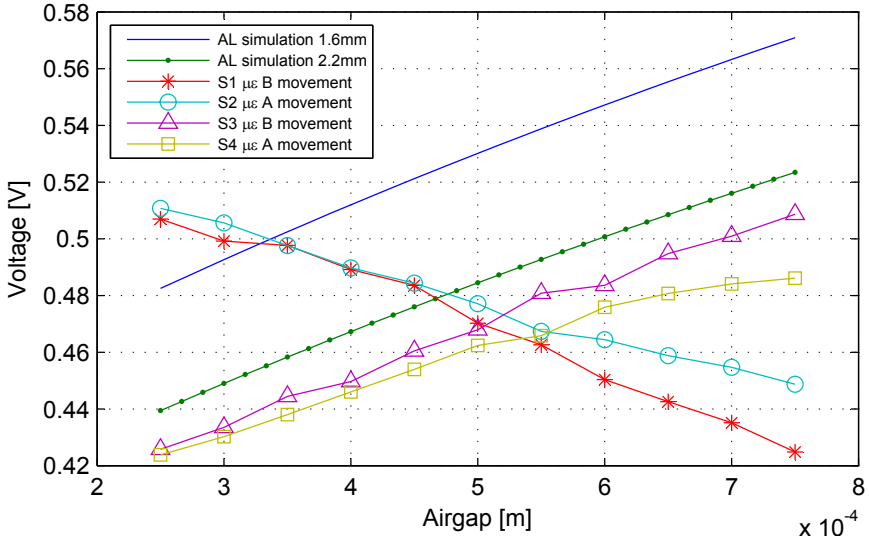

Figure 5.6: Induced sensing coil voltage (measured and simulated) vs. airgap for movement in $\mu\epsilon$ A and B direction.

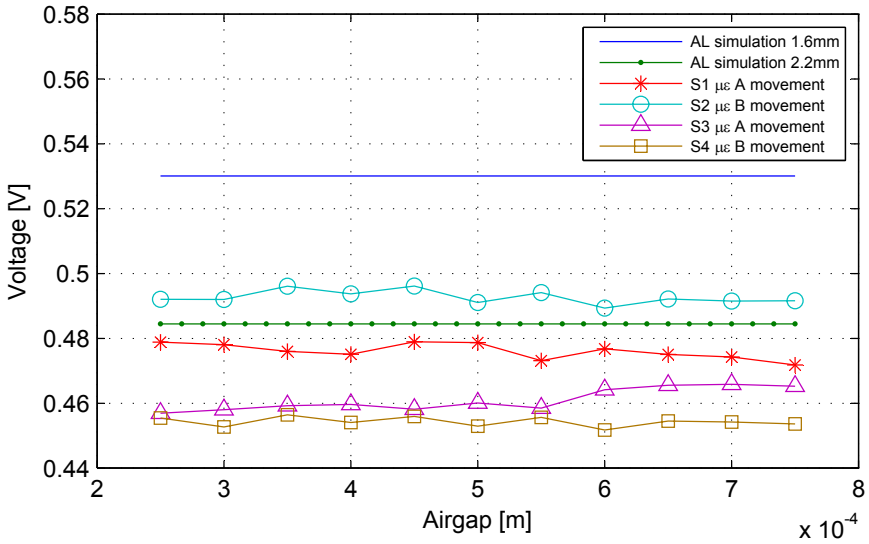

Figure 5.7: Induced sensing coil voltage (measured and simulated) vs. airgap for movement in $\mu\epsilon$ A and B direction.

The dc offset is less of a concern when using a differential measuring strategy, as can be seen in Figure 5.8. Both simulated results are centred around 0 V_{dc} but the gradients differ slightly. There is a large difference between the varying voltages : S4 - S2 $\mu\epsilon$ A movement and S3 - S1 $\mu\epsilon$ B movement. The results when moving in the $\mu\epsilon$ B sensor direction correlates closely with the simulation results. For the first half of the movement range, the simulation and $\mu\epsilon$ A movement also correlates. When moving the target further away from the $\mu\epsilon$ A sensor, the differences between the simulated and practical results increase. This phenomenon can be attributed to the modification made to the sensor.

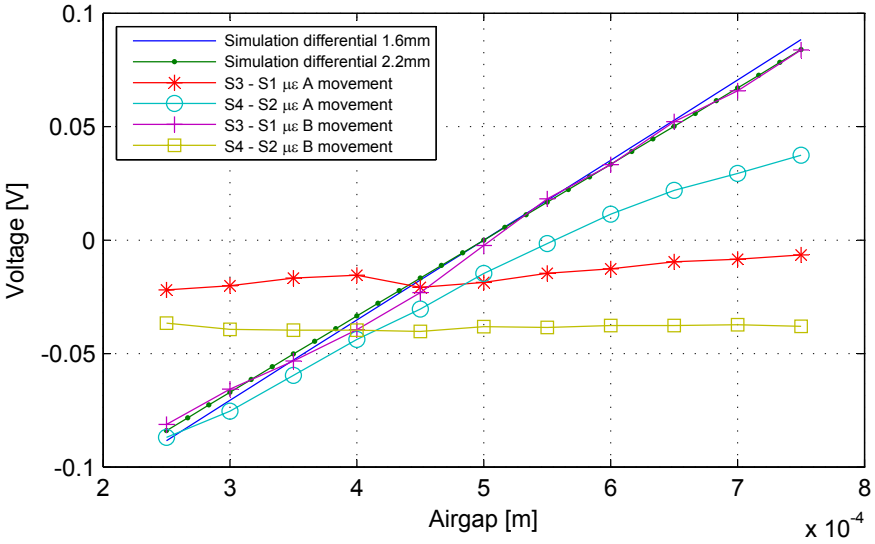

Figure 5.8: Induced sensing coil voltage (measured and simulated) vs. airgap for movement in $\mu\epsilon$ A and B direction.

Performance parameters

The final step in calibration of the double-layer sensor is comparing the performance parameters measured to those predicted. Table 5.3 shows the sensitivity of the simulated and measured results when an aluminium target is used. The values listed in the last column is the deviation between the simulated and measured results, in percentage. The deviation of sensing coils 1 and 3 are less than 5 %; a very good correlation. Sensing coils 2 and 4 results do not correlate as well, showing a larger than 20 % deviation. These results exhibit the same trend in the error as seen throughout this section, when moving the target in the $\mu\epsilon$ A direction.

Table 5.4 summarises the linearity of the simulated and measured results when an aluminium target is used. The measured linearities are much larger than the simulated linearities, as was the case with the single-layer sensor. On average the linearity of the double-layer sensor is better than the single-layer sensor's linearity.

This concludes the double-layer sensor design and calibration. In the next section a optimal five-layer sensor is designed.

Table 5.3: Sensitivity comparison: Double-layer with Aluminium target.

Sensing coil	Sim 1.6 mm [V/m]	Sim 2.2 mm [V/m]	Measured [V/m]	Deviation [%] 1.6 mm	2.2 mm
1	352.92	335.25	338.50	4.08	0.96
2	352.92	335.25	253.85	28.07	24.28
3	352.92	335.25	335.73	4.87	0.14
4	352.92	335.25	264.16	25.15	21.2

Table 5.4: Linearity comparison: Double-layer with Aluminium target.

Sensing coil	Sim 1.6mm [%]	Sim 2.2mm [%]	Measured [%]
1	0.13	0.14	12.35
2	0.13	0.14	10.62
3	0.13	0.14	7.17
4	0.13	0.14	14.43

5.2 Optimal five-layer sensor

This section presents the design of an optimal five-layer PCB sensor.

5.2.1 Design

Specifications

The specifications of the five-layer sensor are given in Table 5.5. The only differences between the double and five-layer sensor is the number of layers and the insulating material thickness.

Temperature rise in excitation coil

The first step in the design process is checking that the excitation coil is suited to carry the specified excitation current. The temperature rise is the same for the single, double and five layer sensor since the geometries and excitation currents are the same for all three sensors.

Maximum number of excitation coil windings

The excitation coil inductance directly influences the maximum number of excitation coil windings that can be used. In the five-layer sensor the total number of excitation coil windings are multiples of five. One, two and three windings per layer will result in a total number of excitation coil windings of five, ten and fifteen respectively. The excitation coil inductance, determined using the FEM model, is shown in Table 5.6. The inductance for $n_{exc} = 3$ is larger than

Table 5.5: Electrical and mechanical constraints of a five-layer sensor.

Electrical	Value	Unit
Maximum RMS Voltage (V_{rms})	10.6	V
Maximum RMS Current (I_{rms})	0.1	A
Operating Frequency (f)	2	MHz
Mechanical		
Track hight (h_t)	35	µm
Sensor measuring range (w_{mr})	500	µm
Min track width (w_t)	200	µm
Min track spacing (w_s)	200	µm
Airgap (w_{ag})	250	µm
Via diameter (d_{via})	700	µm
Axis size (w_{ax})	50	mm
Sensing coil angle (Φ)	50	degrees
Insulating material thickness	0.2	mm
Number of track layers	5	
Axis material	Aluminium	

L_{em} and thus only n_{exc} = 1,2 can be considered. From these results it is clear n_{exc} = 2 (total of 10 excitation coil windings) is the maximum number of excitation coil windings that can be used in a five layer sensor.

FEM model results

The next step in the design process is analysing the FEM model of the five-layer design. Figure 5.9 shows the magnetic field lines of the five-layer sensor when a 0.2 mm insulation material is used. The magnetic fields generated by the excitation coil windings on the different levels interact with one another, increasing the total magnetic flux passing through the sensing coils. In this configuration the sensing coils are connected in series. The voltages induced in each of the levels are thus added together when measuring over this combination of coils.

The gradient of the sensitivity for a constant number of excitation coils ($n_{exc} = 2$) is shown in Figure 5.10. Note that there are two windings per layer, resulting in ten windings forming the excitation coil. The turing point is at n_{sens} = 2, also resulting in a total number of sensing coil windings of ten.

Table 5.6: Five-layer excitation coil inductance using FEM model.

n_{exc}	Total number of excitation coil windings	L with target [µH]	L without target [µH]
1	5	1.252	3.6046
2	10	4.6766	13.394
3	15	10.0325	28.773

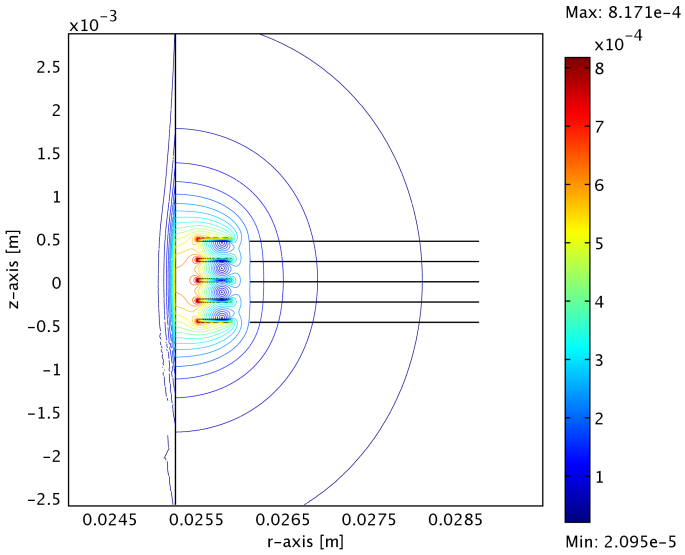

Figure 5.9: Domain plot of five-layer FEM model.

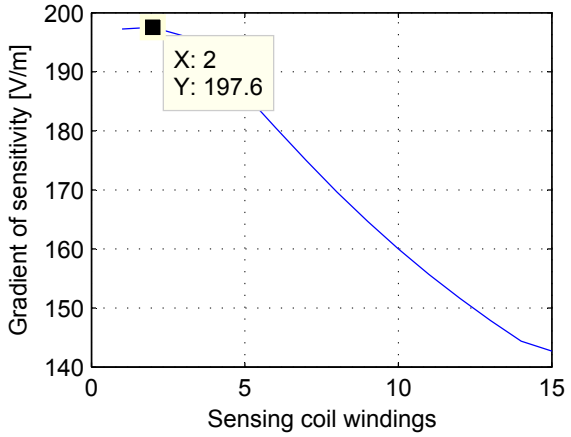

Figure 5.10: Gradient of sensitivity vs. sensing coil windings ($n_{exc} = 1 \rightarrow 15$) for a constant number of excitation coil windings ($n_{exc} = 2$).

Figure 5.11 shows the sensitivity of the five-layer sensor for a constant number of excitation coil windings ($n_{exc} = 2$). The sensitivity is 383.7 V/m at $n_{sens} = 2$ and 1326 V/m at $n_{sens} = 7$, a 346 % improvement on the former. The effect of using more sensing coil windings than suggested by the sensitivity gradient turning point will be discussed in more detail later in this chapter.

The linearity for a constant number of excitation coil windings ($n_{exc} = 2$) is shown in Figure 5.12. As found in all the previous FEM model results, the linearity is very good.

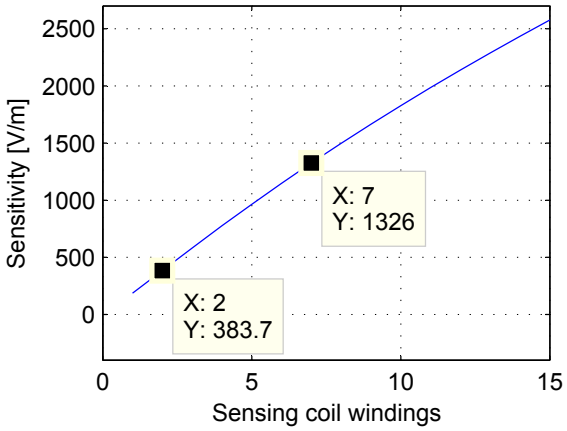

Figure 5.11: Sensitivity vs. sensing coil windings ($n_{sens} = 1 \rightarrow 15$) for a constant number of excitation coil windings ($n_{exc} = 2$).

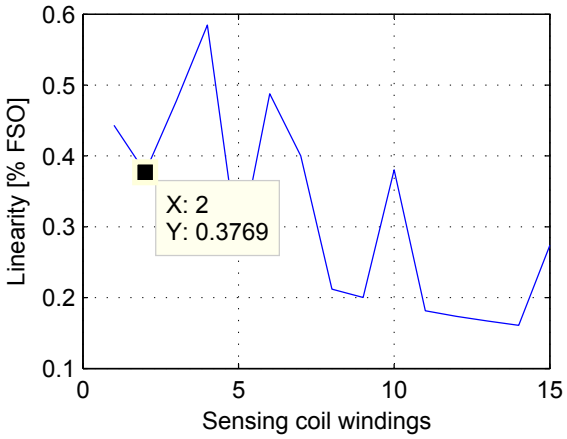

Figure 5.12: Linearity vs. sensing coil windings ($n_{sens} = 1 \rightarrow 15$) for a constant number of excitation coil windings ($n_{exc} = 2$).

5.3 Comparing single, double and five-layer sensors

Comparing the different sensors designed in this document is important as it gives more insight to what sensor is best suited for a specific application.

Figure 5.13 shows the voltages induced on the sensing coils for a single, double and two five-layer sensors. The first three sensors were designed using the optimal design process as discussed in section 3.4. The last sensor (Five-layer $n_{exc} = 2$, $n_{sens} = 7$) is included to highlight the advantages of increasing the number of sensing coil windings. First, just the dc levels of the different sensors are compared. Similar dc offsets are found for the double and five-layer optimal sensors. These are larger than the dc offset of the single layer optimal sensor. The last sensor has the largest dc offset of all the sensors displayed. A large dc offset is beneficial for the demodulation circuitry since the signal average voltage is much higher than the noise level.

Differential measurement results, centred around 0 V_{dc}, are shown in Figure 5.14. In this case the gradient of the signals are more important than the level. The gradient increases gradually between 315.6 - 1093.6 V/m for the optimal sensors. The last sensor's sensitivity is 3767.2, which is much larger than the other three.

The four sensors can be compared using a decision making matrix as shown in Table 5.7. The sensors are compared in terms of sensitivity, average voltage level and cost. This project focuses on a low cost sensor, thus cost carries the most weight in this comparison. Linearity is similar for all the sensors and is therefor not included in this comparison.

The five-layer sensor might have superior sensitivity but this comes with a huge disadvantage: this sensor is ten times more expensive to manufacture than the single and double-layer sensors. This is also highlighted in the decision making matrix where the double layer sensor has the highest score. The double-layer sensor costs the same as the single-layer sensor but has a

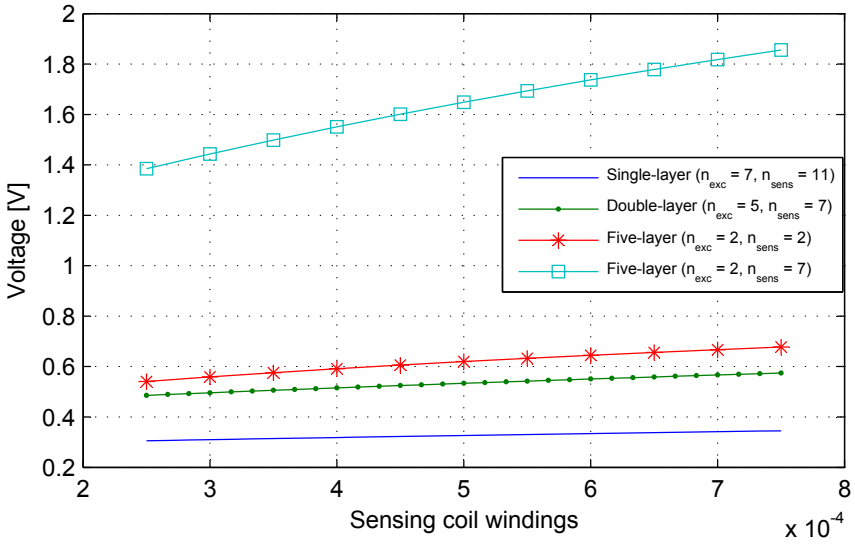

Figure 5.13: Induced sensing coil voltage vs. displacement for 1, 2 and 5 layer sensors.

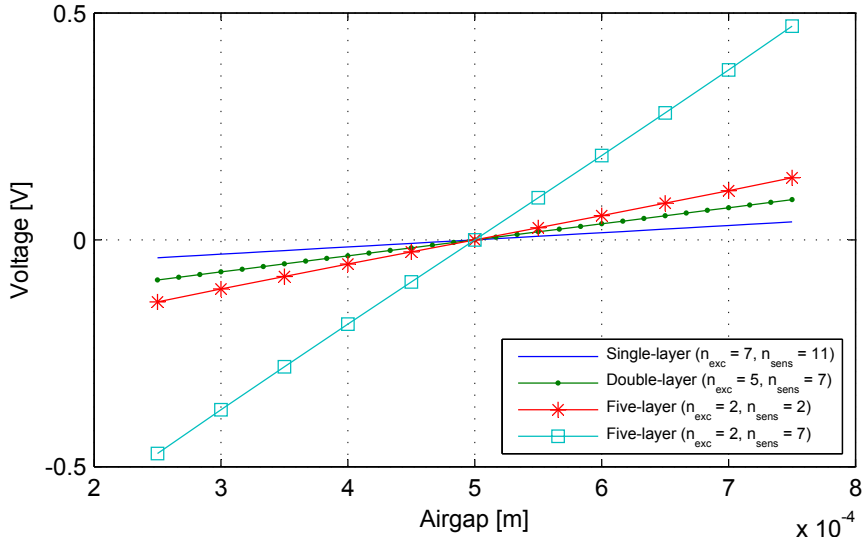

Figure 5.14: Differential voltage vs. displacement for 1, 2 and 5 layer sensors.

larger sensitivity. This sensitivity can be improved by increasing the number of sensing coil windings as illustrated with the two five-layer sensors.

Table 5.7: Decision making matrix comparing 1, 2 and 5 layer sensors.

Characteristic	Sensitivity (10)	Average voltage (10)	Cost (10)	Score (10)
Weighting factor	0.4	0.1	0.5	1
Sensor (n_{exc}, n_{sens})				
Single-layer (7, 11)	2	2	8	5
Double-layer (5, 7)	4	4	8	6
Five-layer (2, 2)	6	6	2	4
Five-layer (2, 7)	7	7	2	4.5

This concludes the comparison between the single, double and five-layer sensors. The next section introduces some of the other factors that influences the performance parameters and cost that has not been discussed previously.

5.4 Additional performance influencing parameters

Choosing values for some of the less important variables are commonly done to ease the design process. This section analyses the effects two of these variables have on the performance parameters and costs.

5.4.1 Track width and track spacing

The track spacing (w_s) and track width (w_t) are dependent on the manufacturing process, as discussed in section 3.1.1. All the sensors, designed and implemented thus far, had $w_t = w_s =$ 200 µm. In this section the effects of decreasing w_s and w_t are explored.

Figure 5.15 shows the induced voltage for four combinations of excitation coil track width and sensing coil track width. The results are based on the single-layer FEM model with $n_{exc} = 7$ and $n_{sens} = 11$ for all of the combinations. In these results the track width and track spacing are the same for a specific coil. The combination where both the excitation coil track width (excitation coil w_t) and sensing coil track width (sensing coil w_t) is 100 µm has the largest average voltage level. From this figure it is clear that a smaller excitation coil track width results in a larger average voltage level.

The differential results of the induced voltages are shown in Figure 5.16. Sensitivity values, for each of the combinations,is also shown in the legend of the Figure 5.16. Excitation coil track thickness significantly influences the sensitivity; an increase of more than 1.8 times is found when this thickness is reduced from 200 µm to 100 µm. A smaller excitation coil track width means the sensing coils are located closer to the target. This places the sensing coils in a region where the magnetic fields are more sensitive for target movement. The induced voltage is therefore also more sensitive to target movement, resulting in a sensor with a larger sensitivity.

Sensing coil track width also influences the sensitivity but not nearly as significantly as excitation coil track width. An increase in sensing coil track width causes an increase in sensitivity. Voltage induced in the sensing coil is directly proportional to the amount of magnetic flux passing through it. A larger sensing coil area causes more magnetic flux to pass through the sensing coil, thus a larger voltage is induced. The sensor is also more sensitive since the area in which

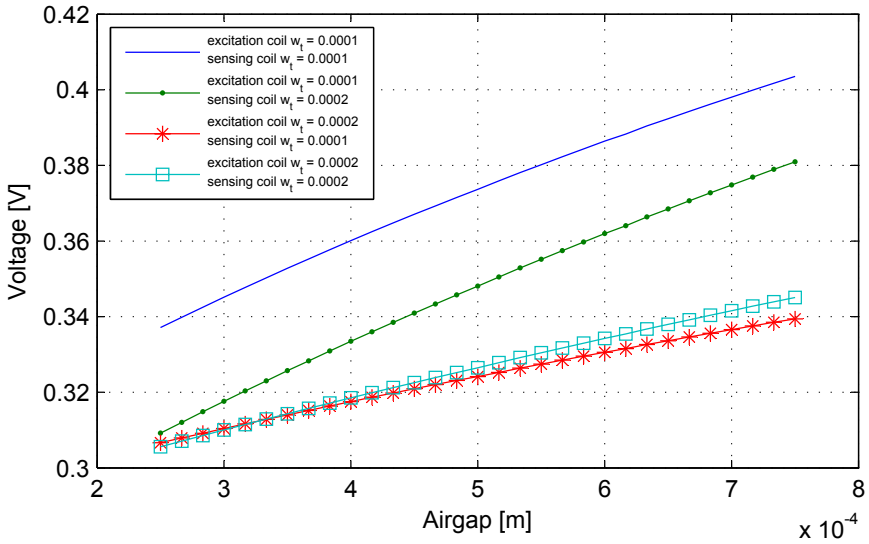

Figure 5.15: Induced sensing coil voltage vs. displacement for different track spacing and track width.

the magnetic field changes is larger.

The track width used throughout this document ($w_t = w_s = 200$ µm) was used since it is the thinnest track most South African PCB manufacturers can produce. Only companies, based in countries such as Israel and England, can manufacture 100 µm wide tracks. These PCBs are ten times more expensive than the 200 µm wide track boards manufactured in South-Africa. Using a thin track (< 200 µm) is thus not economically viable.

This concludes the discussion of the effects track width and track spacing have on the sensor parameters and cost. Next the insulation material thickness is discussed.

5.4.2 Insulation material thickness

Varying the insulation material thickness and the effect this has on a PCB sensor is discussed in this section. The insulation material used in PCBs are made from epoxy resin that is reinforced with woven fibreglass. Insulation material thickness directly influences the distance between tracks placed on the top and bottom layers of the PCB. The results used in this section are generated by the FEM model for a double-layer sensor with $n_{exc} = 5$ and $n_{sens} = 7$.

Figure 5.17 shows the sensing coil induced voltage for a moving target and varying insulation material thickness (fr4). In this graph it is clear that decreasing insulation material thickness increases the dc level of the induced voltage. Using a thinner insulation material decreases the distance between the top and bottom-layer tracks. More of the magnetic fields generated by the top layer excitation coil couples with the bottom sensing coils and vice versa. This results in a larger induced voltage when the insulation material is thinner.

The differential results of the induced voltages discussed above are shown in Figure 5.18. Sen-

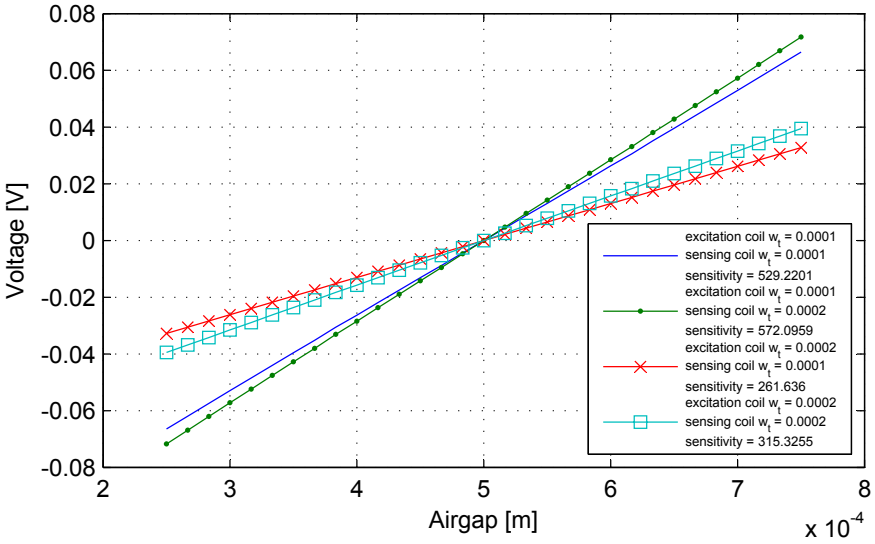

Figure 5.16: Differential voltage vs. displacement for different track spacing and track width.

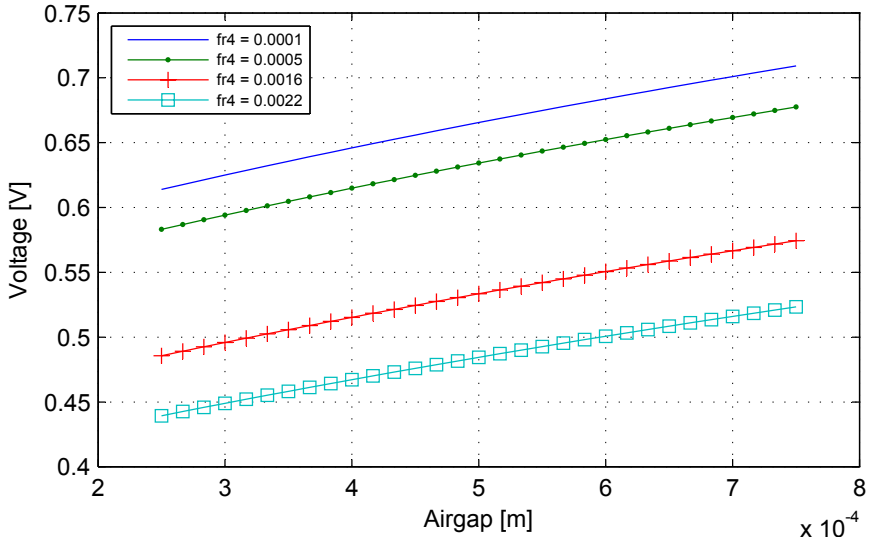

Figure 5.17: Induced sensing coil voltage vs. displacement for different insulation material thicknesses.

sitivity is also shown in the legend of this figure. Insulation track thickness does not influence the sensitivity as much as the dc level. Only a 13 % difference is found between the smallest (100 µm) and largest (2.2 mm) insulation track thickness. Furthermore, reducing the insulation thickness also reduces the mechanical strength of the PCB construction. From these results it seems modifying the insulation track thickness to improve sensitivity is not viable.

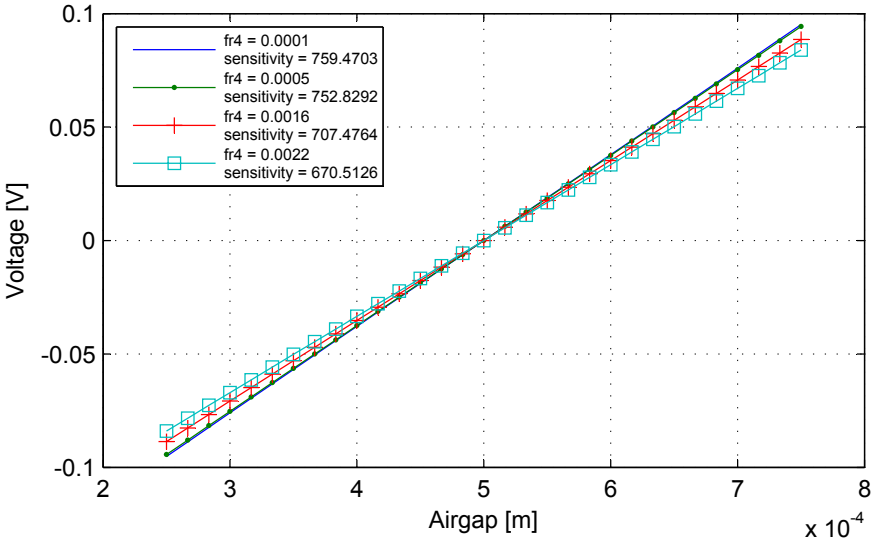

Figure 5.18: Differential voltage vs. displacement for different insulation material thicknesses.

5.5 Conclusion

This chapter started with a discussion of the design and calibration of an optimal double-layer sensor. Good correlation between the FEM model results and manufactured sensor results were found. The design of a five-layer sensor was presented and it has the largest sensitivity of all the sensors discussed. This was followed by a formal comparison between the single, double and five-layer sensor in terms of sensitivity, average voltage and cost. The double-layer is the best choice according to the decision making matrix since it has acceptable sensitivity as well as low cost.

Finally, two additional influencing factors were discussed, i.e. track width and insulation material thickness. It was shown that the performance of a sensor can be improved by decreasing the track width and spacing. This however has the disadvantage of a large increase in cost. Decreasing the insulating material thickness does not result in any significant improvement in performance.

The results included in this chapter established that the optimal design flow diagram can be used to design sensors that are optimal in terms of size and performance. It also shows that using a larger number of sensing coil winding, than suggested by the optimal design flow diagram, has a positive effect on the performance. A double-layer sensor, with more sensing coil windings than suggested by the optimal design flow diagram, will render a low cost sensor with acceptable performance.

Chapter 6

Conclusions and recommendations

This chapter summarises the most important conclusions of the project as well as some unresolved issues which warrant future work.

6.1 Conclusions

This project laid the foundation for PCB eddy current displacement sensor design in the McTronX group. This section presents the highlights of this project, starting with the FEM model and design flow diagram.

6.1.1 FEM model and design flow diagram

The first step in designing an eddy current displacement sensor was to derive a FEM model for the sensor. This FEM model can be used to predict sensor behaviour in different configurations, i.e. combinations of target material, excitation coil current, number of excitation and sensing coil windings, airgap, track spacing and track width etc. The simulated results were compared to practical results and these correlated closely for the single layer sensor. Sensitivity differed less than 10 % for aluminium and stainless steel. FEM models were also compiled for the double- and five-layer sensors. The average voltage correlation between predicted and practical results differs more than 10 % for the double-layer FEM model. The single-layer FEM model's average voltage differed less than 5 % between the measured and predicted results. Refinement of the multi-layer FEM model should be done. The FEM model was also used in the design process.

An optimal design flow diagram, based on the trends found in the FEM results and some analytical formulas, were derived. This flow diagram was implemented on a single-, double- and five-layer sensor design to illustrate its use. From the close correlation between the practical and simulated results for both the single- and double-layer sensor it is clear that this flow diagram is indeed useful. The design flow diagram is easy to use and can be used to design

sensors for different configurations. It does not take into account spatial limitations but rather focuses on sensitivity and linearity. Spatial limitations should be taken into account in future.

6.1.2 Sensor

During this project two PCB displacement sensors, a single-layer and a double layer, were manufactured. Both sensors were manufactured to required accuracy and timeously by local PCB industries. It can be concluded that this is a viable solution to the problem in terms of executability. This project did not explore the integration of a PCB sensor into an AMB. Sensor mounting, materials used and heat effects must be explored before this sensor can be commercially implemented.

One of the other concerns addressed by this project is the high cost of displacement sensors in AMBs. A PCB sensor can be locally manufactured at a fraction of the cost of other position sensors. The machinery and skills required to manufacture a PCB sensor are readily available in South Africa. Locally manufactured sensors are beneficial for the South African economy since it decreases imports and supports job creation.

The single-, double- and five-layer sensors were compared in terms of sensitivity, average voltage and cost. The five-layer sensor has superior sensitivity and average voltage but is ten times more expensive than the other two sensors. The single- and double-layer sensor has the same manufacturing cost, but the latter has a much larger sensitivity. It is concluded that a double-layer sensor is the best solution to the problem.

6.1.3 Evaluation platform

This project made use of a simple voltage-to-current converting drive circuit. It successfully supplied the power needed to drive the excitation coil during testing and calibration. Problems such as signal drift were not caused by the drive circuit but rather by the signal generator used as an oscillator input for the drive circuit. The design of a compact, stable drive circuit that includes the oscillator remains.

The induced sensing coil voltages were captured using a digital oscilloscope and demodulated using MATLAB® software on a personal computer. Using software, only the operating frequency (2 MHz) component of the induced voltage could be extracted and analysed to compare with the measured results. A demodulation circuit, able of supplying a position output to a controller, should be designed.

A test platform, used to calibrate the sensor, was also designed and manufactured as part of this project. Three targets, made form aluminium, stainless steel and mild steel, were manufactured and used in testing. Different target materials and different target sizes can easily be tested on this platform by only replacing the target. All the results shown in this document were measured using this evaluation platform. The test platform is difficult to use and should be modified to better simulate the AMB environment.

6.2 Recommendations

This section discusses some of the unresolved issues and work that should be done in future.

6.2.1 FEM model and design flow diagram

Determining the inductance of the excitation coil, when the target is in place, must be refined. Neither the FEM model nor the analytical formulas gave accurate results for this inductance. A three dimensional FEM model could be explored, but would be computationally intensive. The problem can also be solved by deriving analytical formulas for conductive core planar coils using Maxwell's equations. No analytical models for this specific configuration were found in the literature.

The FEM model for multi-layer sensors is incomplete since the insulation material has not been included in the simulations. This influences the inductance calculated with the FEM for multi-layer configurations. The sensor will be used inside an AMB, thus the materials that are present in this environment must also be included in the FEM model. The effect the AMB electromagnets have on the sensor can also be investigated with such a simulation but might require three-dimensional modelling since the magnetic fields are distributed in different directions.

The design flow diagram does not take into account spatial limits such as maximum sensor diameter and thickness. Only sensitivity and linearity are used as optimisation factors. It is possible to design a sensor, using this flow diagram, that is physically too big to fit into the mounting space provided. A sensor that does not use all the available space effectively can be also designed using the flow diagram presented in this dissertation. The spatial limitations should be included in the design flow diagram.

6.2.2 Sensor

The sensor implementation has not been explored extensively in this project. Before integrating the sensor into an AMB system, it must be ensured that the sensor will operate correctly in this environment. The sensor and sensor mount should be designed with mechanical factors, such as temperature changes and vibration effects, in mind. The materials used to manufacture the PCB tracks and insulating material must also be researched with the application in mind. When designing a sensor for high temperature applications, other materials for the tracks and insulation should be explored.

6.2.3 Evaluation platform

The oscillator output connected to the drive circuit has a large effect on the sensor operation, since it directly influences the induced voltage. This effect is discussed in detail in Appendix A.4. With the signal generator used, the amplitude drift was significantly larger than the fre-

quency drift. In an ideal sensor, the oscillator should be very stable and immune to temperature fluctuations. The induced voltages are directly proportional to the excitation coil current, which in turn in directly proportional to the oscillator voltage. The excitation coil current or oscillator voltage can be measured and used when interpreting the induced sensing coil voltage inside the detector. This can help eradicate the effect of oscillator drift. In this scenario the change in coil inductance, rather than the absolute value of the induced voltage, is used as a measure of the radial movement. This would increase the complexity and cost of the detector circuitry and should only be done as a last resort.

In this project the induced voltages were captured with a digital oscilloscope and demodulated using software. Detector circuitry that can be placed close to the sensor should be developed. Only the induced voltage at the operating frequency must be detected. This will minimise noise caused by the electromagnets and other electromagnetic sources. The detector circuitry must amplify and condition the position signal for input to the control system. Digital transmission of the position signal has various advantages and must be considered. It is less susceptible to noise and can be transmitted over longer distances than analog communication. Cost involved in digitising the position signal is the main drawback of digital communication but this should be investigated.

The environment in which the demodulation circuitry will be placed must also be considered. Placing the demodulation circuitry close to the sensor can help minimise the noise coupling onto the induced voltage through the connecting cable. This might not be viable if the environment in the vicinity of the AMB is not suited for PCBs. In this case, the connection between the sensor and demodulation electronics should be designed with care. The connecting cables must be sufficiently shielded to keep noise and cross-coupling to a minimum.

Improving the evaluation platform must also be considered. Spring-loading the target will ensure it stays completely tangent relative to the sensor while still maintaining ease of movement. The actuators used to move the target, fine thread M10 bolts, are inadequate to accurately and easily move the target in micrometer steps. The M10 fine threaded bolt has a 1 mm pitch, in other words, for each revolution the bolt experiences 1 mm translational movement. This method for moving the target is very time-consuming since the four bolts must be adjusted by hand until the target is at the required position. An actuator, capable of highly repeatable movement should be considered. An AMB could be used as actuator but this would greatly increase the evaluation platform's cost. Using a finer thread bolt can improve the resolution of target movement, since the rotational movement is larger for the same translational movement when compared to a bolt with a larger thread.

The $\mu\epsilon$ sensors used as a reference sensor in the evaluation platform must be calibrated using a high precision method, according to commonly accepted methods and standards. This would ensure accurate calibration of the PCB sensors.

6.2.4 Additional remarks

The sensor should be tested in an AMB system. It is expected that the effect of noise on the system will not be extensive. This can be attributed to the high operating frequency and differ-

ential measuring principle that is used.

The sensor developed in this project can be used to measure radial and axial position as well as rotational speed. This can be achieved by modifying the rotor and demodulation circuitry. An investigation into this should be done as it would decrease the total cost of the sensors in an AMB system even more. This may also require that some intelligence, such as a microcontroller or digital signal processor, be included in the demodulation circuitry.

6.3 Closure

This project set out to design, simulate, manufacture and test a low cost eddy current displacement sensor, all of which were addressed. A design process were deduced and implemented on single-, double- and five-layer sensors. A FEM model for all these sensors were compiled and used in the design process. The measured and simulated results correlated closely, thus proving the accuracy of the FEM model and design process. A single- and double-layer sensor were manufactured using low cost PCB methods. These sensors were tested using the evaluation platform. This project showed that PCB eddy current sensors are a viable low cost option for displacement measurement in AMBs.

Bibliography

[1] E. O. Ranft, "The development of a flexible rotor active magnetic bearing system," Master's thesis, North West University, Potchefstroom, RSA, May 2005.

[2] J. J. Janse van Rensburg, "Development of a flywheel energy storage system - uninterrupted power supply," Master's thesis, North West University, Potchefstroom, RSA, December 2007.

[3] J. Jansen van Rensburg, "An intergrated controller for an active magnetic bearing system," Master's thesis, North West University, Potchefstroom, RSA, December 2007.

[4] R. Larsonneur and P. Bühler, "New radial sensor for active magnetic bearings," in *International Symposium on Magnetic Bearings*, no. 9, Lexington, Kentucky, USA, August 2004.

[5] A. C. Niemann, "Design and development of sensors for active magnetic bearings," Master's thesis, North West University, Potchefstroom, RSA, June 2005.

[6] G. Schweitzer, H. Bleuler, and A. Traxler, *Active magnetic bearings : Basics, Properties and Applications of Active magnetic bearings*. Zurich: Authors Working Group, 2003.

[7] D. B. Guralnik, S. Solomon, and W. T. McLeod, Eds., *Collins Concise Dictionry of the English Language*. London, UK: William Collins, 1980.

[8] A. F. Kip, *Fundamentals of Eletricity and Magnetism*. London, UK: McGraw-Hill, 1962.

[9] J. Cathey, *Electric machines : Analysis and design applying MATLAB®*. McGraw-Hill, 2001.

[10] G. Y. Tian, Z. X. Zhao, and R. W. Baines, "The research of inhomogeneity in eddy current sensor," *Sensors and Actuators*, vol. A 69, pp. 148–151, 1998.

[11] N. K. K. Kaisha, "Apparatus for non-contact measurement of distance between a metallic body and a detection coil," UK Patent 1 512 799, 1975.

[12] ——, "Eddy-current distance measuring apparatus," U K Patent 2 054 867, 1980.

[13] S. D. Roach, "Designing and building an eddy current position sensor," *Sensors*, September 1998.

[14] P. Bühler, "Device for cantact-less measurement of distances in multiple directions," Europe Patent 1 422 492, 2002.

[15] L. Burdet, T. Maeder, R. Siegwart, P. Bühler, and B. Aeschlimann, "Thick-film radial position sensor for high temperature active magnetic bearings," in *Symposium on Magnetic Bearings*, no. 10, Marigny, Switzerland, August 2006.

[16] R. Pallas-Areny, *Sensors and signal conditioning*, 2nd ed. New York, USA: Wiley, 2001.

[17] *eddyNDCT 3700*, Micro-Epsilon, Ortenburg, Germany, 2006.

[18] R. Kirchdoerffer and V. Frolov, "Inductive proximity sensor," US Patent 0 212 510, 2005.

[19] J. Zoethout, A. Boletis, and H. Bleuler, "High performance capacitive position sensing device for compact active magnetic bearing spindles," *JSME*, vol. 46, pp. 900–907, September 2003.

[20] B. S. Guru and H. R. Hiziroglu, *Electric machinery and transformers*, A. S. Sedra, Ed. Oxfort University Press, 2001.

[21] D. Griffiths, *Introduction to electrodynamics*, 3rd ed. Prentice Hall, 1999.

[22] Y. Bihan, "Study on the transformer equivalent circuit of eddy current nondestructive evaluation," *NDT&E*, vol. 36, pp. 297–302, 2003.

[23] D. Vyroubal, "Impedance of the eddy-current displacement probe: The transformer model," *IEEE Transactions on instrumentation and measurement*, vol. 53, no. 2, pp. 384–391, April 2004.

[24] B. A. Auld and J. C. Moulder, "Review of advances in quantitative eddy current nondestructive evaluation," *Jornal of nondestructive evaluation*, vol. 18, no. 1, pp. 3–36, 1999.

[25] O. C. Zienkiewicz and R. L. Taylor, *The finite element method*, 5th ed. Oxford, UK: Butterworth-Heinemann, 2000.

[26] R. W. Clough, "The finite element method in plane stress analysis," in *Conference on electronic computation*, no. 2. ASCE, 1960.

[27] G. E. Barron, J. R. Brauer, N. J. Lambert, V. D. Overbye, and G. H. Stalker, *What every engineer should known about Finite Element Analysis*, J. R. Brauer, Ed. New York: Marcel Dekker, 1988.

[28] *AC/DC Model User's Guide*, Comsol Multiphysics, Gottengen, Germany, August 2006.

[29] L. Shen and J. Kong, *Applied electromagnetism*, 3rd ed. Boston, USA: PWS Publishing Company, 1995.

[30] R. Kollman, "Constructing your power supply - layout considerations," Texas Instrumants, Dallas, USA, Tech. Rep., 2005.

[31] *Generic Standard on Printed Board Design*, IPC Std. 2221, February 1998.

[32] S. S. Mohan, M. del Mar Hershenson, S. P. Boyd, and T. H. Lee, "Simple accurate expressions for planar spiral inductances," *IEEE Journal of solid-state circuits*, vol. 34, no. 10, pp. 1419–1424, October 1999.

[33] H. A. Wheeler, "Simple inductance formulars for radio coils," vol. 16, no. 10. IRE, Oktober 1928, pp. 1398–1400.

[34] E. B. Rosa, "Calculation of the self-inductances of single-layer coils," *Bull. Bureau Standards*, vol. 2, no. 2, pp. 161–187, 1906.

[35] D. A. Neamen, *Electronic circuit analysis and design*, 2nd ed. Boston, USA: McGraw-Hill, 2001.

[36] F. F. Booyens, "Magnetic bearing micro model," North West University, Potchefstroom, RSA, Tech. Rep., November 2006.

[37] S. B. Vardeman, *Statistics for engineering problem solving*, 1st ed. Boston, USA: PWS Publishing Company, 1993.

Appendix A

Measuring irregularities

Verification of a design can only be done when measured results can be compared to simulated or calculated results. The accuracy of the measured results are also important to ensure correct interpretations and conclusions. It is also true that a level of uncertainty and inconsistency is always present in measured data. In this appendix these irregularities are analysed to better interpret the measured data.

A.1 Boxplots

Displaying large amounts of measured data is challenging as this can easily overwhelm readers. It is sometimes necessary to repeatedly measure a quantity to eradicate unwanted random disturbances such as electronic noise and temperature effects. These large amounts of data can easily be displayed by using boxplots.

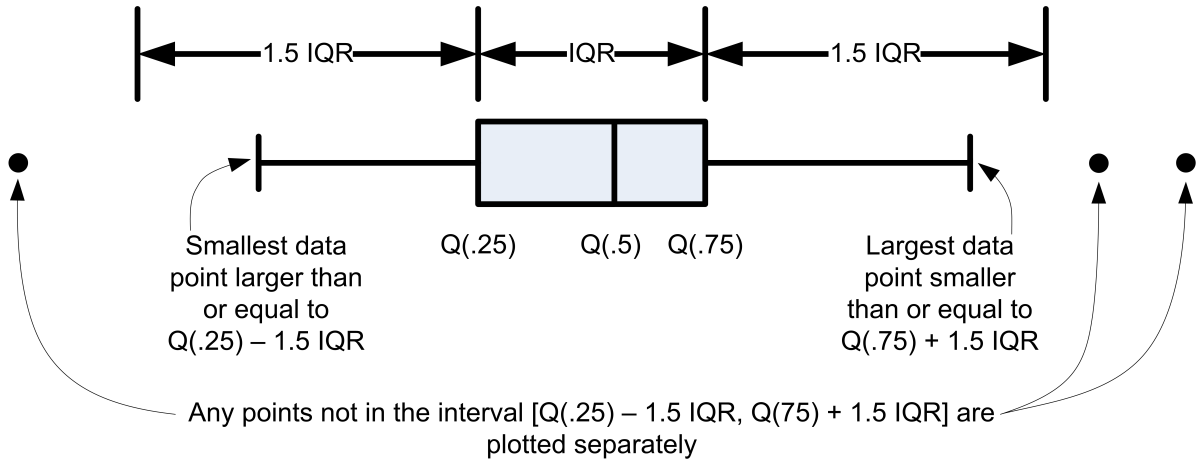

Figure A.1: Generic boxplot [37]

A generic boxplot is shown in Figure A.1. A box is drawn with the first (Q(.25)) and third

(Q(.75)) quartiles as borders. A line is drawn in this box at the median (Q(.5)). The interquartile range (IQR) is the difference between first and third quartile. Lines or "whiskers" are drawn at the data points up to 1.5 IQR smaller than Q(.25) and up to 1.5 IQR larger than Q(.75). Any points outside of this range are plotted individually . A boxplot can give an indication of the distribution shape as well as the variance in the data. Comparing the range of different data sets is easily done and irregular measurements are highlighted visually [37].

A.2 Current probe phase shift

The excitation coil characteristics (resistance and impedance) of the manufactured PCB sensor must be compared to the characteristics predicted in the design. This is done by using (4.2) to calculate the characteristics from the measured data. A fast fourier transform (FFT) is used to find the amplitude and phase of the phasors measured with a LeCroy® WaveRunner® 6030A digital oscilloscope. In (4.2) the voltage is chosen as reference and thus has a 0° phase angle. The phase between voltage and current is the phase angle θ. In a mainly inductive circuit the current is lagging the voltage and the phase angle is negative. A phase angle can only vary between -90° and 90° [20].

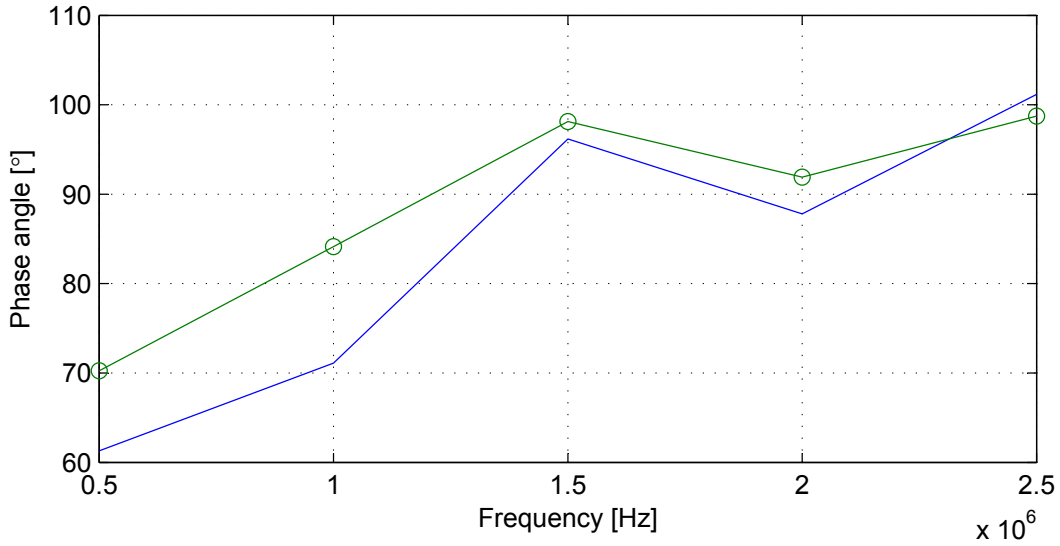

Figure A.2: Excitation coil impedance phase angle vs. frequency

The excitation coil impedance is determined from the excitation coil voltage and current. Figure A.2 shows the phase angle of this impedance at frequencies between 0.5 and 2.5 MHz. A phase angle θ larger than 90° is obtained, which is impossible. This phenomenon must be understood before the measured impedance can be compared to the predicted impedance.

A purely resistive load is connected to the drive circuit to try and pinpoint the source of the phase shift. An ac current, roughly equal to the amplitude of the sensor operating current, is applied to the resistive load. Voltage and current signals are captured with the oscilloscope and

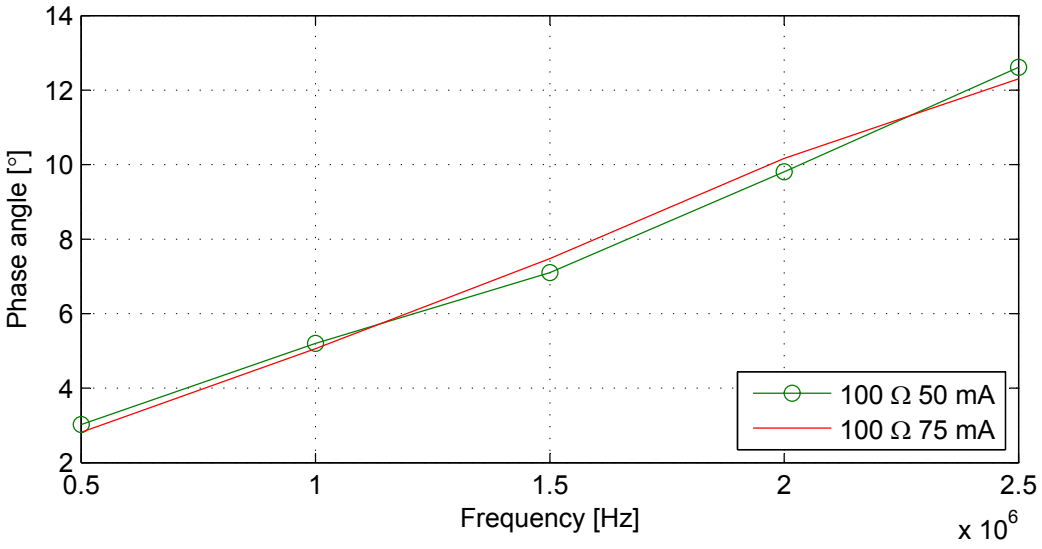

Figure A.3: Resistive load impedance phase angle vs. frequency

the impedance is determined using (4.2). The phase angle vs frequency for a 100 Ω resistive load, with 50 and 75 mA flowing through it, is shown in Figure A.3. Surface mount carbon resistors are used since these components have a very small internal inductance when compared to wire wound resistors. A large, almost linear phase shift can be seen in the figure. This proves that the phase shift is not only caused by the load but also by the oscilloscope and probes used. The effect can be eliminated by subtracting the expected phase shift from the measured results.

A.3 Difference in probe readings

Measuring the same voltage with different oscilloscope probes should give the same reading. This statement is tested by connecting all 4 probes to the same sensing coil and capturing the data with the oscilloscope. Rated current flows through the excitation coil and the waveforms are saved in 15 second intervals. The target is not moved and 90 measurements are taken. The rms voltage for each measurement is calculated using FFTs as discussed earlier and the results are summarized in Figure A.4. Another 70 measurements is taken at a different position and these results are summarized in Figure A.5.

The difference between the largest median (Probe 1) and smallest median (Probe 4) is 3.3 mV and 3.4 mV for the two target positions respectively. The IQR for the two target positions is 2.1 mV and 1.9 mV, respectively. All the boxplots are quite symmetrical thus the distribution is bell-shaped. The variance of all the measurements is relatively equal and thus reacts the same on change in input. The variance can be attributed to oscillator drift and is discussed in the following section. The difference in probe output can be ignored by using only 1 probe for all the measurements. The problem can also be minimised by normalising the probes, i.e. making the medians equal by subtracting a specific constant value form each of the sensing coil voltages.

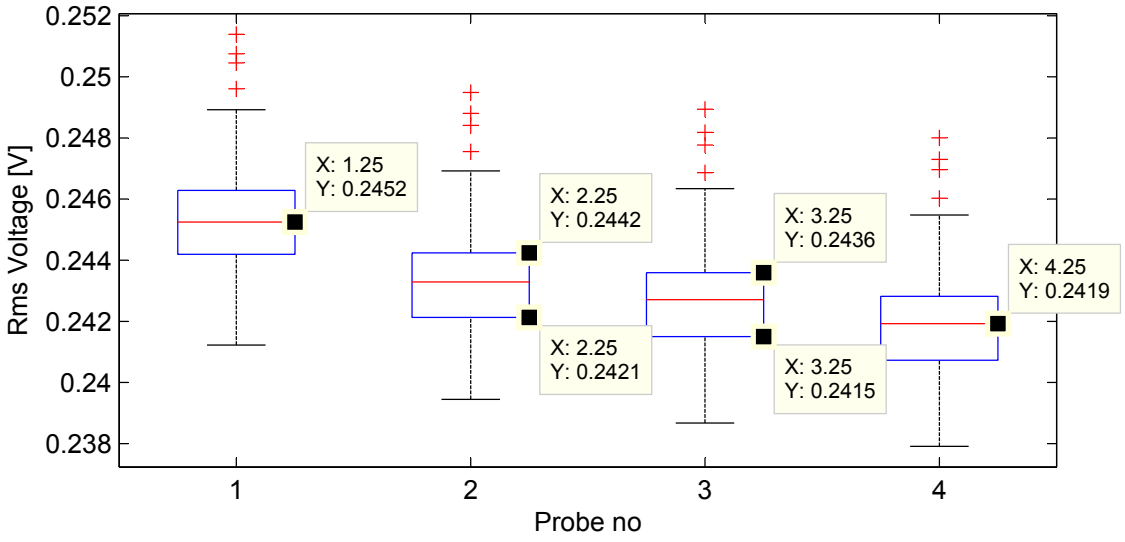

Figure A.4: Rms sensing coil voltages vs probe numbers [1 - 90]

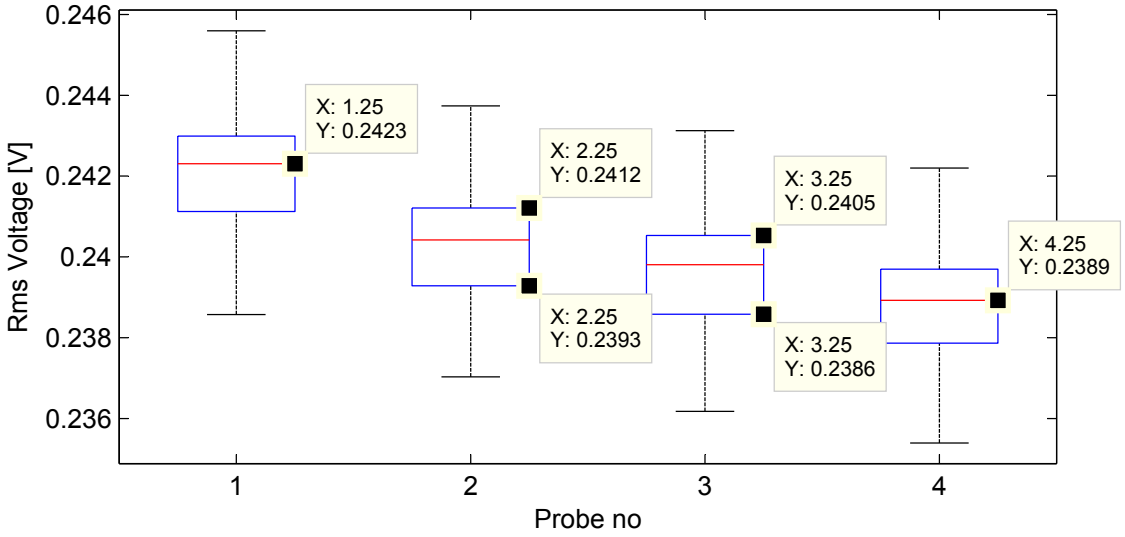

Figure A.5: Rms sensing coil voltages vs probe numbers [91 - 160]

A.4 Oscillator drift

The driver circuit is a voltage-to-current converter that controls the excitation coil current according to a voltage reference. In the evaluation platform the reference is generated using an EZ® Digital FG7020A signal generator. A change in reference voltage directly influences the excitation coil current. This in turn changes the magnetic flux levels in the sensing coils and thus also the voltages induced in the sensing coils. Signal generator frequency and amplitude drift thus directly influences sensor operation.

Oscillator drift effects on a sensing coil voltage is shown in Figure A.6. The target position is not changed and one probe is used for all the measurements. Measurements 1 - 24 are taken after the oscillator was on for a long time ($>$ 7 hours), measurements 25 - 53 are taken 10 minutes after switching on the oscillator and measurements 54 - 78 are taken 1 hour after switching on the oscillator. At the start of each measuring series the oscillator voltage is adjusted to ensure a 100 mA current is flowing in the excitation coil. Each of the measurement series is taken over a 6 minute time frame in 15 second intervals.

When the oscillator is on for longer than an hour, the change in sensor voltage is 1.4 mV and 2.6 mV for the two measurement series respectively. A much larger change in sensing coil voltage (3.9 mV), shortly after switching on the oscillator, can be attributed to temperature effects of the oscillator internal components. These effects might seem negligible as it causes a smaller than 2 % change in rms amplitude. However, when only a 10 mV change in sensing coil voltage over the whole measuring range is detected, this drift could cause a 20 % error in position output. In the next section the differences in the sensing coils are explored.

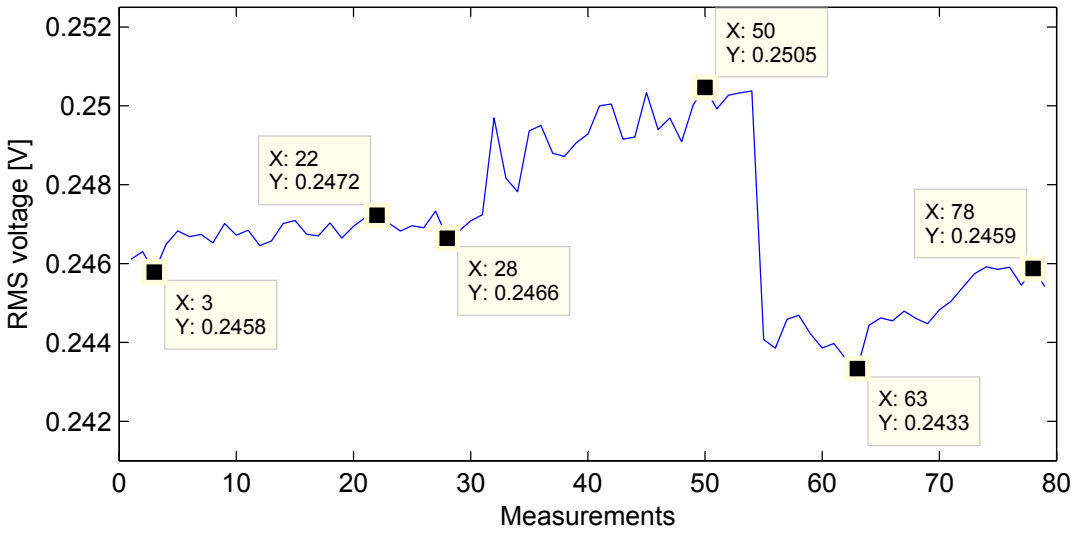

Figure A.6: Sensing coil 2 voltage for a constant target position, showing oscillator drift

A.5 Sensing coil differences

All the sensing coils are identical as shown in Figure 2.13. The connection between the sensing coils and connector are however not the same for all four sensing coils. Two sensing coils are situated close to the connector and have identical connecting tracks. This differs from the connecting tracks of the other two sensing coils which are longer. The difference in sensing coil rms voltage caused by this irregularity is investigated in this section.

To compensate for the difference in voltage measured with different probes, one probe is used for all the measurements in this section. The probe is moved to the coil that must be measured

and thus moved after each measurement. Drift effects are counteracted by constantly adjusting the oscillator voltage to ensure the correct excitation coil current flows. The sensing coil voltages are measured at the two extreme positions for each of the four coils, i.e. the furthest and nearest the target can be from a specific coil. Eleven measurements are captured at each of the positions for all four sensing coils. Figure A.7 shows the measurement results in boxplot format.

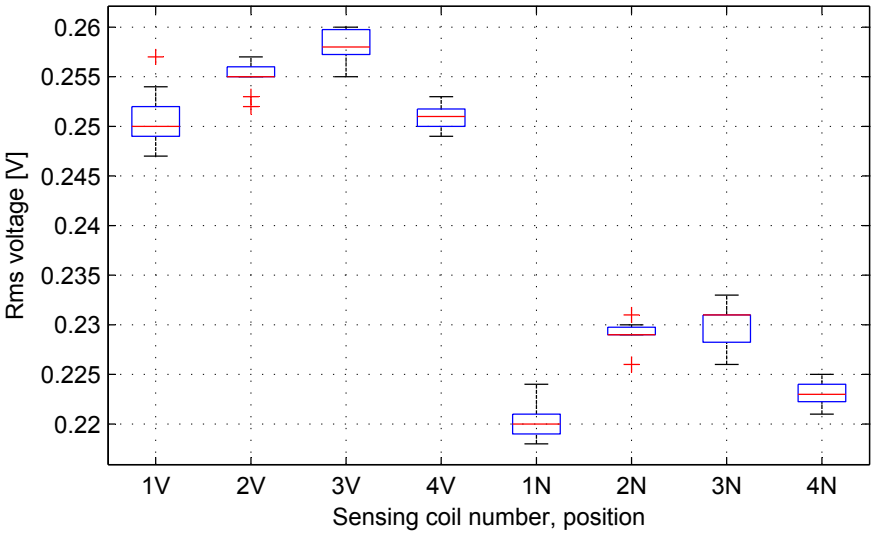

Figure A.7: Sensing coil rms voltage with target near and far from the coils

The sensing coil number used in Figure A.7 refers to Figure 4.11. The furthest position results are shown above the Fs and nearest above the Ns. It is clear that the sensing coils with short connecting tracks (1 and 4) have a smaller rms voltages than those with long connecting tracks (2 and 3). This is true for target positions near and far from the sensing coils. Variance of the results also differs; sensing coil 2 has the smallest variance and sensing coil 3 the largest. This could be attributed to a small set of data; only 11 measurements per boxplot.

Appendix B

Manufacturing drawings

B.1 Drawing numbering conventions

The drawings are all numbered according to the numbering convention shown in Figure B.1.

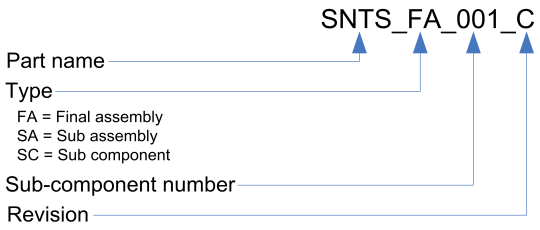

Figure B.1: Manufacturing drawings' numbering convention

Table B.1 gives the part names and a short description of each of the parts.

Table B.1: Part number and description.

Part name	Description
SNTS	Sensor test setup overview
BASE	Base plate
SEHO	$\mu\epsilon$ Sensor holder
CNAX	Sensing axis
PCBP	PCB Pillar type 1
PCBP	PCB Pillar type 2
LEGG	Leg
WSHR	Washer
SNTS	Sensing axis sub assembly
AXCX	Threaded rod
ACAX	Sensing axis

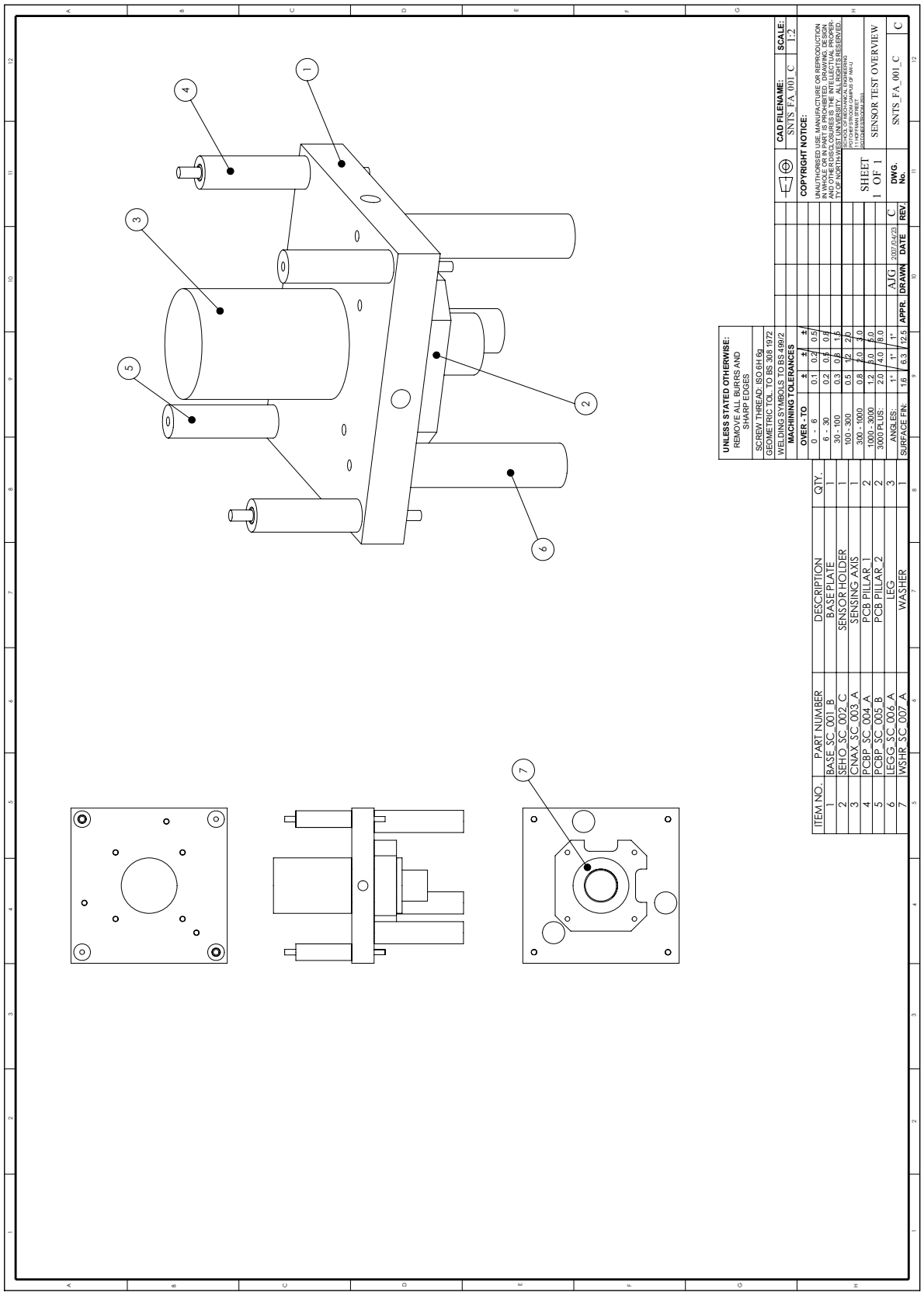

Figure B.2: Sensor test setup overview

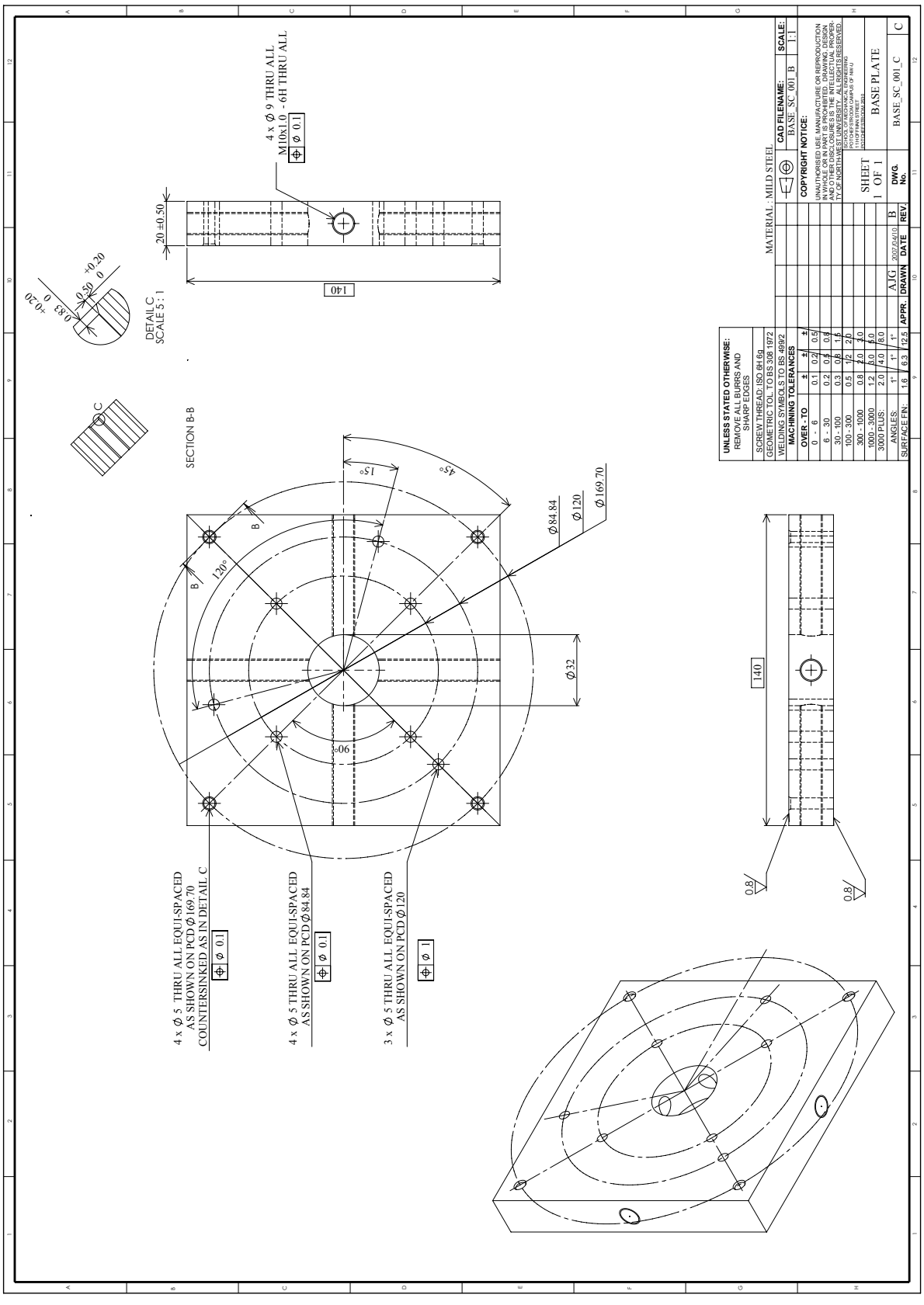

Figure B.3: Base plate

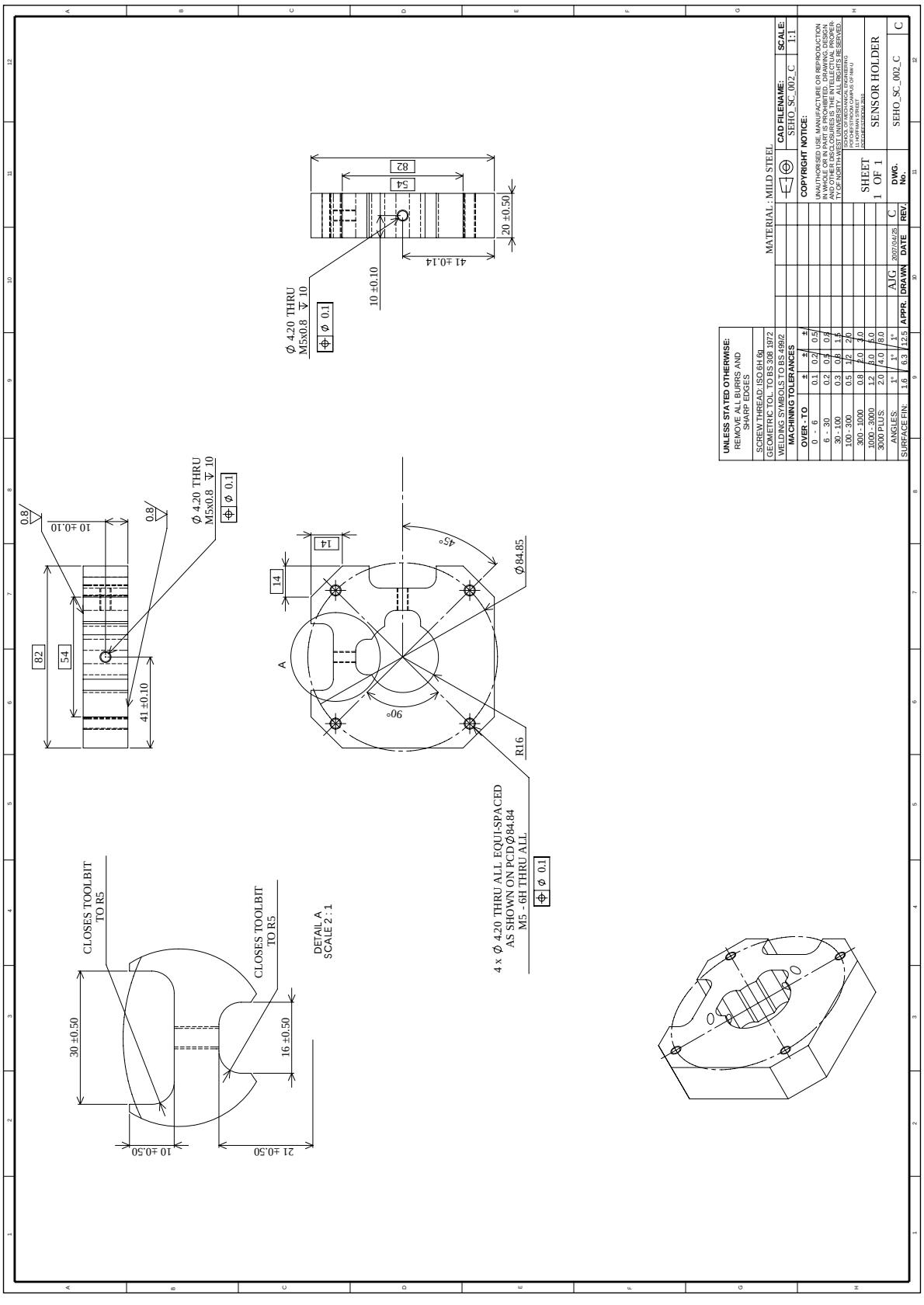

Figure B.4: $\mu\epsilon$ Sensor holder

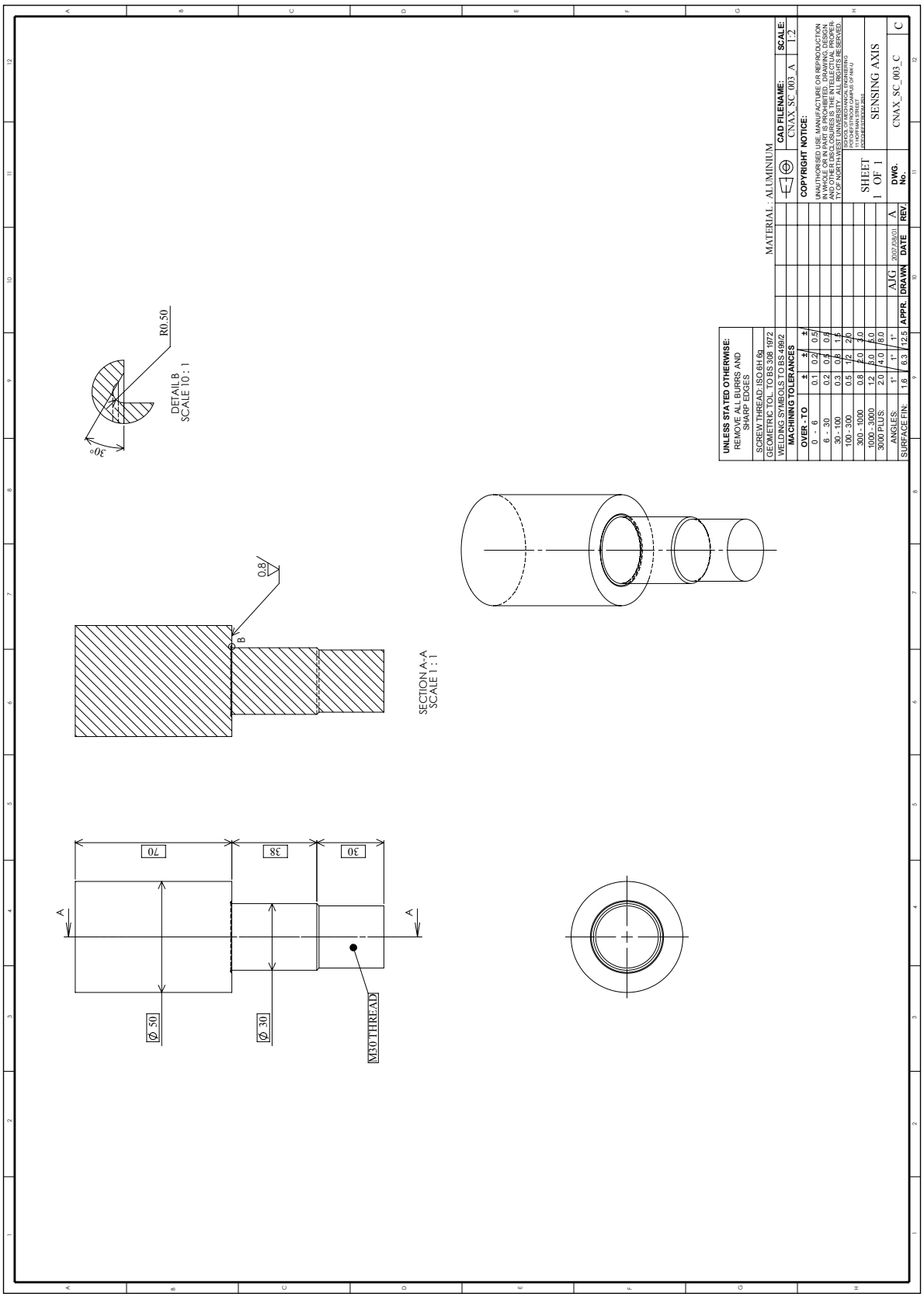

Figure B.5: Sensing axis

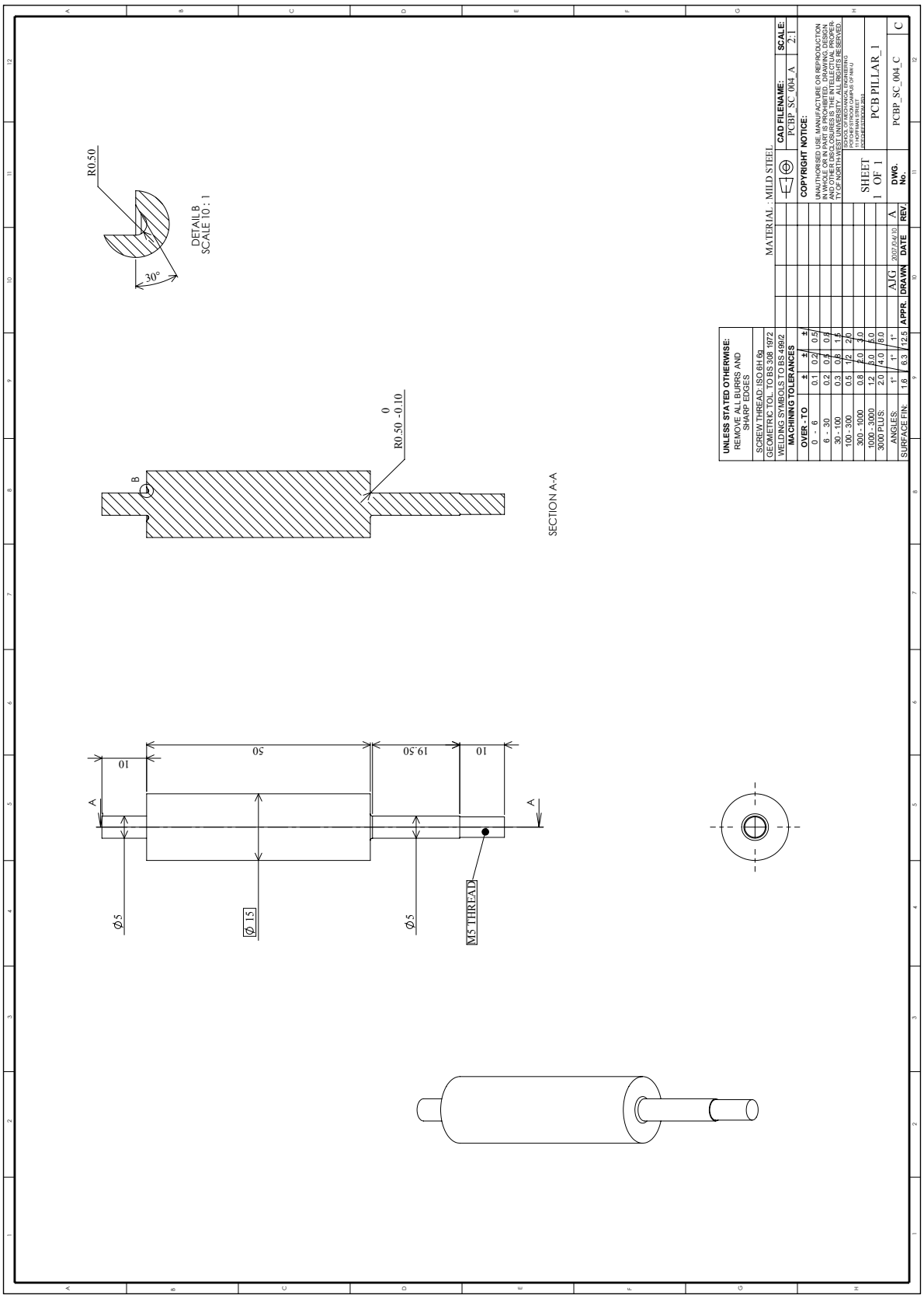

Figure B.6: PCB Pillar type 1

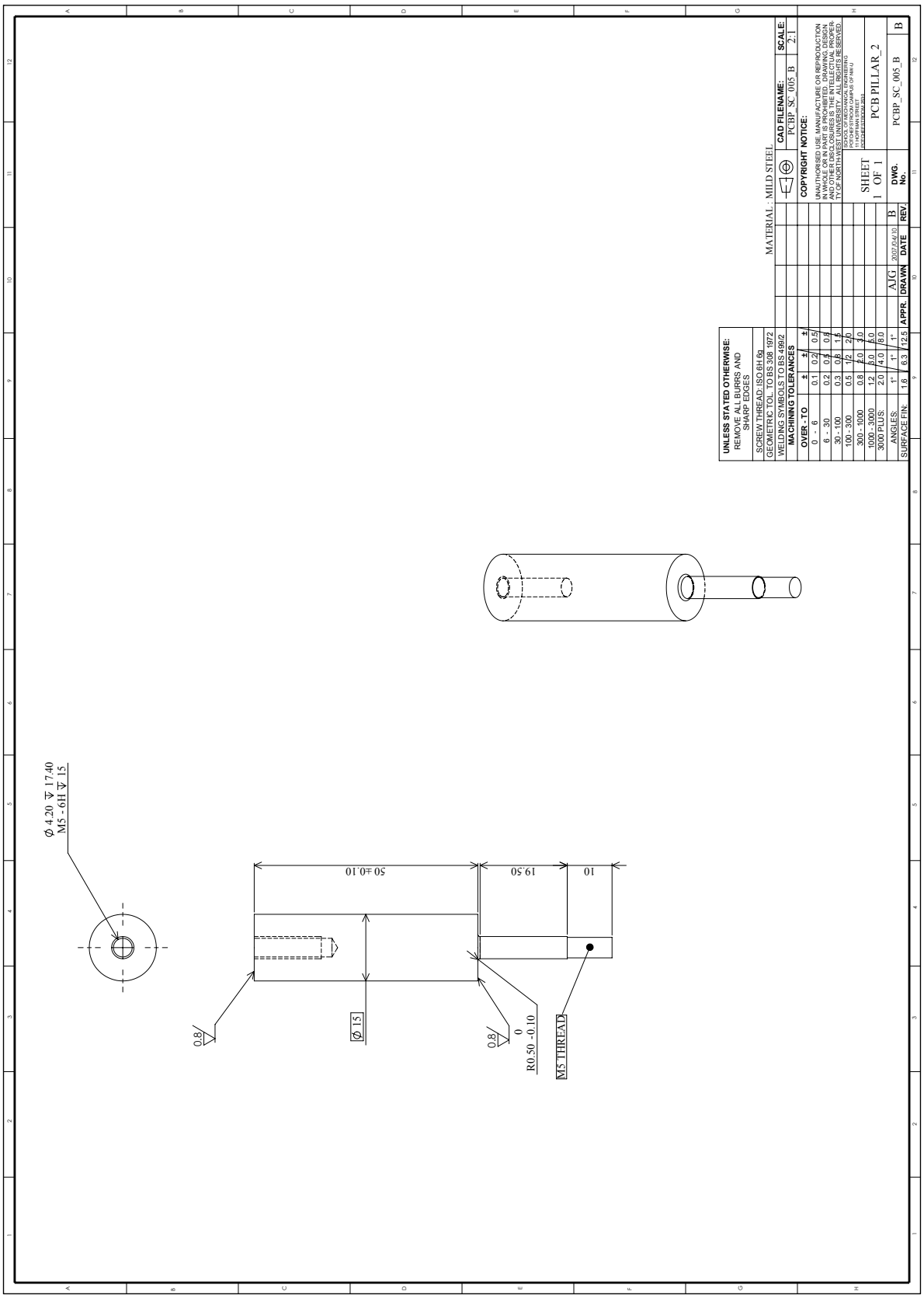

Figure B.7: PCB Pillar type 2

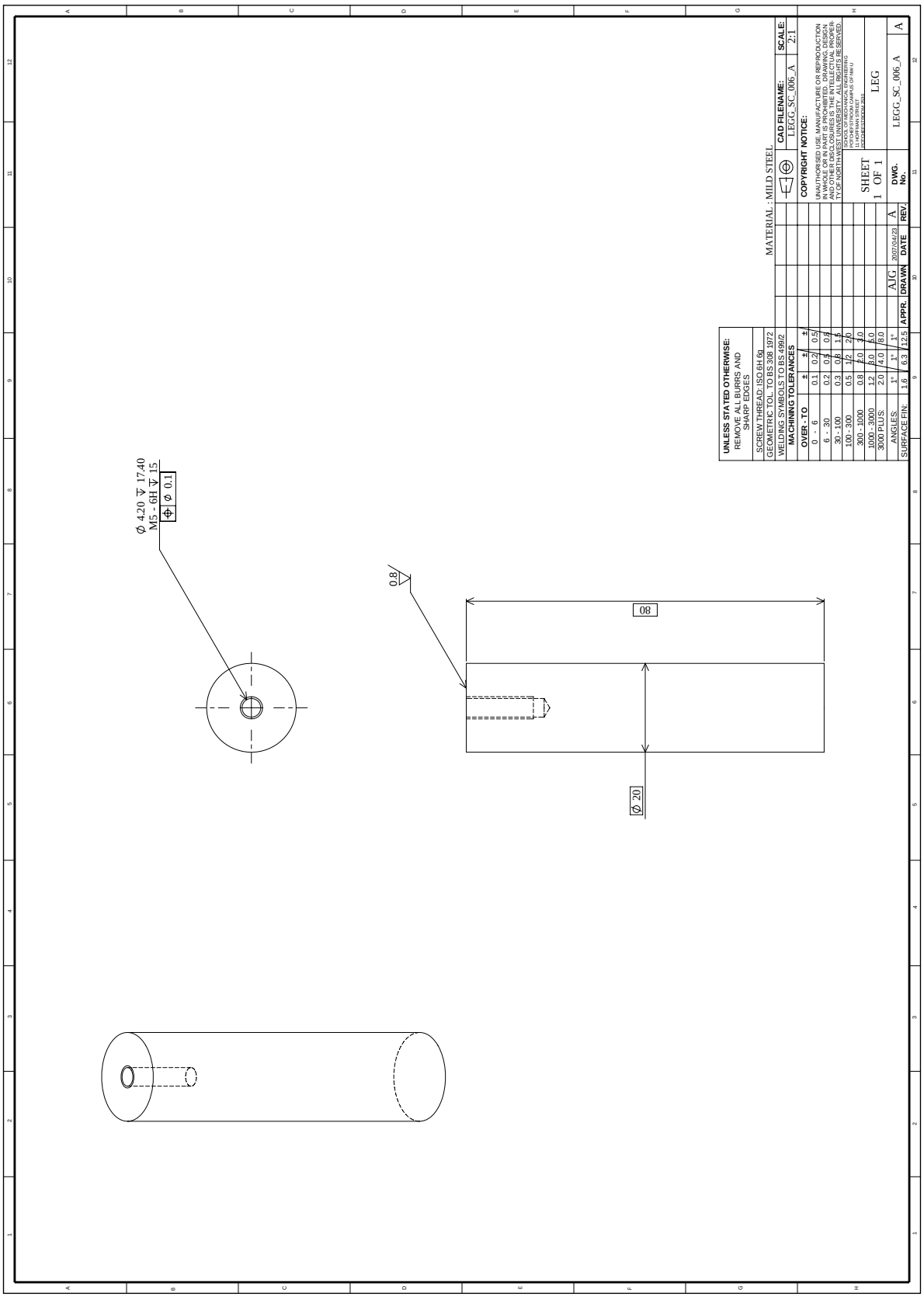

Figure B.8: Leg

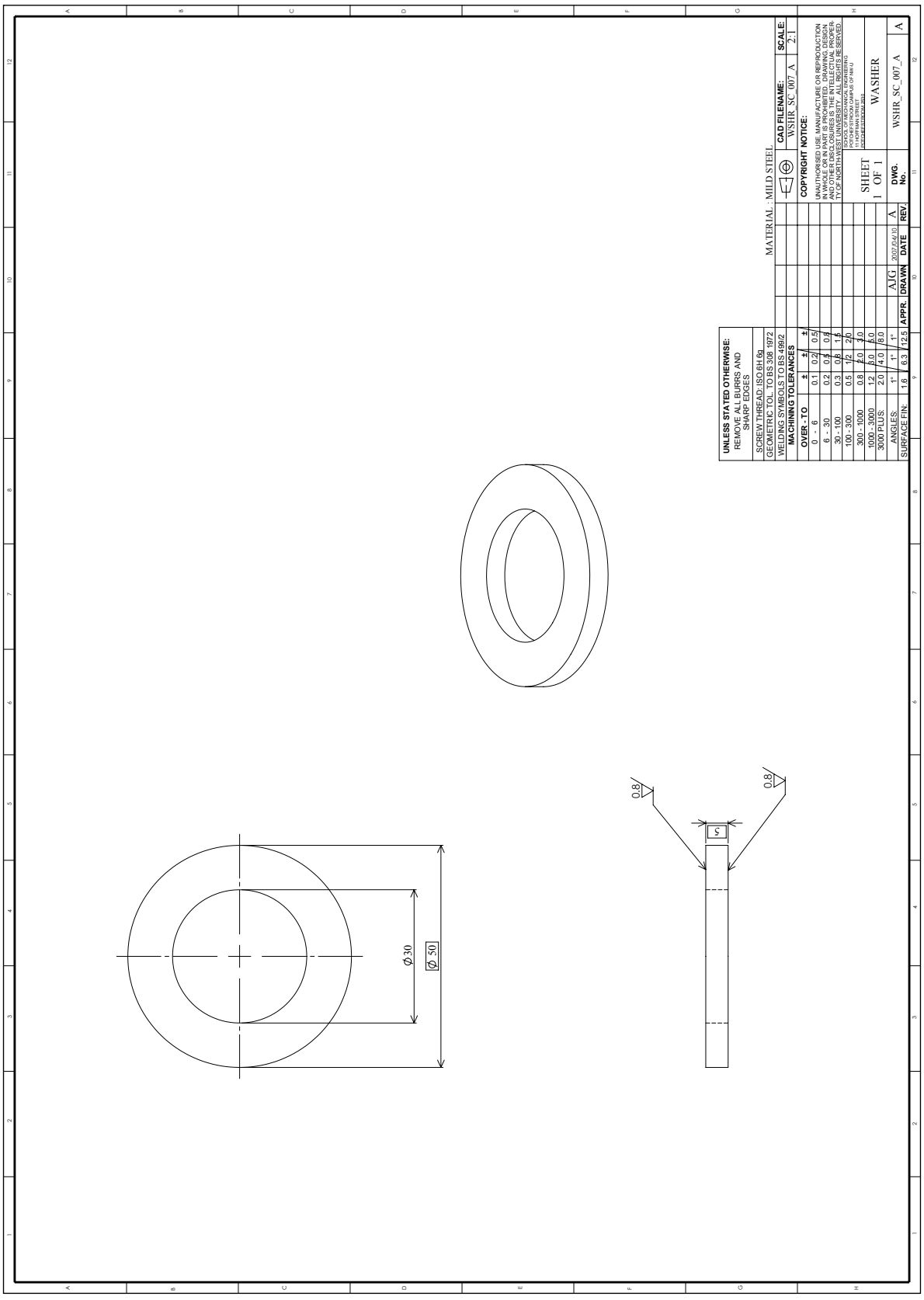

Figure B.9: Washer

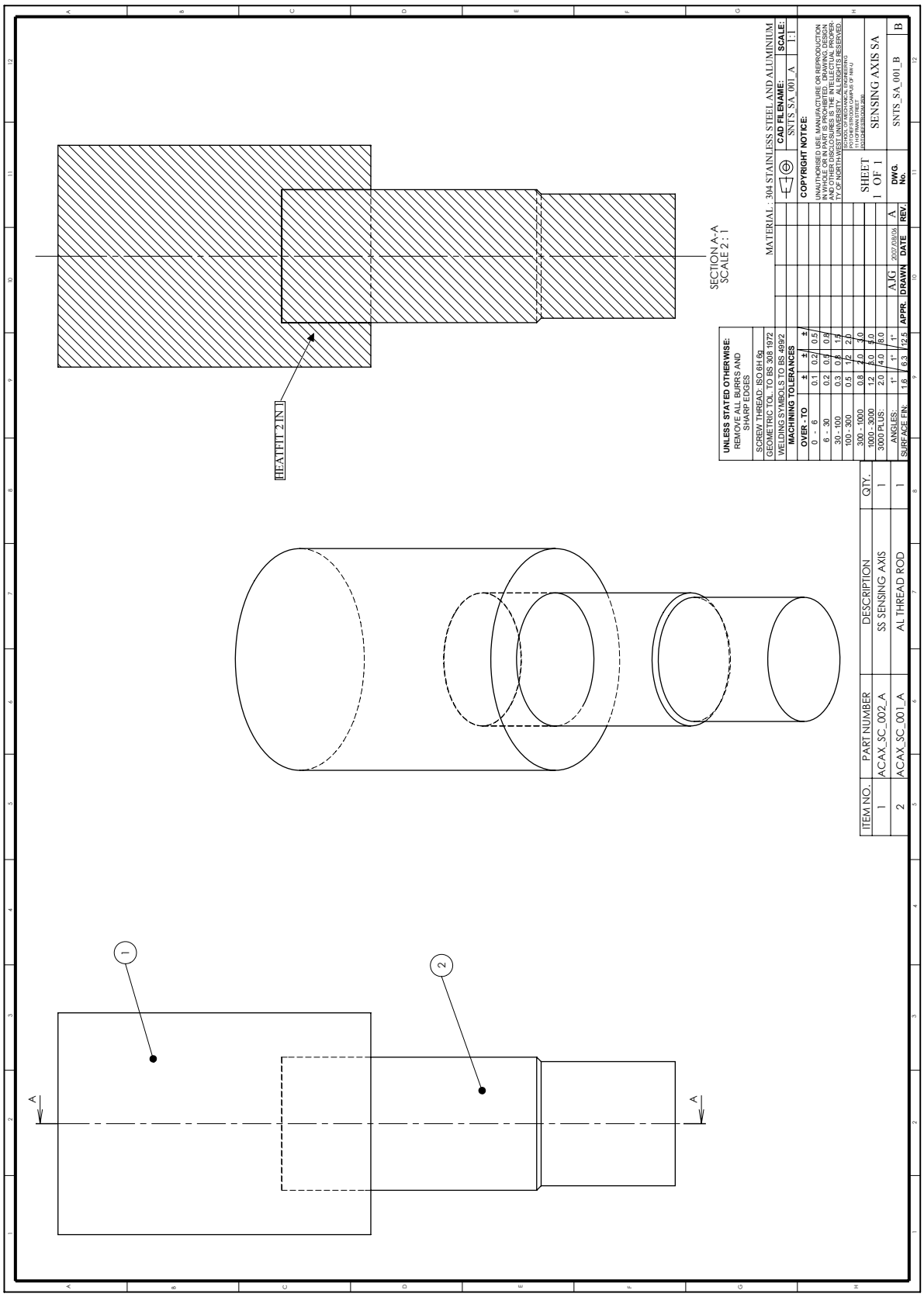

Figure B.10: Sensing axis sub assembly

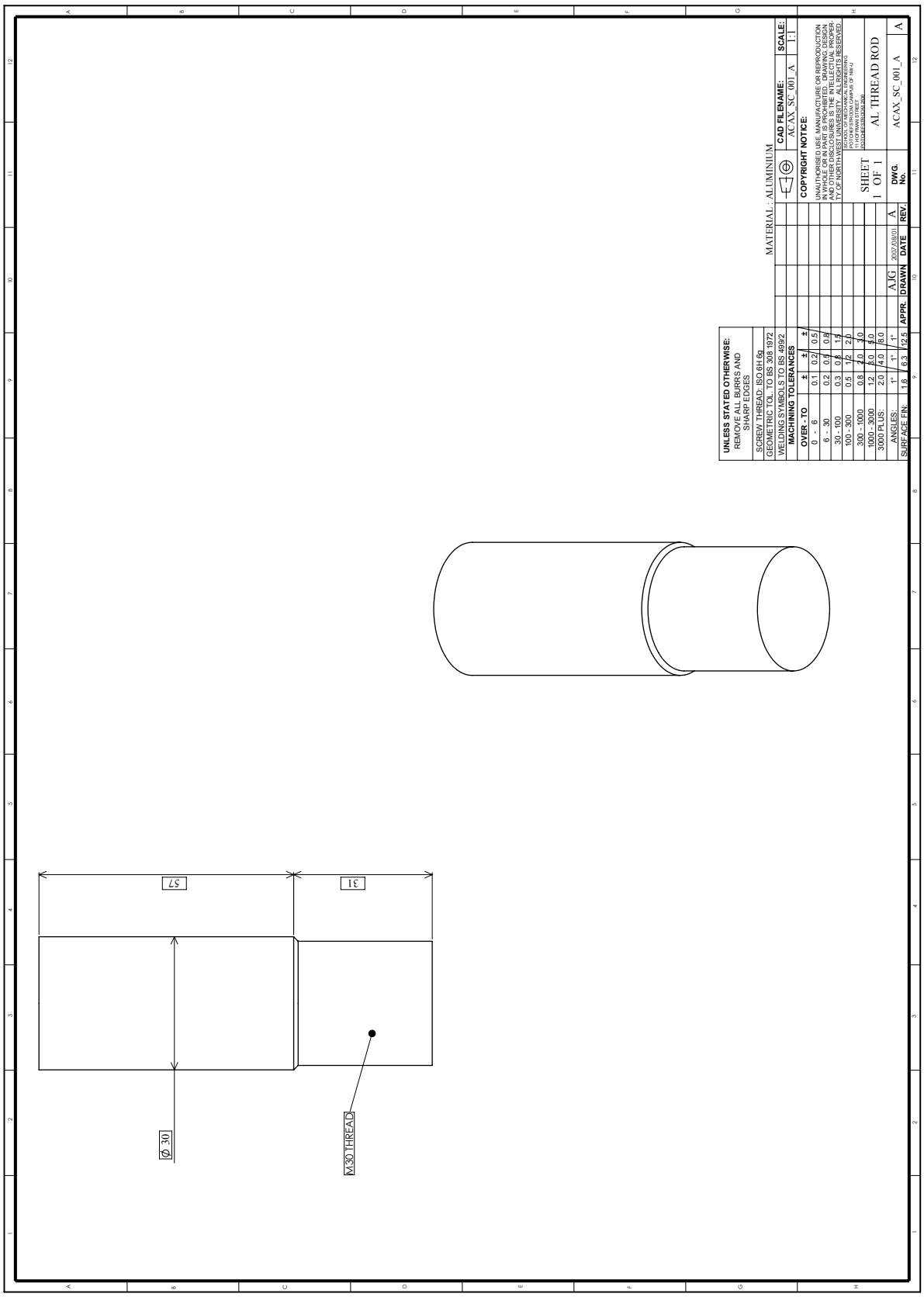

Figure B.11: Threaded rod

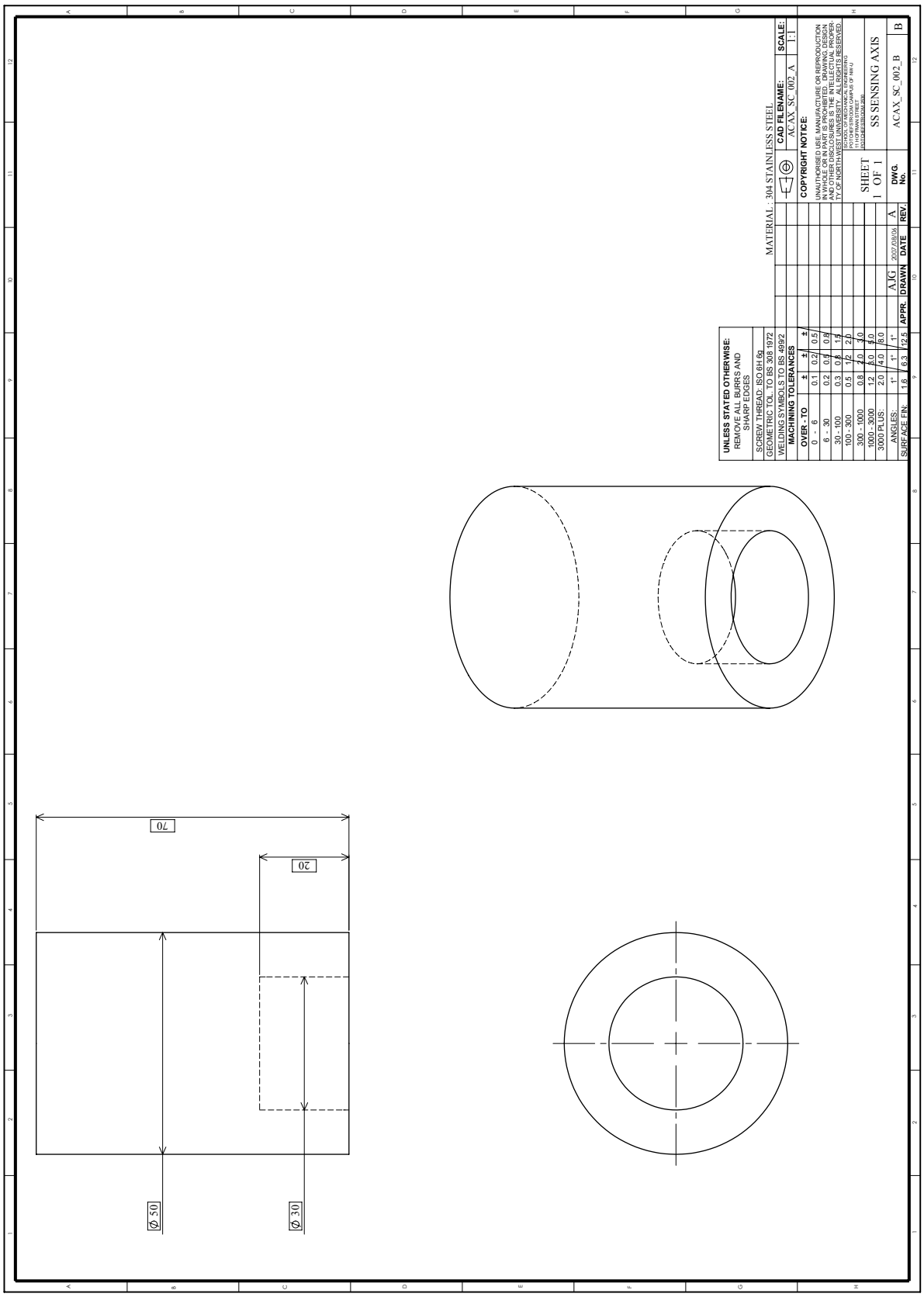
70
20
Ø 50
Ø 30
UNLESS STATED OTHERWISE:
REMOVE ALL BURRS AND SHARP EDGES
SCREW THREAD: ISO 61 6g
GEOMETRIC TOL. TO BS 308:1972
WELDING SYMBOLS TO BS 499/2
MACHINING TOLERANCES
OVER - TO ± ± ±

Appendix C

Sensor system layout

C.1 Single-layer sensor

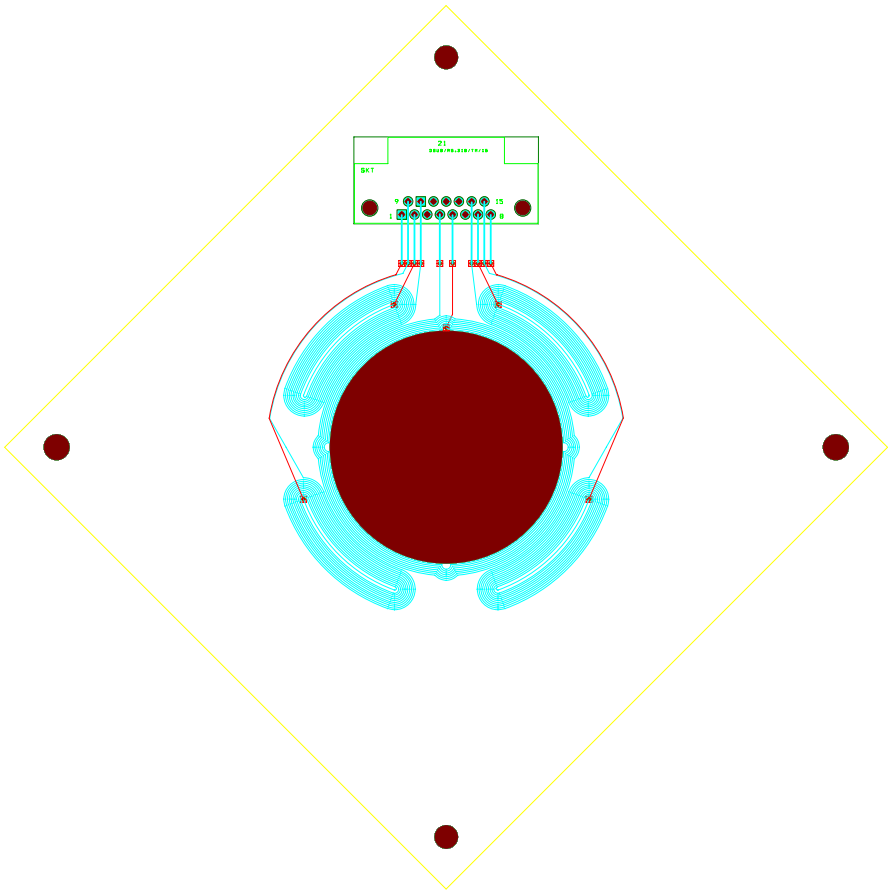

Figure C.1: Single-layer sensor ($n_{exc} = 7$, $n_{sens} = 11$)

C.2 Double-layer sensor

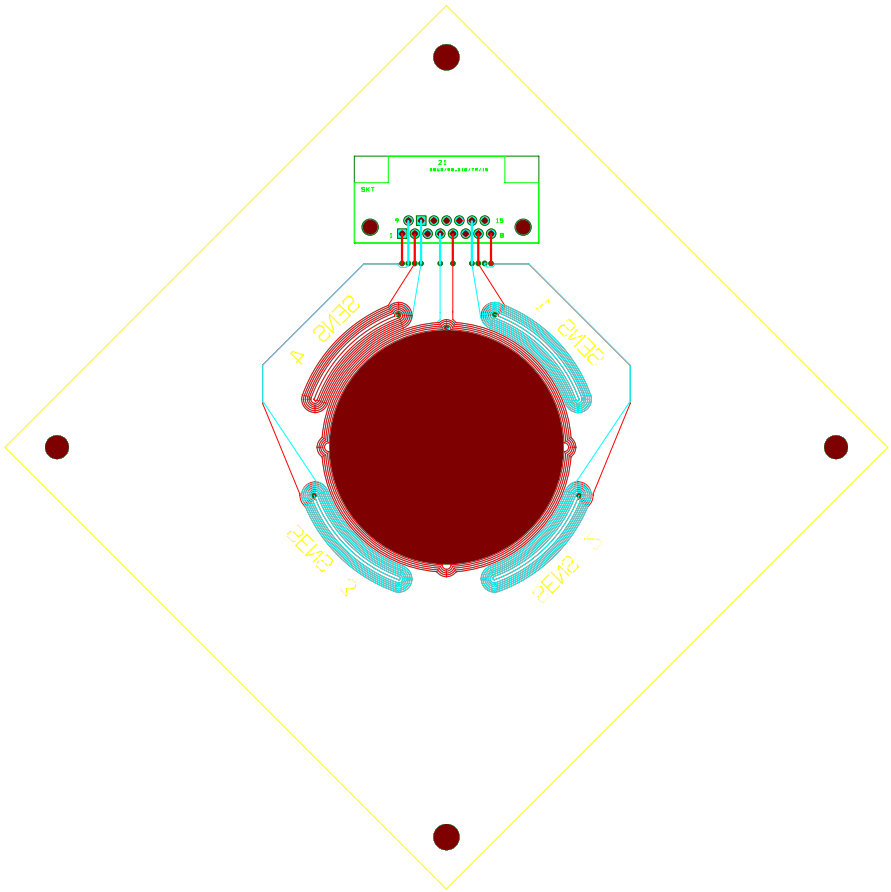

Figure C.2: Double-layer sensor top layer ($n_{exc} = 5$, $n_{sens} = 7$)

C.3 Drive circuit

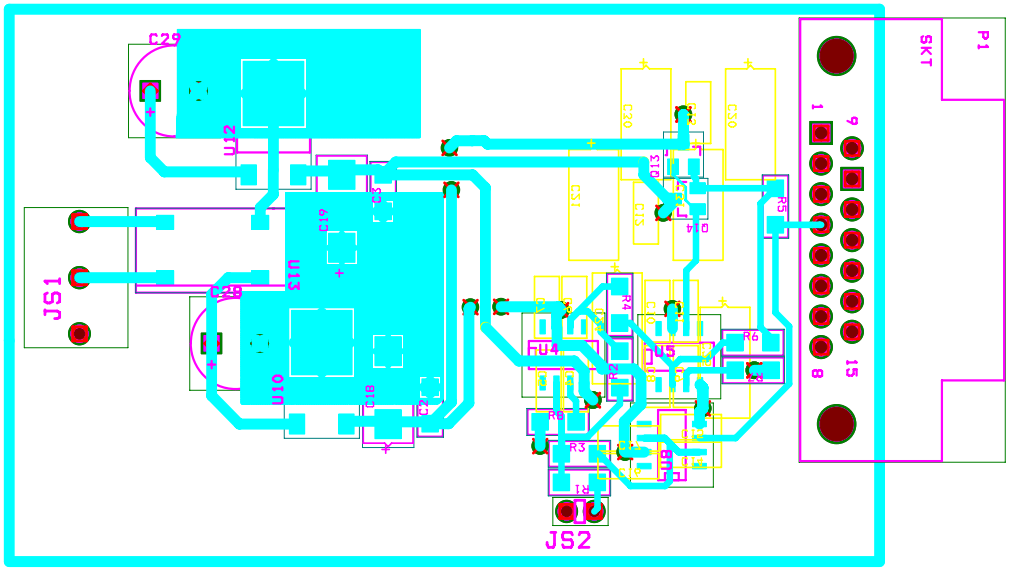

Figure C.3: Drive circuit top view

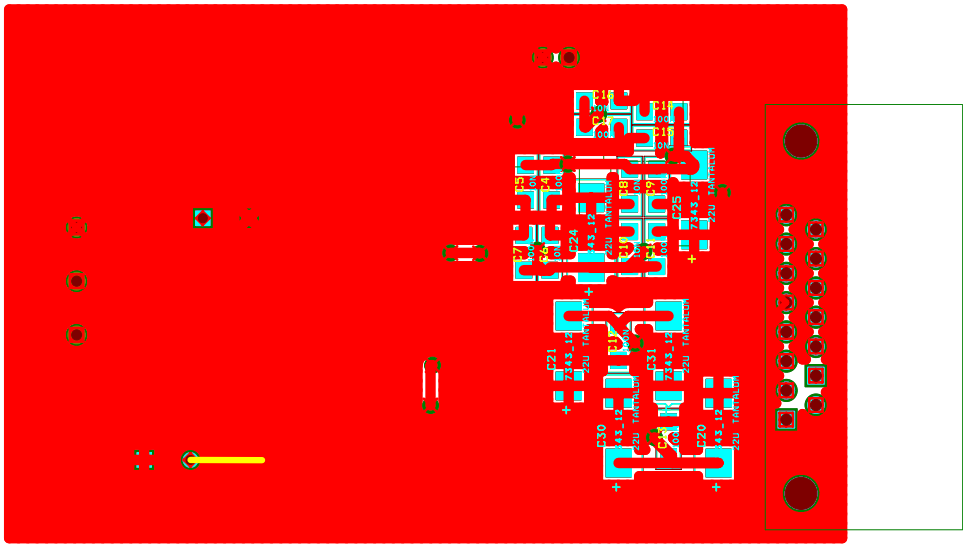

Figure C.4: Drive circuit bottom view

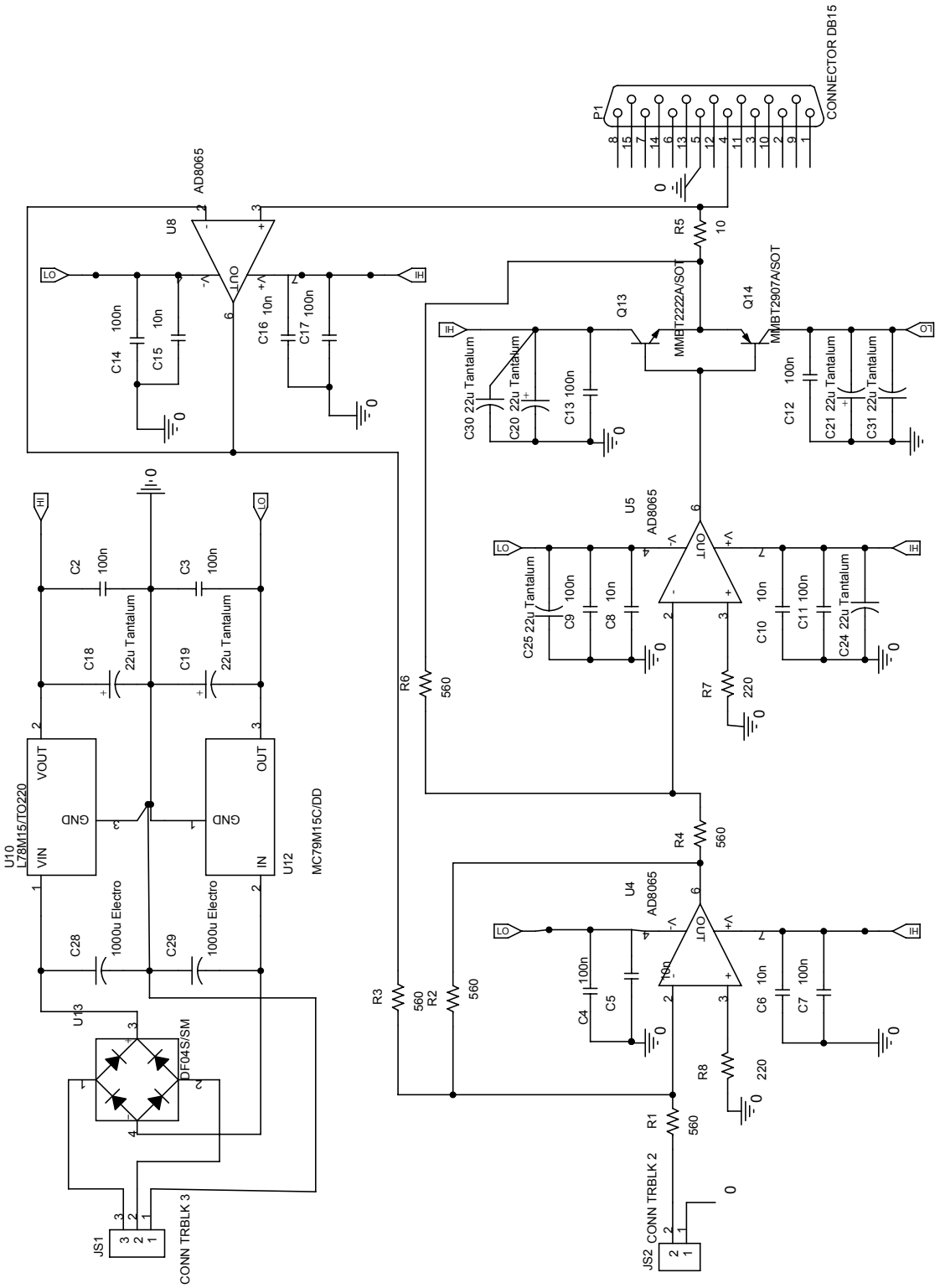

Figure C.5: Drive circuit diagram

Appendix D

Data DVD

This appendix lists all the data included on the data DVD.

D.1 Comsol Script® code and data

In this folder the m-files used in the simulation as well as the mat-files containing the results are included for the single-, double- and five-layer sensors.

D.2 Solidworks® sketches

The mechanical sketches of the evaluation platform are all included in this location. The sketches used to generate the PCB tracks are also included.

D.3 Orcad® files

The sensor drive circuit's simulation and layout files as well as the sensor probe's layout files are included in this section.

D.4 Measured data

In this folder, the data captured with the oscilloscope can be found.

D.5 MATLAB® code

The m-files used to demodulate the measured data can be found in this folder.

D.6 Photos

Photos of the PCB sensors, evaluation platform and drive circuit are included in this folder.

D.7 Documentation

The project proposal and dissertation can be found in this folder.

D.8 References

Some of the references, in pdf format, can be found in this folder.